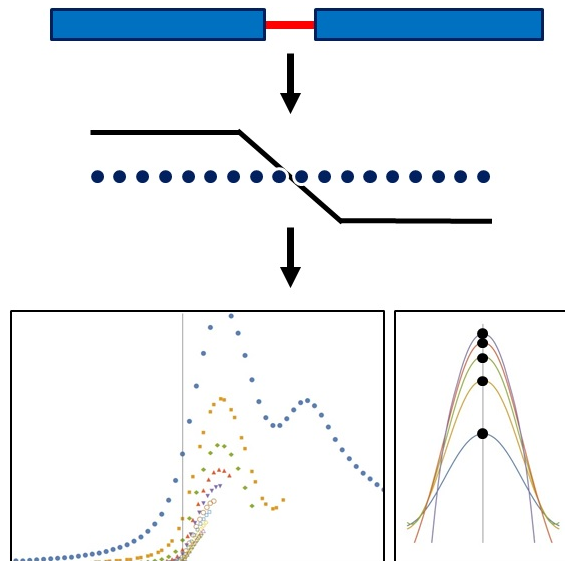


DMRG method for the linear DC-conductance of one-dimensional correlated systems



Von der Fakultät für Mathematik und Physik
der Gottfried Wilhelm Leibniz Universität Hannover

zur Erlangung des akademischen Grades
Doktor der Naturwissenschaften
Dr. rer. nat.

genehmigte Dissertation von

Msc. Jan-Moritz Bischoff

2019

Referent:

Prof. Dr. Eric Jeckelmann, Leibniz Universität Hannover

Korreferenten:

Prof. Dr. Wolfram Brenig, Technische Universität Braunschweig

Prof. Dr. Holger Frahm, Leibniz Universität Hannover

Tag der Promotion: 16.12.2019

Abstract

Interesting discoveries have recently been made in the area of solid state physics and nano technology regarding electronic systems that are confined to reduced spatial dimensions. Under these circumstances the quantum nature of the electrons begins to surface. In the one-dimensional case this class of systems is therefore called quantum- or nano wires. The conductance in such quantum wires becomes quantized and is dominated by electronic correlations.

The goal of this thesis was to develop a fast and efficient procedure to describe a realistic transport measurement for such systems. The method presented here is inspired by the work of Dan Bohr et al. who used the Density Matrix Renormalization Group algorithm(DMRG) to evaluate the Kubo formula for the linear response to an applied potential. In a similar way the procedure of this thesis also computes the Kubo formula using the dynamical DMRG in order to calculate the low frequency response to an AC source-drain voltage of finite systems. Making use of a special finite size scaling allows to extrapolate the results into the thermodynamic limit and to finally obtain the linear DC-conductance.

First, the theoretical framework for the new method was developed. This was followed by testing the new approach in different model systems. The first model comprised of a tight-binding chain that was filled with spinless, noninteracting fermions. In subsequent steps the model was expanded by introducing a homogeneous interaction in the Luttinger liquid regime followed by inhomogeneous interaction for different chain sections. The potential impact of impurities was assessed in the above models.

Lastly, the two cases of the Hubbard chain of spin- $\frac{1}{2}$ electrons and of the Holstein model in one dimension, where Einstein phonons interact with spinless fermions, were studied.

The results of the proposed method are consistent with Luttinger liquid and Landauer scattering theory. In the Luttinger liquid regime the influence of phonons to the charge structure factor was confirmed. A dependency on the length of the quantum wire in the form of dissipation effects for the conductance was not observed.

Keywords:

conductance of nanowires, Density Matrix Renormalization Group, Luttinger-liquid

Zusammenfassung

Im Bereich der Festkörperphysik und Nanotechnologie haben sich in jüngster Zeit interessante Beobachtungen in elektronischen Systemen machen lassen, die räumlich auf wenige Dimensionen eingeschränkt sind. Entgegen der klassischen Erwartung kommen hier Quantenphänomene der betrachteten Fermionen zum Vorschein. Im eindimensionalen Fall werden diese Systeme daher auch Quanten- oder Nanodrähte genannt. Die Leitfähigkeit in solchen Quantendrähten wird durch quantenmechanische Elektronenkorrelationen dominiert und ist quantisiert.

In dieser Arbeit wird eine schnelle und effiziente numerische Methode entwickelt, die den Anspruch hat eine Transportmessung an einem Quantendraht möglichst realitätsnah zu beschreiben. Diese Methode ist inspiriert von der Arbeit Dan Bohrs et al., der bereits gezeigt hat, dass mithilfe der Dichte-Matrix Renormierungsgruppenalgorithmus(DMRG) die Kuboformel für die lineare Antwort auf ein Potential berechnet werden kann. Ähnlich dazu wird auch hier die Kuboformel mithilfe der dynamischen DMRG für eine AC Source-Drain Spannung für endliche Systeme berechnet. Ein spezielles Finite Size Scaling erlaubt es, die Ergebnisse für diese endlichen Systeme in den thermodynamischen Grenzfall zu extrapolieren und schließlich die lineare DC-Leitfähigkeit zu erhalten.

Zunächst wird das theoretische Grundgerüst für die Methode erläutert. Im darauf folgenden Teil wird die Methode an verschiedensten Modellsystemen getestet. Als erstes Modell wird eine Tight-Binding Kette untersucht, in der die Fermionen weder Spin besitzen, noch in irgendeiner Form wechselwirken. Das Modell wird dann langsam erweitert, indem erst homogene Wechselwirkung im Luttinger Flüssigkeitsbereich und dann inhomogene Wechselwirkung in unterschiedlichen Teilabschnitten der Kette untersucht werden. Des Weiteren wird der Einfluss von Störstellen in diesen Systemen untersucht. Zuletzt werden schließlich die beiden Fälle einer Hubbard Kette mit Spin- $\frac{1}{2}$ Elektronen und des Holstein Modells in einer Dimension mit Einsteinphononen, die mit spinlosen Fermionen wechselwirken, betrachtet.

Die Ergebnisse der Methode sind konsistent mit der Luttinger Flüssigkeits- und mit der Landauer Streutheorie. Außerdem lässt sich ein Einfluss von Phononen auf den Ladungsstrukturfaktor im Luttinger Regime beobachten. Eine Abhängigkeit der Leitfähigkeit durch eine Änderung der Länge des Quantendrahtes und etwaigen Dissipationseffekten ließ sich in allen Fällen nicht beobachten.

Schlagwörter:

Leitfähigkeit von Nanodrähten, Dichte-Matrix Renormierungsgruppe, Tomonaga-Luttinger-Flüssigkeit

Contents

1. Introduction	1
1.1. Conductivity and Conductance	1
1.2. Setup	4
1.3. Model and Outline	5
2. Shape of the Perturbation	11
3. Density Matrix Renormalization Group	16
3.1. Infinite-system DMRG	17
3.2. Finite-system DMRG	20
4. Finite Size Scaling DDMRG	22
4.1. Dynamical Density Matrix Renormalization Group	22
4.2. Converting DDMRG Output into broadened Conductance	25
5. Verifying the Method	30
5.1. Tight-Binding Chain - Correlator Calculation	30
5.2. Tight-Binding Chain - Numerical Results vs. Analytical Expectation	35
6. Luttinger Liquids and Fermionic Interaction	39
6.1. Homogeneous Interaction	39
6.2. Homogeneous Interaction - Single Barrier	41
6.3. Homogeneous Interaction - Double barrier	44
7. Inhomogeneous Interaction	50
8. Boson Interaction - Holstein Chain	56
9. Spinfull Fermions - Hubbard Chain	61
10. Conclusion	66
A. Appendix	69
A.1. Current Operator as Linear Response to an External Field	69
A.2. Kubo Formulation of the Conductance	71
B. Appendix	74
B.1. Scaling Analysis	74
C. Appendix	81
C.1. Elastic Scattering - Single Barrier	81

C.2. Elastic Scattering - Two Barriers	83
--	----

List of Abbreviations

AC - Alternating Current

CDW - Charge Density Wave

DC - Direct Current

DDMRG - Dynamical Density Matrix Renormalization Group

DMRG - Density Matrix Renormalization Group

1. Introduction

The area of solid state physics is one of the largest fields of physics that treats solid matter as systems of ordered atomic particles to describe their physical properties. These are usually consisting of more or less stationary atomic cores, where electrons display a much larger contribution to the dynamics of the systems [1,2]. This thesis focusses on the electronic transport in a subclass of such bodies in which the electrons are confined to reduced spatial dimensions. Especially, when the structures are close to being one-dimensional the electron transport is dominated by their fermionic quantum nature. In the three dimensional description electrons can be treated as a Fermi liquid [3] which fails to provide a viable description in one dimension. While in three dimensions nearly individual excitations of single electrons can contribute to the transport, in one dimension only collective excitations are possible because of the strong confinement [1].

1.1. Conductivity and Conductance

Here, the related quantities of conductivity and conductance are discussed for the specific case of a one-dimensional conductor. These quantities are important when one is interested in the description of a transport measurement. The derivation presented is close to Reference [3].

At first, assume that a current $j(x, \tau)$ in the one-dimensional system is generated as the linear response to an electromagnetic potential $\phi(x, \tau)$. This potential is very weak and slowly changing in space. Therefore, linear response theory allows to express the current as

$$j(x, \tau) = -\frac{q^2}{\hbar} \int_{-\infty}^{\tau} \int \chi(x - x', \tau - \tau') \phi(x', \tau') d\tau' dx', \quad (1.1)$$

where q is the electric charge and the susceptibility $\chi(x, \tau)$ is the retarded current density correlation function

$$\chi(x - x', \tau - \tau') = -i\theta(\tau - \tau') \langle [\hat{j}(x, \tau), \hat{n}(x', \tau')] \rangle. \quad (1.2)$$

Here, $\theta(\tau)$ denotes the Heaviside step function that expresses time retardation. The hat denotes the interaction picture version of the respective current probability density operator and the density operator. Fourier transforming (1.1) and using the convolution theorem delivers the k - and ω - dependent conductivity that connects

an electric field $E(k, \omega)$ to the current by

$$j(k, \omega) = \sigma(k, \omega)E(k, \omega). \quad (1.3)$$

In order to simulate a potential that is switched on adiabatically the frequency receives an additional very small and positive imaginary part δ . This ensures that for $\tau \rightarrow 0$ the contributions to the integral become smaller [4]. For homogeneous interacting fermions in one dimension Luttinger Liquid theory provides the retarded current density correlation function (1.2). Then, the momentum- and frequency-dependent conductivity can be described by

$$\sigma(k, \omega) = \frac{4q^2}{\hbar} uK \frac{i(\omega + i\delta)}{(\omega + i\delta)^2 - u^2k^2}, \quad (1.4)$$

where the Luttinger parameter K is depending on the interaction (see chapter 6) and u is the charge velocity. For the noninteracting case $K = 1$ and the charge velocity equals the Fermi velocity $u = v_{\text{F}}$. When the fermions are spinless the prefactor of 4 is replaced by 2.

There are two interesting cases regarding the electric field $E(k, \omega)$. For one the case of a periodic and uniform field $E(0, \omega)$ such that

$$\sigma(0, \omega) = \frac{4q^2}{\hbar} uK \frac{i}{\omega + i\delta}. \quad (1.5)$$

The real part of the conductivity is then

$$\begin{aligned} \text{Re}\{\sigma(0, \omega)\} &= \frac{4q^2}{\hbar} uK \frac{\delta}{\delta^2 + \omega^2}, \\ &\stackrel{\delta \rightarrow 0}{=} 2\pi D \delta(\omega), \end{aligned} \quad (1.6)$$

where D is the Drude weight

$$D = \frac{2q^2\pi}{\hbar} uK. \quad (1.7)$$

The other case is that of a static field that is spatially inhomogeneous $E(k, 0)$ and consequently

$$\begin{aligned} \sigma(k, 0) &= \frac{4q^2}{\hbar} uK \frac{\delta}{\delta^2 + u^2k^2}, \\ &\stackrel{\delta \rightarrow 0}{=} 2\pi G \delta(k), \end{aligned} \quad (1.8)$$

with the conductance

$$G = \frac{2q^2}{h}K. \quad (1.9)$$

Note that $\sigma(k, 0)$ is already a real conductivity. In the special case of noninteracting fermions $G = G_0$. This is the so called quantum of conductance that is also mentioned in chapter 5.

$$G_0 = \frac{q^2}{h}. \quad (1.10)$$

These two cases describe two different measurements. The first case would need a field with finite frequency over the finite length of the probe that will measure the conductivity $\sigma(0, \omega)$. The second case is realized by applying the field only over a part of the sample. Here, the wavenumber dependent conductivity $\sigma(k, 0)$ is probed. These two cases become relevant when in chapter 2 the shape of an applied perturbation is discussed. The conductance is what is usually measured in a transport measurement as seen in Figure 2. Therefore, the second case is preferred. The conductance takes the length over which the electromagnetic field is applied L into account as can also be seen if one compares the units in equation (1.8). In the DC-limit $\omega \rightarrow 0$ the linear DC-conductance G follows the relation

$$G_{\text{Lin}} = \lim_{\omega \rightarrow 0} \frac{\sigma(k, \omega)}{L} = \lim_{\omega \rightarrow 0} \frac{j(k, \omega)}{LE(k, \omega)} = \lim_{\omega \rightarrow 0} \frac{j(k, \omega)}{V_{\text{SD}}(k, \omega)}, \quad (1.11)$$

where the electric field over only a section of the probe is the result of a source-drain voltage $V_{\text{SD}}(k, \omega)$. This is the definition of the linear DC-conductance, but there also exists a definition for the differential conductance. I will assume a small source-drain voltage such that only states at the Fermi edge contribute to the transport. In this limit both definitions are equal. Separating the frequency dependency from the source-drain voltage and using $j(\omega) = \text{Re}\{q \langle J(\omega) \rangle\}$ leads to the final expression for the DC-conductance

$$G = \lim_{\omega \rightarrow 0} \lim_{V_{\text{SD}} \rightarrow 0} \text{Re} \left\{ \frac{q \langle J(\omega) \rangle}{V_{\text{SD}} f(\omega)} \right\}. \quad (1.12)$$

The heart of this equation is the expectation value $\langle J(\omega) \rangle$ that is a linear response to perturbation as in equation (1.1). In appendix A.1 I show how to derive this expression and in appendix A.2 the resulting DC-conductance [5]. Treating the current as a linear response to a perturbation is also known as the Kubo formalism [4, 6] and consequently the description for the conductance that is obtained by using this approach is called the Kubo-conductance (see Appendix A.2) [7]. This formulation of the conductance is the one I will use throughout this thesis for a model that uses

finite chains with discrete sites.

The approach is based on the assumption that a limited amount of orbitals in a linear chain can be occupied by electrons that are contributing to the transport. An electron can then hop from one orbital into a neighboring orbital, but has to respect Pauli's principle and interactions. There are several theoretical models that include different kinds of interactions and degrees of freedom. Most famous examples are the simple tight-binding model of spinless fermions [8], the spinful Hubbard model [9, 10] and the Holstein model [11], that includes vibrations in the form of additional Einstein phonons. The problems inherent to these models is that their chains would have to consist of infinitely many links in order to describe a realistic experiment in the thermodynamic limit. In the next two chapters I explain how the systems I am using are modelled and how the problem of the thermodynamic limit is overcome.

1.2. Setup

In this section the general transport setup and ways to model specific systems are discussed. A realization of the concept of one-dimensional wires can be found in semiconductor wires [12], carbon nanotubes [13] and atomic wires that are deposited on a substrate [14, 15] and atomic and molecular wire junctions [16–19].

A transport measurement on these objects is performed by attaching metal fingers on each side of the wire serving as leads. The setup is then exposed to a source- and drain voltage which is transferred through the leads into the wire. In the leads and the wire this results in a local electric field that gives rise to a current. Usually these structures are very fragile and therefore the wires can only be created in very short lengths in the nanometer regime.

Fig. 1 and Fig. 2 are two examples of different quantum wires in an actual experiment. The images are taken from the two experimental groups in [20] and [21]. In both pictures the thin wire structure is attached to the mentioned leads that are of much bigger proportions.

In the first figure the probed object is a semiconducting carbon nanotube. The research group measured the conductance of the setup at different temperatures. Their measurements indicate that the resistance is dominated by the channel resistance of the device and not the contact resistance. However they argue that for specific gate voltages other mechanisms like Schottky barriers forming at the contacts might take over the dynamics [22]. They also derive that the conductivity of the carbon nanotube may be tunable from an insulator up to that of a good conducting metal.

The second experiment was conducted with a semiconductor nanowire with the

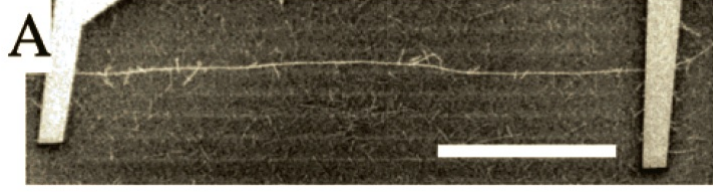


Figure 1: The picture shows a very thin semiconductor nanotube transistor by field-emission scanning electron micrographs. On both sides of the wire there are metallic Au/Cr leads attached. The scale bar possesses a length of $100\mu m$. The figure is adapted from Ref. [20]

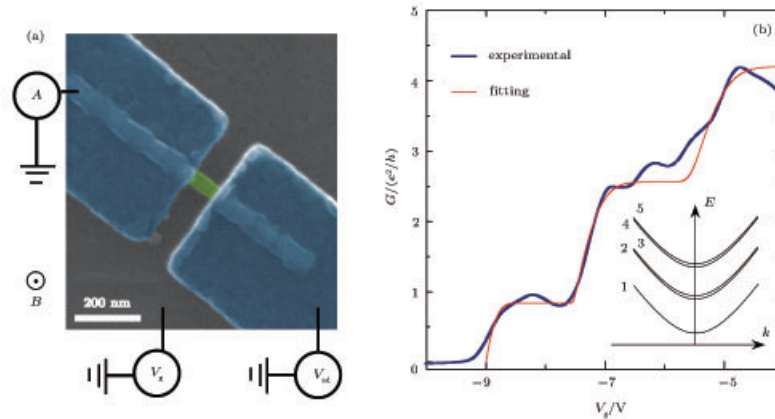


Figure 2: Example of nanowire transport setup. On the left there is a false color SEM-Image of InSb nanowire that is connected to Ti/Al leads. On the right hand side the depiction shows the measured conductance for different values of gate-voltage. This image is adapted from Ref. [21]

long term goal in mind to use them in nanoelectronics [23]. The group was measuring the ballistic transport in an InSb nanowire. The results were the characteristic plateaus in the conductance and were found consistent with the Landauer approach [24].

In conclusion, these transport experiments serve as example setups and show that they can be represented by a lead-wire system. In the next section I discuss how the setup is modelled into a one-dimensional finite chain taking into account the essential characteristics described so far. I also layout the concept that allows studying finite systems in order to gain insight into the thermodynamic limit behavior.

1.3. Model and Outline

As mentioned in the introduction about conductivity and conductance 1.1 this part is dedicated to the explanation of how a lead wire structure can be mapped into a one-dimensional finite chain. The last two sections provided the insight in the characteristics of an experimental transport setup. The following properties are of

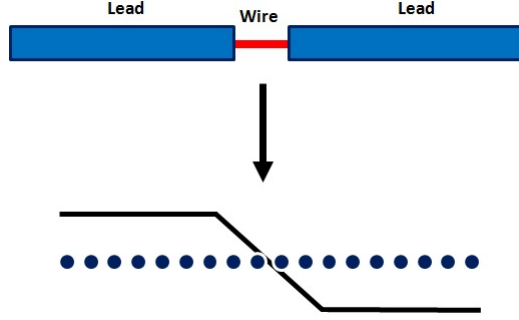


Figure 3: Schematics for the mapping of the experimental lead-wire setup into a one-dimensional chain and applied potential.

importance.

- The setups consists of two leads and one wire section.
- The lead structure has much bigger proportions then the quantum wire.
- A source- and drain voltage is applied to the two leads and falls off over the wire section.
- The current is generated by the voltage through an effective electric field.

The influence of the source and drain voltage will be treated as perturbation to the equilibrium system. The equilibrium Hamiltonian of the system will be called H_0 and the time dependent perturbation that is responsible for the dynamics $\delta H(\tau)$ such that the total system Hamiltonian is the combined

$$H(\tau) = H_0 + \delta H(\tau). \quad (1.13)$$

At first, a base system will be modelled for the setup in equilibrium. For simplicity the kinetic movement of the electrons will be restricted to nearest neighbor hopping such that the kinetic part of H_0 for a chain of M sites would be

$$H_{\text{Kin}} = - \sum_{j=2}^M \sum_{\sigma} t(j) \left(c_{j,\sigma}^{\dagger} c_{j-1,\sigma} + \text{h.c.} \right). \quad (1.14)$$

$c_{j,\sigma}^{\dagger}$ and $c_{j,\sigma}$ denote the fermionic operators that create or annihilate a fermion at position j . The so called hopping amplitude $t(j)$ determines the likelihood of one site hopping process from site $j-1$ to j . Most of the time it is not necessary to use spinfull electrons to explain certain behaviors of the setup as explained later in this thesis. In this case, there will not be a summation over the spin parameter.

In addition electrons can interact in the form of the Coulomb interaction where the strength can be described by the nearest neighbor interaction parameter V

or for spinfull fermions by U . The Hamiltonian part for the Coulomb interaction depending on whether a spinfull model is used or not then reads

$$H_{C1} = V \sum_{j=2}^M \left(n_j - \frac{1}{2} \right) \left(n_{j-1} - \frac{1}{2} \right), \quad (1.15)$$

$$H_{C2} = U \sum_{j=1}^M n_{j,\uparrow} n_{j,\downarrow}. \quad (1.16)$$

The number operator $n_{j,\sigma} = c_{j,\sigma}^\dagger c_{j,\sigma}$ counts the fermions of spin σ at site j or in the spinless case $n_j = c_j^\dagger c_j$ the number of fermions.

The chain splits naturally into three regions that consist of one wire section in the middle and the two leads in the outer parts. This separation is due to the different material or the difference in dimensionality and size. The differentiation could be modelled in various ways. For example the hopping amplitudes $t(j)$ or the interaction between the electrons could be different for the three regions. In this thesis most of the time the three sections are accounted for by the shape of the potential of the perturbation as seen in Fig. 3 and in one specific case by different interactions for the wire and leads in chapter 7. Therefore, the hopping amplitude will always be constant $t(j) = t$.

Another degree of freedom that can be taken into account would be vibrations. A setup as seen in Figure 2 may be subject to vibrations that can be modelled in the form of quasi particles called phonons. These bosons could manifest at each site and could be described in the form of a phonon Hamiltonian

$$H_{\text{Phonon}} = \omega_b \sum_{j=1}^M b_j^\dagger b_j - g \omega_b \sum_{j=1}^M \left(b_j^\dagger + b_j \right) n_j, \quad (1.17)$$

where b_j^\dagger and b_j are the boson creation and annihilation operators that either create or destroy a phonon at site j . ω_b is associated with the phonon frequency. Via coupling g an electron at site j is able to create phonons at the same site.

The next step is to define the form of the perturbation. $\delta H(\tau)$ will be composed as

$$\delta H(\tau) = e V_{\text{SD}} f(\tau) A. \quad (1.18)$$

Here e stands for the electron charge and V_{SD} the source and drain voltage. $f(\tau)$ is function that represents a slow oscillation of the electric field in time τ . A is the operator that couples the field to the fermions. That means it is composed of fermion number operators $n_{j,\sigma}$ and also describes the shape of the potential. How the shape of the potential is chosen and the consequences of this choice is discussed

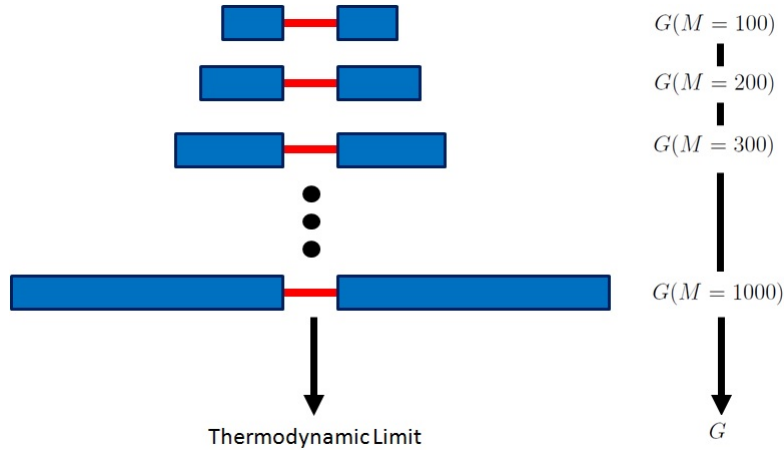


Figure 4: Schematics of the iteration process to reach the DC-conductance in the thermodynamic limit by enlarging finite setups and calculating their finite broadened conductance.

in the next chapter.

The next question is how to determine the conductance of such a linear chain that is composed of these sub-parts in the thermodynamic limit. Analytically even for finite chains the theoretical methods are quite limited. However, I will rely on one of the most powerful numerical methods, the Density Matrix Renormalization Group (DMRG) [25–28]. The algorithm works especially well in one dimension as later explained in detail in section 3.

In Figure 4 the concept for reaching the thermodynamic limit is depicted in form of a schematic. At first, the DC-conductance for a system of length M is calculated. The system then is grown in size. During the enlargement the wire stays at a constant length. The DC-conductance is calculated for the bigger system. This continues for systems as big as the DMRG can handle. In the end the values can be extrapolated from the finite systems into the thermodynamic limit.

This might sound easier than it is in practice. The DC-conductance for finite systems has discrete spectra, but for the limit of an infinite chain, these spectra are expected to be continuous. For this reason the spectra have to be broadened in order to prepare an extrapolation. The full process is explained later in section 4.2.

One might now assume that the combination of the three sub parts form a suitable base Hamiltonian

$$H_0 = H_{\text{Kin}} + H_{\text{C1/2}} + H_{\text{Phonon}}. \quad (1.19)$$

In practice, this is not feasible because of the computational demand each of these parts contribute to the numerical calculations. It is far more pragmatic to use

smaller combinations like

$$H_0 = H_{\text{Kin}} + H_{\text{C1}}, \quad (1.20)$$

$$H_{\text{Hubbard}} = H_{\text{Kin}} + H_{\text{C2}}. \quad (1.21)$$

to study the effects of different Coulomb interaction onto the conductance. Or if interested in the influence of phonon interactions one might use

$$H_{\text{Holstein}} = H_{\text{Kin}} + H_{\text{Phonon}}. \quad (1.22)$$

Since, now the underlying concept and the model are elaborated I will discuss the shape of the perturbation that is ultimately responsible for the charge current (2nd chapter). This will be followed by the introduction of the Density Matrix Renormalization Group algorithm (3rd chapter). Based on this introduction the algorithm is extended to the Dynamical Density Matrix Renormalization Group for the special problem of quantities that are the linear response to a perturbation. In addition, the finite size scaling is explained that is necessary to extrapolate the DC-conductance of finite systems into the thermodynamic limit. After clarifying the model details the new method will be used in the fourth chapter for a one-dimensional Fermi gas for which the behavior can be calculated analytically. This serves as verification process for the viability of the procedure. The method will be further applied to several different configurations, in the Luttinger liquid regime of homogeneous interaction in chapter 6, in the inhomogeneous regime in chapter 7, for the noninteracting chain that is coupled to phonons, also known as Holstein model in chapter 8 and finally the Hubbard model of spinfull fermions in chapter 9.

In summary, the extension into more complex systems serves the purpose to model realistic experiments conducted with one-dimensional electronic conductors [12–19].

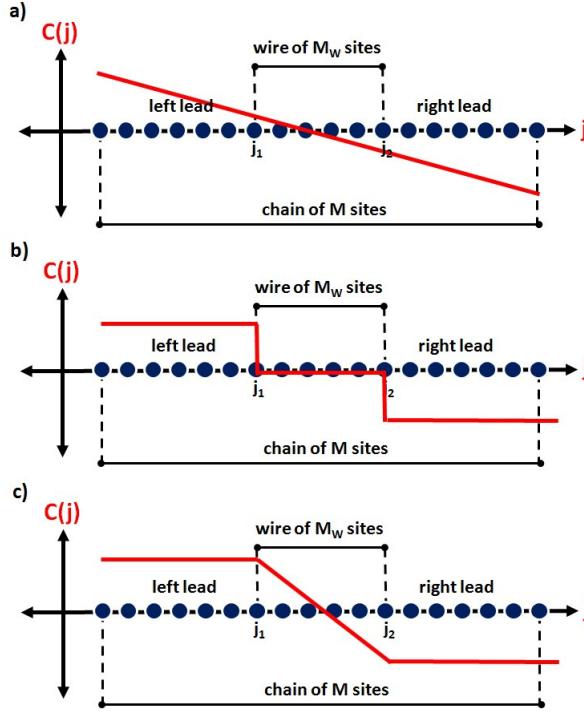


Figure 5: Schematics for homogeneous one-dimensional chains of fermion sites that are numbered by j . The first and last wire sites are named j_1 and j_2 . The three depictions show different shapes $C(j)$ of the applied electric potential. Only in depiction b) and c) the wire regions are distinct from the leads through the shape of the perturbation. Schematics c) was adapted from Ref. [33]

2. Shape of the Perturbation

As pointed out in the first chapter, the main focus of interest is the dynamic behavior of a quantum wire. In the previous chapter the quantity of conductance was introduced. In Appendix A.2 the formula of the Kubo-conductance [5, 7] $G(\omega)$ is derived by using linear response theory such that

$$G(\omega) = \lim_{\eta \rightarrow 0^+} \frac{q^2}{\omega} \sum_m |\langle 0 | J | m \rangle|^2 \left(\frac{\hbar\eta}{(E_m - E_0 - \hbar\omega)^2 + (\hbar\eta)^2} - \frac{\hbar\eta}{(E_m - E_0 + \hbar\omega)^2 + (\hbar\eta)^2} \right). \quad (2.1)$$

Since $\dot{A} = J$, that means that the current operator is equivalent to

$$J = \frac{i}{\hbar} [H, A] = \frac{i}{\hbar} [H_0, A]. \quad (2.2)$$

Usually, the Hamiltonian for relevant systems H_0 can be separated into two parts, where the first part is the kinetic term and the second part is dependent on some

combination of number operators: $c_i^\dagger c_i = n_i$.

$$H_0 = - \sum_{j=2}^N t(j)(c_j^\dagger c_{j-1} + c_{j-1}^\dagger c_j) + \sum_{i=1}^N \Theta(n_i, n_{i-1}). \quad (2.3)$$

In addition, a perturbation is added according to equation (1.18). The operator of the perturbation A will also consist of a combination of single site number operators such that

$$A = \sum_{i=1}^N C(i)n_i. \quad (2.4)$$

$t(j)$ and $C(i)$ can be set to zero if necessary and the Θ denotes the parts of the Hamiltonian that only contains combinations of number operators. They can be ignored, because they commute as

$$[c_j^\dagger c_k, n_i] = \begin{cases} 0, & \forall i \neq j, k \\ 0, & \forall j = k \\ -c_i^\dagger c_k, & \forall i = j \neq k \\ c_j^\dagger c_i, & \forall i = k \neq j \end{cases}. \quad (2.5)$$

With that in mind the commutator in (2.2) reads

$$J = \frac{i}{\hbar} [H_0, A] = \frac{i}{\hbar} \left[- \sum_{j=2}^N t(j)(c_j^\dagger c_{j-1} + c_{j-1}^\dagger c_j) \quad , \quad \sum_{i=1}^N C(i)n_i \right] = \sum_{i=2}^N \Delta C(i) J_i, \quad (2.6)$$

with $\Delta C(i) = C(i) - C(i-1)$ and the probability current operator J_i defined as

$$J_i = \frac{i}{\hbar} t(i)(c_i^\dagger c_{i-1} - c_{i-1}^\dagger c_i). \quad (2.7)$$

It is worth to note that a positive current expectation value $\langle J \rangle$ by this definition in (2.6) describes a current from the left to the right direction of the chain if one were to allow only positive values for $t(j)$.

The question arises how to choose the shape of the applied external potential $C(i)$, in order to model a transport measurement. For example a linear potential drop over the chain as seen in Figure 5 a) would definitely generate a positive current(for an infinite chain), although it still might be suppressed by the other parts of the

Hamiltonian. That would mean

$$A_{\text{Linear}} = \sum_{i=1}^N C_{\text{Linear}} n_i(i), \quad (2.8)$$

$$C_{\text{Linear}}(i) = \left(-\frac{i-1}{N-1} + \frac{1}{2} \right), \quad (2.9)$$

$$\Delta C_{\text{Linear}}(i) = -\frac{1}{N-1}, \quad (2.10)$$

which results in the respective J_{Linear}

$$J_{\text{Linear}} = -\sum_{i=2}^N \frac{1}{N-1} J_i. \quad (2.11)$$

An apparent downside of this shape is, that for a homogeneous non-interacting chain there is no distinction between lead and wire parts. Then, the effective current operator (2.11) is simply the sum over all the single site currents normalized by the length of the chain.

In order to emphasize the different constituents of the setup a different shape for the applied external potential can be selected. A more step like perturbation that is constant over the lead sections and zero in the wire section as seen in Figure 5 b) would encourage a current but keep the distinction between different chain parts preserved. Therefore, the effective current would be formed through

$$A_{\text{Step}} = \sum_{i=1}^N C_{\text{Step}}(i) n_i, \quad (2.12)$$

$$C_{\text{Step}}(i) = \begin{cases} \frac{1}{2} & \text{for } i < j_1, \\ -\frac{1}{2} & \text{for } i \geq j_2, \\ 0 & \text{else,} \end{cases} \quad (2.13)$$

$$\Delta C(i)_{A_{\text{Step}}} = \begin{cases} -\frac{1}{2} & \text{for } i = j_1, \\ -\frac{1}{2} & \text{for } i = j_2, \\ 0 & \text{else.} \end{cases} \quad (2.14)$$

into J_{Step}

$$J_{\text{Step}} = -\frac{1}{2}(J_{j_1} + J_{j_2}). \quad (2.15)$$

The effective current only depends on the two sites where the potential drops.

A scaling analysis that uses the correlator (5.15) that is calculated in chapter 5 reveals that A_{Linear} leads to a measurement of the Drude weight and not the conductance. This corresponds to the conductivity of equation (1.6) where the electric

field is uniformly distributed over the sample. A_{step} on the other leads to a scaling that is proportional to the conductance in the leading order corresponding to equation (1.8). For this thesis I decided to take a mixture of the A_{linear} and the A_{step} according to Figure 5 c) where I have a constant potential over the lead sections and a linear drop in the middle of the setup over the wire. This shape prevents probing the Drude weight and still takes a more realistic approach of a dropping voltage over the wire.

At the same time this distinguishes the wire from lead sections, even in the homogeneous interacting setup

$$A_{\text{Mixed}} = \sum_{j=1}^N C_{\text{Mixed}}(j)n_j, \quad (2.16)$$

$$C_{\text{Mixed}}(j) = \begin{cases} \frac{1}{2} & \text{for } j \leq j_1, \\ -\frac{j-j_1}{j_2-j_1} + \frac{1}{2} & \text{for } j_1 < j < j_2, \\ -\frac{1}{2} & \text{for } j \geq j_2, \end{cases} \quad (2.17)$$

$$\Delta C(j)_{A_{\text{Mixed}}} = \begin{cases} -\frac{1}{M_W-1} & \text{for } j_1 < j \leq j_2, \\ 0 & \text{else.} \end{cases} \quad (2.18)$$

Therefore, the effective current for the mixed field is

$$J = -\frac{1}{M_W-1} \frac{i}{\hbar} \sum_{j_1+1}^{j_2} t(j)(c_j^\dagger c_{j-1} - c_{j-1}^\dagger c_j). \quad (2.19)$$

This operator has the other computational advantage, that it does not scale with M like J_{Linear} , but with M_W , which is the number of wire sites and therefore the length of the wire section. This is very beneficial during the enlargement of the finite scaling process described later in this thesis, because the wire length is held constant.

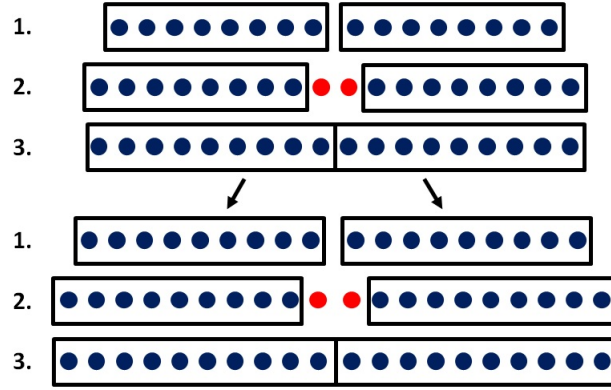


Figure 6: The figure shows a schematic depiction of the infinite-system DMRG algorithm. Step 1. starts with two blocks. In step 2. two new sites are added. In step 3. these are incorporated into a superblock. The Hilbert space that represents the superblock is truncated. The algorithm then turns back to step 1. by splitting up the new superblock into two blocks.

3. Density Matrix Renormalization Group

In the previous chapter the modelling of the setup into one-dimensional chains of M sites was discussed. The physics of this setup can be described by a Hilbert space of d^M dimensions, where d denotes the local Hilbert space dimension of a single site. It is easy to see that for big site number M the Hilbert space becomes too large to handle. Therefore, the Density Matrix Renormalization Group (DDMRG) algorithm is introduced as numerical method that can reduce the Hilbert space to a dominant subspace. The subspace then contains enough information to determine the physics of the transport properties. This decimation process works especially well in the present case of one-dimensional short-range Hamiltonians. The explanation I present here is very close to the reference of Ulrich Schollwöck [27] who not only delivers a good introduction to the field of DMRG, but also connects it to the field of matrix product states.

The DMRG can be split into two kinds of DMRG procedures. The first is the infinite-system DMRG in which the system size is continuously growing, and the second the finite-system DMRG where the total system size stays constant. These two types are explained in detail in the following sections. In practice these two versions are combined into one by using the infinite-system DMRG as preparation until the desired system size is reached and then one switches to the finite-system DMRG that keeps the system at the desired size.

3.1. Infinite-system DMRG

The infinite-system DMRG employs iterations as depicted in Figure 6. As seen in the figure the algorithm can be divided into three substeps. At first a system of size M is split into two blocks. The smallest system to start with would consist of only $M = 2$ sites that is then split into a left and right block. In the next step two new sites are inserted in between the two blocks such that the total system grows by two sites. The sites are then absorbed into new left and right blocks that effectively grow by one site each. While this procedure continues the total system size is growing by two and the sub-block size by one, whenever this three substeps are executed.

The Hilbert space of the complete system can either be described through the basis of the two blocks, $\{|i\rangle_L\}$ for the left block and $\{|j\rangle_R\}$ for the right block, or by treating the two single sites in the middle of the wire isolated by using the tensor product of the sub-block states $\{|a\rangle_L\}$ and $\{|a\rangle_R\}$ and the local basis of the two sites $\{|s\rangle_L\}$ and $\{|s\rangle_R\}$. Any state $|\psi\rangle$ of the system can therefore be expressed as

$$|\psi\rangle = \sum_{i_L, j_R} c_{i_L, j_R} |i\rangle_L |j\rangle_R = \sum_{a_L, s_L, s_R, a_R} c_{a_L, s_L, s_R, a_R} |a\rangle_L |s\rangle_L |s\rangle_R |a\rangle_R. \quad (3.1)$$

For small block sizes the Hilbert space might actually be small enough to be handled by the numeric resources available. But once, a certain size is reached a truncation back to a Hilbert space of maximum dimension D has to be performed. If one is interested in the ground state of the system $|0\rangle$ one can minimize the functional

$$E(\psi) = \frac{\langle \psi | H | \psi \rangle}{\langle \psi | \psi \rangle} \quad (3.2)$$

with respect to ψ , where the Hamiltonian is expressed in the basis of the combined blocks. Since the systems of interest are one-dimensional with short range interactions most matrix elements of the Hamiltonians are zero which opens up possibilities to use sparse Eigensolver techniques. This usually happens in the form of diagonalization algorithms like the powerful Lanczos algorithm [29].

When the system is now enlarged and a single site of local dimension d is added to the basis of the former left block the Hilbert space dimension for the complete left side would grow from D to dD , because the former left block takes over the role of the new sub-block. In order to calculate the targeted state $|\psi\rangle$ one now has to minimize 3.2 in the basis (3.1) of dimension $D^2 d^2$. At this point the basis that is used has to be truncated, because the limit was set to a maximum of D dimensions for a block. This happens by first forming the reduced density operator for the

combination of sub-block and single site

$$\rho_{(L+\text{site})} = \mathbf{Tr}_{(\text{site}+R)} |\psi\rangle \langle\psi|, \quad (3.3)$$

$$\rho_{(L+\text{site})ii'} = \sum_j c_{i,j} c_{i',j}^*. \quad (3.4)$$

Diagonalizing the reduced density operator and then ordering the resulting eigenstates by their eigenvalues allows to determine the eigenstates with the most influence on the system. Only the D most influential eigenstates $\{|b\rangle\}$ are kept to determine the new basis for the left block $\{|i\rangle_L\}$ by expanding with the coefficients that are formed by $\langle a|_L \otimes \langle s|_L |b\rangle$.

The question arises why forming the reduced density matrix and then diagonalizing it will actually provide a good representation for the truncated system. Still following the explanation in Ref. [27] at first the linear algebra method of the singular-value-decomposition(SVD) has to be introduced. It states that any rectangular matrix Ψ of dimensions $(m \times n)$ can be decomposed into three matrices by

$$\Psi = USV^\dagger. \quad (3.5)$$

The matrices U and V have the properties

$$U^\dagger U = I, \quad (3.6)$$

$$VV^\dagger = I. \quad (3.7)$$

U is completely unitary if $m \leq n$ and V is unitary if $n \leq m$. The matrix S on the other hand is diagonal, where the diagonal values are all positive and can be listed and ordered as $S_{aa} = s_a$. The s_a are called singular values and are assumed to be ordered by size, such that the biggest value is the first entry of S .

A system that is split into a left(L) and right part(R) can be described by a pure state

$$|\psi\rangle = \sum_{ij} c_{ij} |i\rangle_L |j\rangle_R. \quad (3.8)$$

Here, $\{|i\rangle_L\}$ and $\{|j\rangle_R\}$ are orthonormal bases for the left and right side of dimensions m and n . Let's assume a matrix Ψ as described in equation (3.5) consists of the coefficients c_{ij} of the pure state. Then the pure state can be rewritten by using the

SVD to

$$|\psi\rangle = \sum_{ij} \sum_{a=1}^{\min(m,n)} U_{ia} S_{aa} V_{ja}^* |i\rangle_L |j\rangle_R, \quad (3.9)$$

$$= \sum_{a=1}^{\min(m,n)} s_a \left(\sum_i U_{ia} |i\rangle_L \right) \left(\sum_j V_{ja}^* |j\rangle_R \right), \quad (3.10)$$

$$= \sum_{a=1}^{\min(m,n)} s_a |a\rangle_L |a\rangle_R. \quad (3.11)$$

When the sum now is not completely executed and only the r first terms that are associated with the largest s_a are taken into account the result is the so called Schmidt decomposition.

$$|\psi\rangle = \sum_{a=1}^r s_a |a\rangle_L |a\rangle_R. \quad (3.12)$$

Using this decimated version of the pure state the reduced density operators are formed for the left and right block by

$$\rho_L = \Psi \Psi^\dagger = \sum_{a=1}^r s_a^2 |a\rangle_L \langle a|_L, \quad (3.13)$$

$$\rho_R = \Psi^\dagger \Psi = \sum_{a=1}^r s_a^2 |a\rangle_R \langle a|_R. \quad (3.14)$$

The surprising result is that the eigenvalues directly present themselves as s_a^2 . To answer the earlier question, it turns out that to ask if a truncated state $|\psi'\rangle$ is a good approximation to $|\psi\rangle$ can be done by relating the 2-norm of $|\psi\rangle$ to the Frobenius matrix norm by

$$\| |\psi\rangle \|_2^2 = \sum_{ij} |c_{ij}|^2 = \|\Psi\|_F^2. \quad (3.15)$$

The consequence is that the optimal approximation of $|\psi\rangle$ by $|\psi'\rangle$ in the 2-norm can be found by the optimal approximation of a matrix Ψ through Ψ' in the Frobenius norm. Constructing Ψ' as

$$\Psi' = U S' V^\dagger, \quad (3.16)$$

where S' is consisting of the r biggest singular values of Ψ on the diagonal and a rest of zeros. This is the optimal approximation for a matrix in the Frobenius norm.

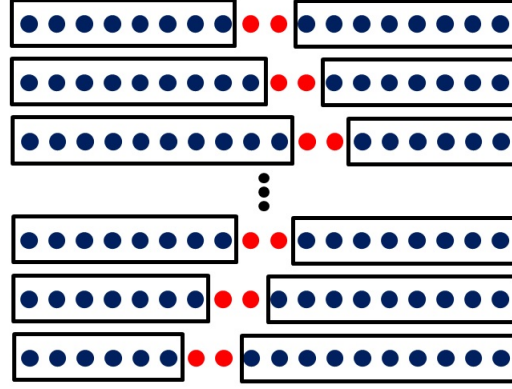


Figure 7: Here the iteration of the finite-system DMRG is depicted. In contrast to the infinite-system DMRG the enlargement of one of the subsystems by incorporating the single sites is simultaneous to the shrinking of the other subsystem, such that the total system size stays the same at every step.

It means the optimal approximation for a state $|\psi\rangle$ is

$$|\psi'\rangle = \sum_{a=1}^{r'} s_a |a\rangle_L |a\rangle_R. \quad (3.17)$$

Therefore, forming the reduced density matrices like in equation (3.3) and equation (3.4) is doing exactly this and delivering the optimal approximation.

3.2. Finite-system DMRG

The finite-system DMRG depicted in Figure 7 is the next procedure that is executed after the infinite-system DMRG. When the desired system size is reached the growing process of the infinite-system DMRG can be stopped and a sweeping process through a system that stays constant in size called finite-system DMRG is continued. In contrast to the previous type of DMRG the growing process of one block happens at the expense of the other block(ensuring the constant system size). During the process of forming the reduced density operator the infinite-system DMRG effectively assumed an environment of the same size as the block it was formed for. Here, in the finite-system DMRG this assumption gets corrected by composing the environment only from the available "left over" block. This correction leads for most non trivial systems to a drastic change in results. When the sweeping starts a block is enlarged and the reduced density matrix uses a shrunk version of the other block. The growth of one block and reduction of the other block continues until a dimensional limit for the Hilbert space is reached or the environment block is consisting of a single site. Now the small block takes over the role of the growing block and the direction of the growth and reduction is reversed. During this sweep process a lot

of the blocks have already been calculated in previous iterations. Therefore, these can be stored and reused to save computation time.

4. Finite Size Scaling DDMRG

In Appendix A.2 the frequency dependant Kubo-conductance was derived. Recalling the formula (2.1)(here $\hbar = 1$) shows that the center of interest lies within the correlator $|\langle m|J|0\rangle|^2$.

$$G(\omega) = \lim_{\eta \rightarrow 0^+} \frac{q^2}{\omega} \sum_m |\langle m|J|0\rangle|^2 \left(\frac{\eta}{(E_m - E_0 - \omega)^2 + \eta^2} - \frac{\eta}{(E_m - E_0 + \omega)^2 + \eta^2} \right). \quad (4.1)$$

It determines the weight of the m -th distribution of symmetric Lorentzians around the origin. For very simplistic systems like the non-interacting tight-binding setup it is actually possible to calculate the correlator analytically, but once the system becomes more complex this does not work anymore. At this point numeric methods like the DMRG presented in the last section have to be relied on.

Additionally, it should be noted that although I will call this quantity the frequency dependant conductance throughout the thesis it is only in the DC-limit $\omega \rightarrow 0$ confirmed to be equivalent to the real DC-conductance G_{exp} that is obtained in an actual measurement. It was never investigated what happens for other frequencies, such that

$$\begin{aligned} G(\omega) &\stackrel{?}{=} G_{\text{exp}}(\omega), \\ \lim_{\omega \rightarrow 0} G(\omega) &= G_{\text{exp}}(0). \end{aligned} \quad (4.2)$$

This means that $G(\omega)$ will only be used in the DC-limit when describing a transport measurement.

The entire chapter 4 is focused on the numeric evaluation of this expression. It is divided into two parts. The first section introduces the Dynamical Density Matrix Renormalization Group Algorithm(DDMRG) from Ref. [30,31] which is an extension to the DMRG algorithm and it is pointed out why it works so well with this kind of dynamic quantities. In the second part the actual method is presented of scaling finite setups in combination with DDMRG to reach the thermodynamic limit of the DC-conductance G .

4.1. Dynamical Density Matrix Renormalization Group

The dynamical variant of DMRG published in Ref. [30,31] is explained here. This algorithm will be of great use to numerically evaluate correlation functions like the one found in conductance in (4.1). As mentioned in the papers this method focusses on the class of correlation functions that are the result for a response of a system to a

time dependent perturbation. This set of correlation functions follows the structure

$$G_O(\omega + i\eta) = \langle 0 | O^\dagger \frac{1}{E_0 - H + \omega + i\eta} O | 0 \rangle, \quad (4.3)$$

where O is the operator, that is observed. Therefore, in the present case the operator O can directly be replaced by the current operator J .

Looking at the imaginary part of this equation yields

$$\text{Im}(G_J(\omega + i\eta)) = \langle 0 | J^\dagger \frac{\eta}{(E_0 - H + \omega)^2 + \eta^2} J | 0 \rangle. \quad (4.4)$$

This is exactly the correlator, that is the building block of the frequency dependent conductance (4.1). Once there is a way to calculate this correlator the frequency dependent conductance can be easily obtained.

Following the References [30, 31] I continue by introducing a correction vector $|\psi_J(\omega + i\eta)\rangle$, that helps to express the correlator as

$$\text{Im}(G_J(\omega + i\eta)) = - \langle 0 | J^\dagger |\psi_J(\omega + i\eta)\rangle, \quad (4.5)$$

$$\text{with } |\psi_J(\omega + i\eta)\rangle = \frac{1}{E_0 - H + \omega + i\eta} J | 0 \rangle. \quad (4.6)$$

The correction vector can be written as the sum of two parts,

$$|\psi_J(\omega + i\eta)\rangle = |X_J(\omega + i\eta)\rangle + i |Y_J(\omega + i\eta)\rangle, \quad (4.7)$$

which are connected through the equation

$$|X_J(\omega + i\eta)\rangle = \frac{H - E_0 - \omega}{\eta} |Y_J(\omega + i\eta)\rangle. \quad (4.8)$$

Although these do not have to be the actual real and imaginary parts of $|\psi_J(\omega + i\eta)\rangle$. In general both might be complex. Nevertheless, the second part is useful, because it is related to the correlator by

$$\text{Im}(G_J(\omega + i\eta)) = - \langle 0 | J | Y_J(\omega + i\eta) \rangle. \quad (4.9)$$

$|Y_J(\omega + i\eta)\rangle$ can be obtained by solving the inhomogeneous linear equation

$$((E_0 - H + \omega)^2 + \eta^2) |\psi\rangle = -\eta J | 0 \rangle. \quad (4.10)$$

A common way to solve equations like this is to minimize a functional with respect

to ψ

$$W_{J,A}(\omega, \psi) = \langle \psi | ((E_0 - H + \omega)^2 + \eta^2) | \psi \rangle + \eta \langle 0 | J^\dagger | \psi \rangle + \eta \langle \psi | J | 0 \rangle. \quad (4.11)$$

The resulting $|\psi_{\min}\rangle$ is

$$|\psi_{\min}\rangle = |Y_J(\omega + i\eta)\rangle. \quad (4.12)$$

The functional for the minimal ψ_{\min} is related to the correlator (4.4) by

$$W_{J,A}(\omega, \psi_{\min}) = -\eta \text{Im}(G_J(\omega + i\eta)) \quad (4.13)$$

These are all the relations needed to calculate the frequency dependent conductance (4.1). The algorithm uses three steps, that are important for the thesis method. The first two steps are equivalent to, what a normal DMRG program explained in chapter 3 does, while the third contains the dynamical part concerning the functional $W_{J,A}(\omega, \psi)$.

1. Since DDMRG is based on the normal DMRG algorithm it starts by minimizing the energy functional

$$E(\psi) = \frac{\langle \psi | H | \psi \rangle}{\langle \psi | \psi \rangle} \quad (4.14)$$

and looking for a good approximation to the ground state $|0\rangle$ according to chapter 3.

2. $|0\rangle$ then is used to calculate $J|0\rangle$. The action of J onto the ground state is the right half of the expression (4.9).
3. By minimizing the functional $W_{J,A}(\omega, \psi)$ with respect to ψ in this part one can directly obtain the correlation function of interest $\text{Im}(G_J(\omega + i\eta))$ via (4.13).

All these steps together open up the possibility to calculate (4.1) via

$$G(\omega) = \lim_{\eta \rightarrow 0^+} \frac{q^2}{\omega} [\text{Im}(G_J(\omega + i\eta)) - \text{Im}(G_J(-\omega - i\eta))] \quad (4.15)$$

Note: The article referenced [30] describes a fourth step, which completes the correction vector via equation (4.8). But since I am only interested in the imaginary part of the correlation function, the results of the first three steps are sufficient for the thesis' method.

In a previous study [32] Bohr et al. evaluated equation (4.15) analytically which lead to a different correlator that is effectively the derivative of equation (4.4) with

respect to ω . Thus, they were able to evaluate the conductance directly at $\omega = 0$ by also using DMRG. For the correlator in this thesis this is not possible. Here, DDMRG is used as described above for a narrow frequency interval around $\omega = 0$ and then (4.15) calculated numerically for $\omega \rightarrow 0$. This approach allows to calculate the conductance for systems up to a size of $M = 2000$ sites with less than 200 eigenstates kept in the density-matrix, while Bohr et al. in Ref. [32] used system lengths up to $M = 200$ sites that kept 1200 density-matrix eigenstates.

The factor $1/\omega$ seems at first to be problematic for calculating equation (4.15), but it is in fact the derivative of equation (4.4) for $\omega \rightarrow 0$. When the limit $\eta \rightarrow 0$ is taken properly the expression is smooth around $\omega = 0$. A problem arises for finite systems as are studied in this thesis where the system size is fixed to a maximum number of M sites. This can be overcome by using a proper finite-size scaling that is introduced in the next section.

4.2. Converting DDMRG Output into broadened Conductance

The final goal is the evaluation of the DC-conductance in the thermodynamic limit. However, the earlier equation (4.15) describes the conductance only in the limit $\omega \rightarrow 0$ for an infinite chain.

$$G = \lim_{\omega \rightarrow 0} \lim_{\eta \rightarrow 0^+} \lim_{M \rightarrow \infty} \frac{q^2}{\omega} [\text{Im}(G_J(\omega + i\eta)) - \text{Im}(G_J(-\omega - i\eta))]. \quad (4.16)$$

As already indicated by the factor $1/\omega$ together with the limit $\omega \rightarrow 0$ the order of the limits is very important. At some point the other limits have to counteract this factor in order to arrive at a finite value for G . Before explaining how to deal with these limits in the actual procedure to calculate G , I want to focus on the shape of the spectrum of the finite systems and what happens if the system size is increased. Since the limit $\eta \rightarrow 0^+$ in connection with the Lorentzians in the correlator $\text{Im}(G_J(\omega + i\eta))$ results in a sum of δ -distributions, $G(\omega)$ is depicted in figure 8 by just using very "slim" Lorentzians of a small finite width η

$$G(\omega, \eta) = \frac{q^2}{\omega} \sum_m |\langle m|J|0\rangle|^2 \left(\frac{\eta}{(E_m - E_0 - \omega)^2 + \eta^2} - \frac{\eta}{(E_m - E_0 + \omega)^2 + \eta^2} \right). \quad (4.17)$$

Because finite systems only ever lead up to discrete spectra an increase in system size M will add more delta-peaks in a symmetric manner around 0. The distributions also appear closer to each other the further the system grows. Although for very high numbers M there are more and more distributions clustered together, they will never lead to a continuous spectrum as expected for an infinite system.

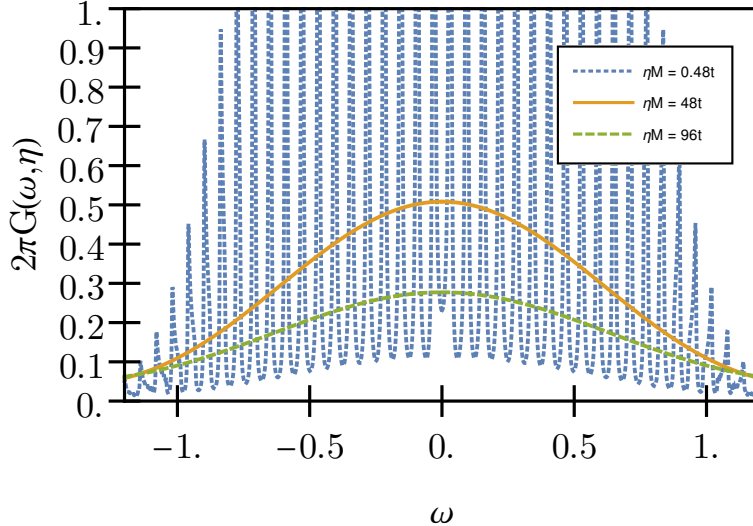


Figure 8: Example spectrum for the broadened frequency dependent conductance for different broadening $C = \eta M$. It is clearly visible how an increased scaling suppresses the discrete nature of the finite spectrum. The examples of $C = 48t, 96t$ show that it is much easier to extract a value for the DC-conductance at $\omega = 0$.

This problem is solved by combining the two limits of η and M , meaning the width of the Lorentzians and the system size into one parameter that can be scaled as

$$\eta = \frac{C}{M}. \quad (4.18)$$

Where C is a constant in units of energy. That means that the frequency dependent conductance changed from a distribution of delta peaks to a distribution of Lorentzians. These get slimmer the longer the setup is, but remember that also more of the Lorentzians appear closer to each other. The key is to choose the broadening well enough, such that for the limit $M \rightarrow \infty$ the conductance of the system converges to the correct value.

Figure 8 shows a finite sample spectrum for a spinless tight-binding chain half filled with fermions for a system length $M = 100$. Three different scaling relations are chosen to point out the direct influence on the spectra. While a very small scaling $C = 0.48t$ still resembles the discrete nature in form of the Lorentzian shapes, the other two examples $C = 48t, 96t$ show an already more smooth appearing shape. As will be seen later in figure 9, the first case is actually unable to reach the correct value of the DC-conductance, because of a too low scaling.

One extreme case would be that the Lorentzians are so slim that the spectrum has very sharp fluctuations that make it impossible to read off values in the infinite limit. In conclusion the scaling has to be chosen carefully, to preserve the actual behavior of the system.

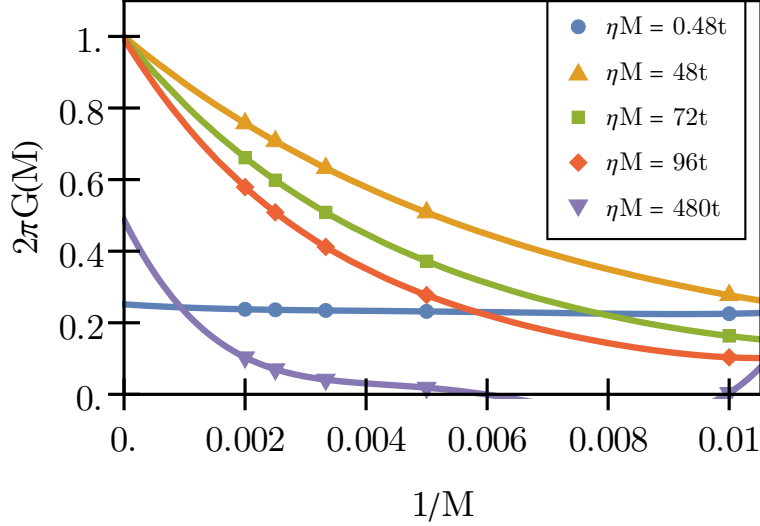


Figure 9: The plot shows the extrapolation of analytically calculated spectra for the noninteracting tight-binding chain at different finite size scaling. This emphasizes how important it is to choose a good scaling. Only the samples of a scaling order of $O(10t)$ converge towards the expected value of $G_0 = 1$. In the other two cases the scaling was either too small or too large to reach convergence in the limited system size.

Another note is, that smoothing the spectra this way, applies only to the investigation of the infinite limit behavior. These spectra do not have any physical meaning for the finite systems. In fact, as seen in Figure 8, the relation (4.18) can be used to tune to several finite DC values ($G(\omega \rightarrow 0.48t/M) \neq G(\omega \rightarrow 0.96t/M)$), just by changing the width, but the limit of the conductance (4.16) will be ultimately unaffected by the tuning and remain the same as can be seen in Figure 9.

The last step on the way to the DC-conductance is to execute the DC-limit, $\omega \rightarrow 0$. The finite size scaling allows to directly read off the DC-values for the finite systems. As pointed out, they are dependent on the scaling and do not represent meaningful quantities, but their limit is in fact the desired DC-conductance in the thermodynamic limit.

In Figure 9 the effect of different scaling parameters C can be observed. As explained in the next chapter the expected value of the conductance would be unity for this specific normalized y-axis. Using the low scaling of $C = 0.48t$ leads to an analytical DC-conductance limit that is differing from the other "well chosen" values of $C = 48t, 72t, 96t$. A much too broader value of $C = 480t$ on the other hand leads to a very slow convergence, that becomes impractical if one is limited to a maximum system size during numeric evaluation.

This completes all the necessary tools for the thesis' method. The final procedure consists of three steps.

1. Specify the Hamiltonian of the system, that is investigated for a specific set

of increasing finite lengths $\{M_i\}$.

2. Use the first three steps of the DDMRG algorithm to calculate the correlator $\text{Im}(G_J(\omega + i\eta))$ and construct the broadened version of the frequency dependent conductance, that is properly scaled,

$$G(\omega, \eta = C/M_i, M_i) = \frac{q^2}{\omega} [\text{Im}(G_J(\omega + i\eta)) - \text{Im}(G_J(-\omega - i\eta))]. \quad (4.19)$$

3. Look for the DC-values of the conductance, $G(M_i) = G(\omega = 0, \eta = C/M_i, M_i)$, and extrapolate them into the thermodynamic limit $G(0, \eta = 0, \infty) = G$.

Of note, although I will call the quantities $G(\omega, \eta = C/M_i, M_i)$ finite frequency dependent conductance and $G(M)$ finite-system conductance throughout the thesis, strictly speaking they are not the equivalent of a conductance for a finite system due to the already mentioned reasons. Only in the limit $M \rightarrow \infty$ that is obtained in step 3. $G(M)$ becomes the physical DC-conductance.

It is also worth to note that in the second step during the construction of the finite frequency dependent conductance the numeric error produced by the DDMRG algorithm is effectively doubled due to the sum. During the calculation of the procedure the quantities are set to $t = q = \hbar = 1$. The extrapolation into the thermodynamic limit is done via polynomial fits and is usually plotted against $1/M$, in order to move the thermodynamic limit ($M \rightarrow \infty$) to the y-axis. The value for the DC-conductance can then be easily obtained by following the fit as guide to the eyes to the intersection with the axis.

5. Verifying the Method

In order to check, if the procedure, that was introduced in the previous chapters, actually works, this chapter starts by providing the analytical results for the DC-conductance of non-interacting spinless fermions in a half filled chain. Once several of the broadened spectra (4.19) are calculated analytically, the new procedure is run for the same system setups. This allows comparison of the numerical and analytical results and to see if they subsequently converge to the same values of G in the thermodynamic limit.

5.1. Tight-Binding Chain - Correlator Calculation

In order to evaluate correlators like in equation (4.17) and (4.19) analytically the setup of interest has to be very simple. This section has the purpose to deliver a well-structured entry for the reader, which is new to this field of physics. The more advanced reader on the other hand might skip this section. This sort of calculation is well known and can be found in [8].

Starting with systems where the fermions are not interacting the Hamiltonian is reduced to the simple tight-binding Hamiltonian

$$H_{\text{TB}} = - \sum_{j=2}^M t(j) (c_j^\dagger c_{j-1} + c_{j-1}^\dagger c_j). \quad (5.1)$$

The single particle wave function $\langle j|k\rangle = \psi_k(j)$ for a particle at position j with momentum k helps to transform the creation and annihilation operators into the momentum picture by

$$a_k^\dagger = \sum_{j=1}^M \langle j|k\rangle c_j^\dagger = \sum_{j=1}^M \psi_k(j) c_j^\dagger, \quad (5.2)$$

$$c_j^\dagger = \sum_k \psi_k^*(j) a_k^\dagger, \quad (5.3)$$

where a_k^\dagger creates and a_k annihilates a fermion of momentum k . Assuming the particle to be forced to the chain, as if a box shaped potential would be present outside the chain, the single particle wave function is given as

$$\psi_k(j) = \sqrt{\frac{2}{M+1}} \sin(kj), \quad k = \frac{\pi n}{M+1} \quad (5.4)$$

$$n \in \{1, \dots, M\}$$

Using this conversion rules and having $t(j) = t$ constant allows to transform the

tight-binding Hamiltonian into the diagonal momentum space representation

$$H_{\text{TB}} = - \sum_k 2t \cos(k) a_k^\dagger a_k. \quad (5.5)$$

During the transformation the identity

$$\frac{2}{M+1} \sum_{j=1}^M \sin(kj) \sin(k'j) = \delta_{kk'} \quad (5.6)$$

was used as in [8]. (5.5) is the well-known result of the cosine shaped energy spectrum of the tight-binding model. There is only a discrete number of possible momentum vectors k , that depends on the total length M of the chain. For the ground state configuration this spectrum is filled up to the energy level of the Fermi vector denoted by k_F .

Just plugging in the expression for the effective current operator (2.6) into the correlator of (4.19) leads to

$$\begin{aligned} \sum_m |\langle m|J|0\rangle|^2 L(\omega, \eta, m) &= \sum_m |\langle m| \sum_{i=2}^M \Delta C(j) J_j |0\rangle|^2 L(\omega, \eta, m) \\ &= \sum_m \left| \sum_{j=2}^M \Delta C(j) \langle m|J_j|0\rangle \right|^2 L(\omega, \eta, m), \end{aligned} \quad (5.7)$$

where $L(\omega, \eta, m)$ represents the Lorentzian distributions. In order to make use of this result the single site current J_j has to be transformed into the momentum picture. Furthermore, it might be of interest if the action of J_j on the ground state $|0\rangle$ can be derived. In the same way as for the Hamiltonian, the transformation rules (5.2) and (5.3) can also be used to express the single site currents J_j as

$$J_j = \sum_{k,k'} a_k^\dagger a_{k'} J_j^{k,k'}, \quad (5.8)$$

where using the single particle wave functions (5.4) directly leads to

$$J_j^{k,k'} = \frac{it}{\hbar} \left[\langle k|j\rangle \langle j-1|k'\rangle - \langle k|j-1\rangle \langle j|k'\rangle \right] \quad (5.9)$$

$$= - \frac{2it}{\hbar(M+1)} \left[\sin(kj) \sin(k'(j-1)) - \sin(k(j-1)) \sin(k'j) \right]. \quad (5.10)$$

The next step on the way to calculate the correlator $|\langle m|J|0\rangle|^2$ is to look at how J_j acts on the ground state $|0\rangle$. The ground state can be formed by filling up the vacuum state $|\text{vac}\rangle$ with fermions of momentum k , until the Fermi level with k_F is

reached

$$|0\rangle = \prod_{k \leq k_F} a_k^\dagger |\text{vac}\rangle. \quad (5.11)$$

The action of the current operator onto the ground state can then be rewritten as

$$\begin{aligned} J_j |0\rangle &= \sum_{kk'} J_j^{k,k'} a_k^\dagger a_{k'} \prod_{q \leq k_F} a_q^\dagger |\text{vac}\rangle \\ &= \sum_{\substack{k' \leq k_F \\ k > k_F}} J_j^{k,k'} |k, k'\rangle, \end{aligned} \quad (5.12)$$

where in the second line the second term only contributes when an electron with momentum $k' < k_F$ is destroyed and a new one with momentum k is created. The notation $|k, k'\rangle$ denotes such a state. Using this knowledge simplifies the correlator and opens up the possibility to evaluate it analytically.

$$\begin{aligned} \sum_m |\langle m | J | 0 \rangle|^2 L(\omega, \eta, m) &= \sum_m |\langle m | \sum_{i=2}^M \Delta C(i) J_i | 0 \rangle|^2 L(\omega, \eta, m) \\ &= \sum_{q,q'} \left| \sum_{i=2}^M \Delta C(i) \langle q, q' | J_i | 0 \rangle \right|^2 L(\omega, \eta, m) \\ &= \sum_{q,q'} \left| \sum_{i=2}^M \Delta C(i) \langle q, q' | \sum_{\substack{k' \leq k_F \\ k > k_F}} J_i^{k,k'} |k, k'\rangle \right|^2 L(\omega, \eta, m) \\ &= \sum_{q,q'} \left| \sum_{i=2}^M \Delta C(i) \sum_{\substack{k' \leq k_F \\ k > k_F}} J_i^{k,k'} \langle q, q' | k, k' \rangle \right|^2 L(\omega, \eta, m) \\ &= \sum_{\substack{k' \leq k_F \\ k > k_F}} \left| \sum_{i=2}^M \Delta C(i) J_i^{k,k'} \right|^2 L(\omega, \eta, m), \end{aligned} \quad (5.13)$$

because the single particle wave function (5.4) can be directly inserted in the defi-

inition of $J_j^{k,k'}$

$$\begin{aligned}
& \sum_{j=2}^M \Delta C(j) J_j^{k,k'} \\
&= - \frac{2it}{\hbar(M+1)(j_2-j_1)} \sum_{j_1+1}^{j_2} \left[\sin(kj) \sin(k'(j-1)) - \sin(k(j-1)) \sin(k'j) \right] \\
& \hspace{20em} (5.14) \\
&= - \frac{2it}{\hbar(M+1)(j_2-j_1)} \left[\sum_{j_1+1}^{j_2} \sin(kj) \sin(k'(j-1)) - \sum_{j_1+1}^{j_2} \sin(k(j-1)) \sin(k'j) \right] \\
&= - \frac{2it}{\hbar(M+1)(j_2-j_1)} \left[\sum_{j_1+1}^{j_2} \sin(kj) \sin(k'(j-1)) - \sum_{j_1}^{j_2-1} \sin(kj) \sin(k'(j+1)) \right] \\
&= - \frac{2it}{\hbar(M+1)(j_2-j_1)} \left[\sum_{j_1+1}^{j_2-1} \sin(kj) \left(\sin(k'(j-1)) - \sin(k'(j+1)) \right) \right. \\
& \quad \left. + \sin(k(j_2)) \sin(k'(j_2-1)) - \sin(kj_1) \sin(k'(j_1+1)) \right] \\
&= \frac{2it}{\hbar(M+1)(j_2-j_1)} \left[2 \sum_{j_1+1}^{j_2-1} \sin(kj) \cos(k'j) \sin(k') \right. \\
& \quad \left. + \sin(k(j_2)) \sin(k'(j_2-1)) - \sin(kj_1) \sin(k'(j_1+1)) \right] \hspace{2em} (5.15)
\end{aligned}$$

Inserting this expression into the conductance (4.19) gives a manageable expression that results in concrete values for $G(\omega, M)$. The computation effort to calculate this expression still grows with M^2 for a constant wire region in the enlargement process, as can be seen in (5.13).

Equation (5.15) was used to study the scaling of the frequency dependent conductance and broadened conductance for the earlier proposed shapes of the perturbation $\Delta C_{\text{Linear}}(i)$ and $\Delta C_{\text{Step}}(i)$ in appendix B.1 The linear case resulted in an expression $G_{\text{Linear}}(\omega, \eta)$ for a finite η

$$G_{\text{Linear}}(\omega, \eta) \approx = \frac{D}{\pi \eta M} \hspace{10em} (5.16)$$

that is scaling with the Drude weight, while the step like potential resulted in an expression

$$G_{\text{Step}}(\omega) \approx \frac{q^2}{h} \left[1 + \cos^2(k_F M_W) \frac{1}{4} \frac{\omega^2}{v_F^2} \right] \hspace{2em} (5.17)$$

that is proportional to the quantum of conductance in the leading order. These two calculations show what was already expected from the two equations (1.6) and

(1.8) of the conductivity in their respective limit. The same calculations were not possible for G_{Mixed} , but in Figure 12 $G_{\text{Mixed}}(M_i) = G(M_i)$ for finite systems of length M_i that are calculated via equation (5.15) are compared with DMRG results. Both the analytical and numeric results approach the quantum of conductance in the thermodynamic limit.

This behavior leads to finally choosing the mixed variant in which the linear drop only occurs in the wire region to ensure the study of the conductance and not the Drude weight.

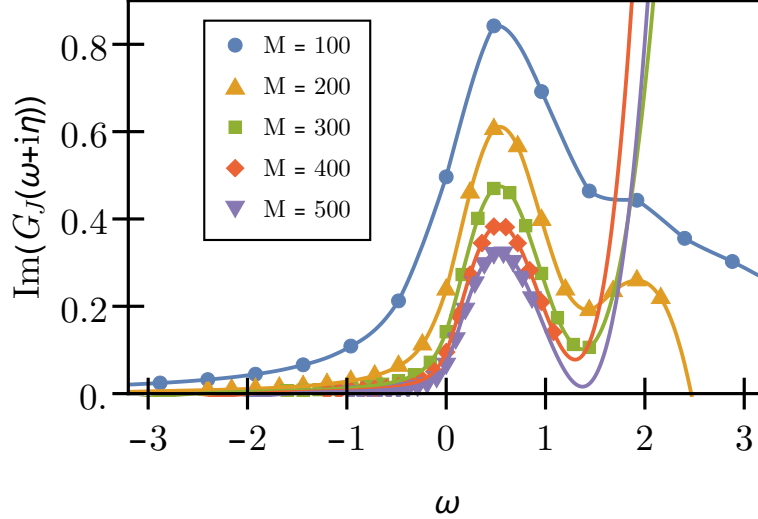


Figure 10: DDMRG output $\text{Im}(G(\omega + i\eta))$ against frequency. The results for different system sizes M and frequencies ω are shown as symbols that are explained in the inset. The DMRG results are then interpolated as seen in the figure. The most notable part is that in the interval around $\omega = 0$ this interpolation is smooth. This is necessary to calculate the finite frequency dependent DC-conductance depicted in Figure 11.

5.2. Tight-Binding Chain - Numerical Results vs. Analytical Expectation

The previous chapter presented the necessary tools to calculate the DC-conductance for the tight-binding model in a very analogous but analytical way to the DMRG procedure. In order to verify the results of the numeric method, the outlined steps of the procedure are run twice. For the first run only the analytical expressions are used to obtain $\text{Im}(G(\omega + i\eta))$. This value for the imaginary part is then used to evaluate the frequency dependent conductance (4.19) and to finally extrapolate the DC-values into the thermodynamic limit, such that a precise value for G is yielded.

In the second run numeric results of the DMRG algorithm of the correlators are used in the same way as described in 4.1, such that they replace the analytically calculated correlators. This way both the numeric and analytical spectra before and after the extrapolation can be compared step by step. In Fig. 9 the extrapolation of the analytical DC-conductance for different scaling parameters of the tight-binding-chain could already be observed. The analytical result therefore predicts a value of $G = 1/(2\pi)$. This matches the value of the so called quantum of conductance

$$G_0 = \frac{q^2}{h} = \frac{1}{2\pi}, \quad (5.18)$$

because $t = q = \hbar = 1$. This is the reason why the plots are scaled in units of $2\pi G = G/G_0$.

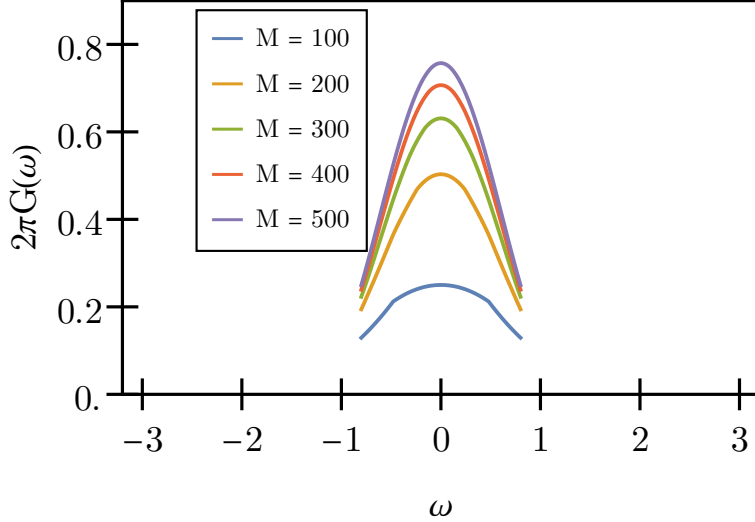


Figure 11: Finite frequency dependent conductance calculated from the in Figure 10 depicted $\text{Im}(G(\omega + i\eta))$ according to equation (4.15). Since the main interest lies within the DC-behavior only a small region around $\omega = 0$ is necessary, in order to extract the scaled DC-conductance for a finite system of size M .

In the second run the process relies purely on the output of the DDMRG algorithm for the imaginary parts $\text{Im}(G(\omega + i\eta))$ for different system size M . A sample of these can be observed in Fig. 10. The shown spectra are for a constant wire region of $M_W = 10$ sites. Because I am only interested in the finite DC-values, after forming $G(\omega = 0, \eta = C/M_i, M_i)$ out of $\text{Im}(G(\omega + i\eta))$, only a small frequency range around $\omega = 0$ has to be taken into account and calculated. The $G(\omega = 0, \eta = C/M_i, M_i)$ that are the direct result of the $\text{Im}(G(\omega + i\eta))$ in Fig. 10 are depicted in Fig. 11. Here again, only a small frequency range around $\omega = 0$ is needed for the extrapolation into the thermodynamic limit. The final extrapolation for both cases is depicted in Fig. 12. The limit of the analytical and numeric routes are both matching the quantum of conductance. The analytical solution was derived using equation (5.13) with equation (5.15).

Additionally the extrapolation for other wire lengths $M_W = 34, 58, 82$ are also included and the conductance is plotted against M_W/M . From the result it can be concluded that a large ratio of M/M_W is desired, to ensure a fast convergence. Therefore, the method works as intended and a small wire section is sufficient to observe the DC-conductance in the thermodynamic limit. Thus, in all following plots only systems of a wire lengths of $M_W = 10$ sites are shown.

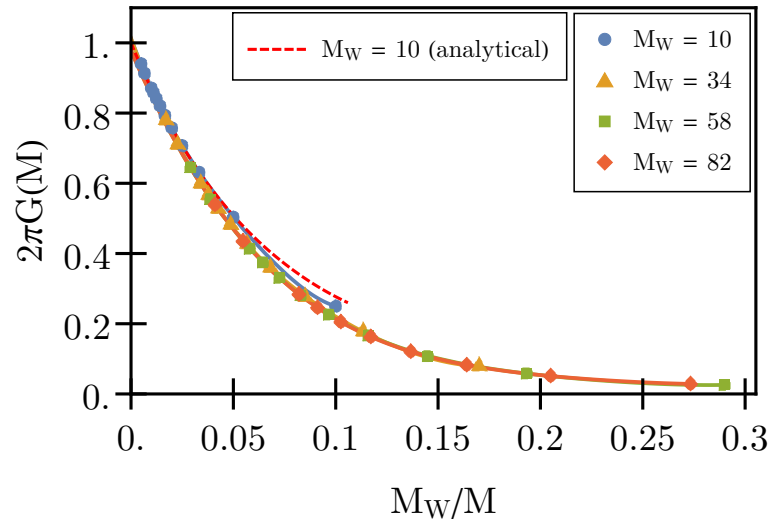


Figure 12: The figure shows the extrapolation of the broadened DC-conductance of the finite systems into the thermodynamic limit. The studied systems differ in wire length M_W . The x-axis is scaled by M_W/M , which shows that for all systems the limit does not change and small wires with large system sizes converge faster. The figure is adapted from Ref. [33].

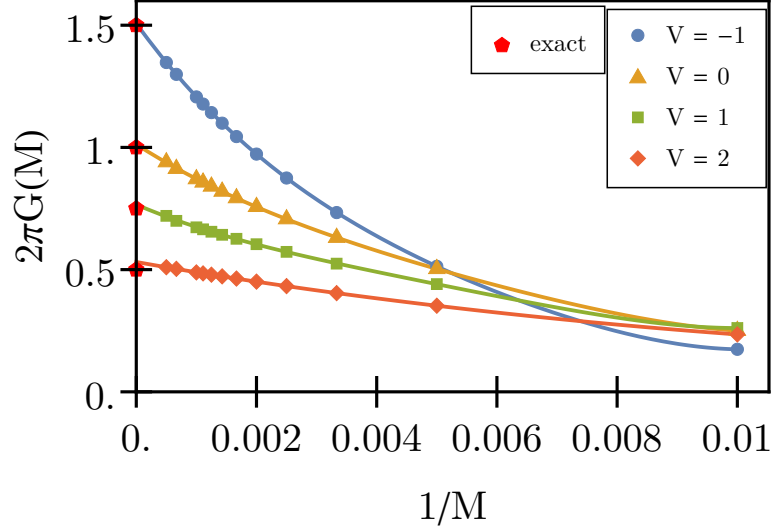


Figure 13: DMRG results for the conductance of a homogeneous interacting chain for different interaction parameters V . $G(M)$ is plotted against an inverse system size $1/M$. At $1/M = 0$ the exact values according to a Luttinger liquid (6.2) and the Bethe ansatz solution (6.3) is depicted as red pentagons. For all cases the wire has $M_W = 10$ sites. The figure was published in Ref. [33].

6. Luttinger Liquids and Fermionic Interaction

In this section the procedure is expanded to interacting systems, where theory predicts the behavior of a Luttinger liquid. In this kind of systems fermions behave as the name implies like a liquid and can be described by a few parameters. The first part starts by investigating only homogeneous interacting chains of different interaction strength V and its effect on the DC-conductance in the thermodynamic limit. Then, in the second part in addition to the interaction a potential barrier [1, 34–36] in form of an on site potential in the middle of the wire section is added. The potential strength can be varied. And then in the last part going even further a second barrier is added where the parameters of the potential can be adjusted individually. All the results of this chapter were published in [33].

6.1. Homogeneous Interaction

The setup is a one-dimensional chain half filled with spinless fermions and effectively the same as the tight-binding setup from before with an added homogeneous interaction term. The Hamiltonian to describe the unperturbed base system is then

$$H_{\text{HI}} = H_{\text{Kin}} + H_{\text{C1}} = -t \sum_{j=2}^M \left(c_j^\dagger c_{j-1} + c_{j-1}^\dagger c_j \right) + V \sum_{j=2}^M \left(n_j - \frac{1}{2} \right) \left(n_{j-1} - \frac{1}{2} \right). \quad (6.1)$$

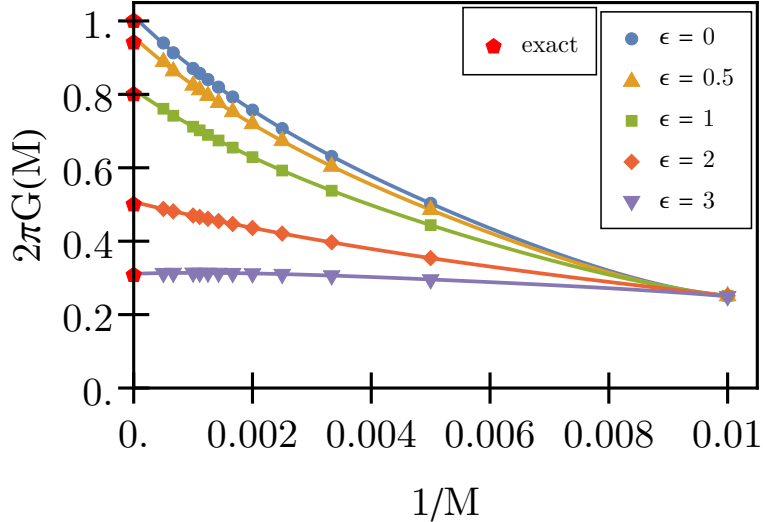


Figure 14: Conductance $G(M)$ for non-interacting chain with impurity of strength ϵ in the middle of the wire section against $1/M$. Red pentagons at the vertical axis indicate the exact values from the Landauer formula (6.5). For all cases the wire is of $M_W = 10$ sites. The figure was published in Ref [33].

The model can be solved using the Bethe ansatz solution for the one-dimensional spin- $\frac{1}{2}$ Heisenberg model [37]. For an interaction parameter V that is restricted to the interval $(-2t, 2t]$, for $t > 0$, a gapless excitation spectrum is expected in the thermodynamic limit. Because here, the fermions are assumed to be spinless, this means that only one type of charge carrier is present. The DC-conductance for a one channel Luttinger liquid G_{LL} [34] is given by

$$G_{LL} = KG_0. \quad (6.2)$$

Here, K is the Luttinger Liquid parameter [34–36]. The parameter can be obtained by the Bethe ansatz solution for the spin- $\frac{1}{2}$ Heisenberg chain, that connects the parameter and the interaction by

$$K = \frac{\pi}{2} \frac{1}{\pi - \arccos\left(\frac{V}{2t}\right)}. \quad (6.3)$$

This enables us to directly compare the predicted DC-conductance G_{LL} with the numeric results of the procedure.

The outcome of the method is displayed in Figure 13. The exact values for the Bethe ansatz solution are marked on the y-axis for different values of the interaction V . The polynomial fits match the theoretical predictions well. An outlier is the extrapolation for the case of $V = 2$, where it overshoots the expected value. This may be due to additional finite size effects that are not taken into account for by the scaling $\eta = C/M$. Nevertheless, in the broader picture this shows that the method

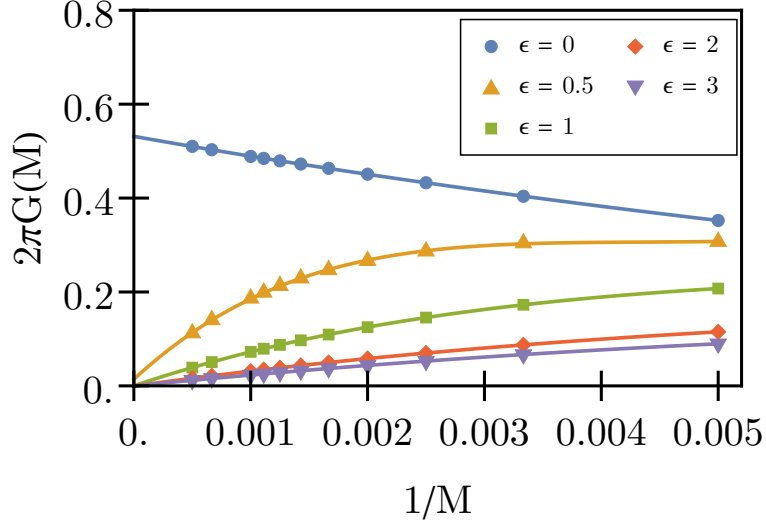


Figure 15: Conductance $G(M)$ for a homogeneous chain with repulsive interaction $V = 2t$ in addition to a single on site barrier in the middle of the wire region of strength ϵ . For all cases the wire has $M_W = 10$ sites. The figure was published in Ref. [33]

is a viable tool for the dynamical quantities of interacting one-dimensional systems.

6.2. Homogeneous Interaction - Single Barrier

The previous system is expanded on by adding a potential barrier modelled as a chemical potential of strength ϵ at a specific site j_a . The site is roughly located in the middle of the wire region. The setups are usually chosen with even number M of total sites, such that there is no middle site. So the potential is applied to one of the closest two sites ($j_a \approx \frac{j_1+j_2}{2}$). The single barrier Hamiltonian then consists of the same parts as the homogeneous interaction Hamiltonian with the addition of the chemical potential

$$H_{\text{SB}} = H_{\text{HI}} + \epsilon n_{j_a} \quad (6.4)$$

For starters it is best to look at the results for the case of the non-interacting chain $V = 0$ with a potential barrier. This specific case can be compared to the Landauer theory of elastic scattering at a barrier [11] and with the results of Kane and Fisher in Ref. [36]. The conductance is controlled by the transmission T through

$$G_L = G_0 T. \quad (6.5)$$

The idea is that an incoming wave is partially transmitted and reflected at the barrier, which is represented in the amplitude of the respective waves. The resulting set of equations can then easily be solved for the transmission coefficient T (see

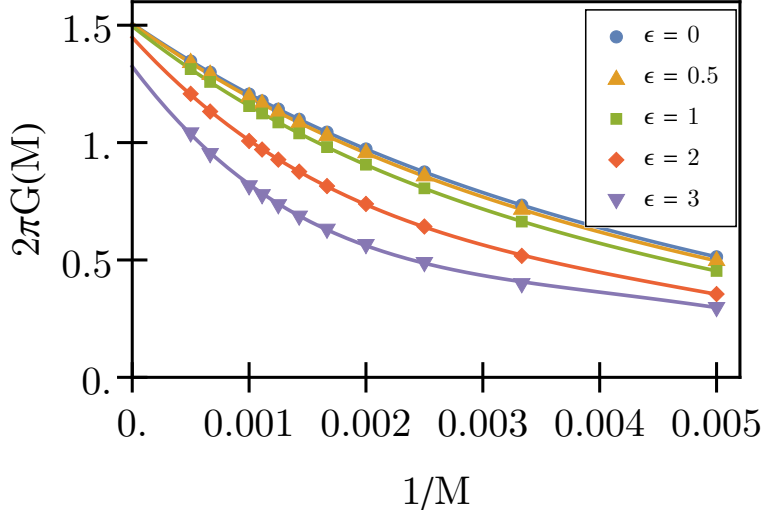


Figure 16: DMRG results for the case of a homogeneous interacting chain with attractive interaction $V = -t$ and on-site barrier of strength ϵ . The wire is of $M_W = 10$ sites and the scaling is chosen as $\eta = 48t/M$. The plot was adapted and slightly modified from Ref. [33]

appendix C.1), which yields

$$T = \frac{4t^2 \sin^2(k_F)}{4t^2 \sin^2(k_F) + \epsilon^2}. \quad (6.6)$$

k_F is the Fermi wave number and is here $\pi/2$ for the simple tight-binding model. From this formula one can directly see that it should not matter if the potential is of attractive or repulsive nature, because the potential strength ϵ only occurs squared. Also the DC conductance should decrease with increasing potential strength $|\epsilon|$.

The procedures output depicted in Fig. 14 matches the values predicted by equation 6.5 surprisingly well. The polynomial extrapolations converge in the thermodynamic limit to the values of the Landauer theory.

However, these results dramatically change, once the interaction is turned on. Fig. 15 and Fig. 16 show the results for $V = 2t$ and $V = -t$. These findings clearly point out how different the conductance is for a Luttinger liquid compared to a non-interacting chain in case of barrier scattering. For the repulsive interaction one can observe a complete breakdown in transport, once the potential slightly differs from $\epsilon = 0$. The result is a universal insulator.

For attractive interaction on the other hand the strength of the impurity does not affect the conductance at all. As Figure 16 depicts this setup stays conducting regardless the strength of the impurity. This behavior is completely different to the results for the homogeneous noninteracting chain where the barrier controls the conductance. Of note, the polynomial extrapolation in Fig. 16 does not exactly match the predicted value for stronger barriers, because a much higher ratio of

M_W/M is needed to make the fits more accurate.

This shows that the results are in strong agreement with the literature [36] and outline the viability of the method in case of a single barrier that is located in the wire section.

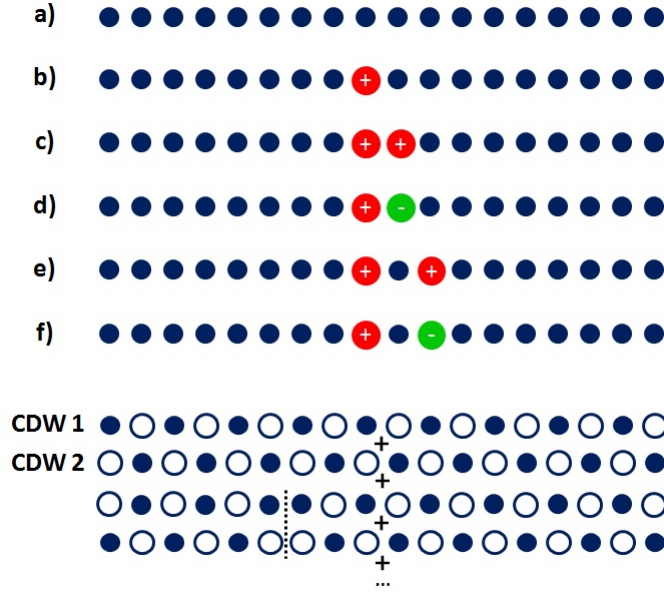


Figure 17: Schematic depiction of several homogeneous interacting setups with different kind of impurities in the middle of the chain. All studied examples of a combination of attractive (green(-)) and repulsive (red(+)) impurities are shown in a)-f). The schematics in the bottom indicate the charge density wave like structure of the ground state that has additional contributions composed of the domains of these charge density waves. In these the periodicity is broken at the so called domain walls (dashed line).

6.3. Homogeneous Interaction - Double barrier

Adding a second barrier to the wire section opens up a variety of different problems to investigate. There are several combinations of how one can place two barriers next to each other. But one has to take into account that the wire is only of $M_W = 10$ sites in contrast to the very large growing lead sections. This means that where exactly these two barriers are placed, when their relative constellation is kept the same, should not make a significant difference. Another characteristic to consider is, whether the impurities are modelled both attractive or repulsive, or one mixes up an attractive and repulsive barrier in one setup.

Regardless of which setup exactly is chosen the Hamiltonian will also follow the previous structure of a single barrier by just adding another on site potential of strength ϵ_b at site j_b to the first impurity ϵ_a at site j_a . The double barrier Hamiltonian therefore is

$$H_{DB} = H_{HI} + \epsilon_a n_{j_a} + \epsilon_b n_{j_b}. \quad (6.7)$$

From a theoretical perspective the behavior of this kind of systems is more complicated to describe than that of a the single barrier.

For the behavior of a single impurity Kane and Fisher proposed a solution for the

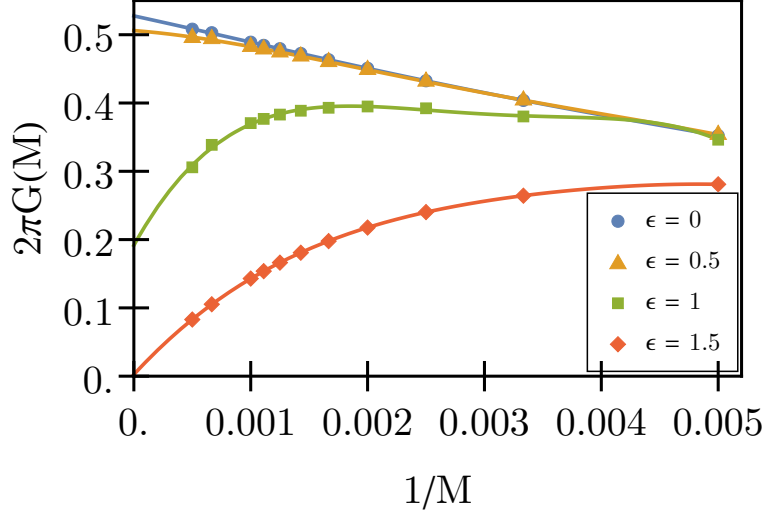


Figure 18: Conductance $G(M)$ for repulsive homogeneous chain with $V = 2t$ and two non-resonant barriers (case c)) of strength ϵ in the middle of the chain. For all cases the wire has $M_W = 10$ sites. The figure was published in Ref. [33]

repulsive Luttinger Liquid ($V > 0, K < 1$) in Ref. [36]. In this system fermions tend to follow a structure that is called a charge density wave (CDW) with additional contributions. This CDW without these contributions is the insulating ground state for nearest neighbor interactions $V > 2t$ outside the Luttinger liquid regime. For a half filled chain of spinless fermions it follows a pattern of periodicity 2 with two possibilities for the ground state as depicted in the bottom of the schematics in Fig. 17 as CDW 1 and CDW 2. As mentioned this structure itself would be insulating, but the additional contributions that are also depicted allow for particles to move through the setup and therefore a current. The contributions are composed of the "domains" of the two CDW's, such that the point in the setup where they meet is called a domain wall (indicated by a dashed line in the schematics).

If one were to add an impurity to such a setup it would directly affect one of the two CDW domains. The system then is pinned down to either CDW solution of the respective domain which in turn makes a current less likely or completely inhibits it. It can be argued that placing an attractive potential into one of the occupied CDW sites (see fig. 17 a)) makes this exact CDW domain preferable to the other one and thus a current is also unlikely. A repulsive barrier (fig. 17 b)) on the other hand results in a similar outcome, by dampening the CDW contributions depending on the site placement and preferring the non disturbed CDW domain. This also suppresses fluctuations. The result can be seen in figure 15, where a single barrier lead to an insulating setup.

The question is now what happens, when a second barrier is added. An interesting idea is to use a second barrier to undo the effect of the first one. This could be

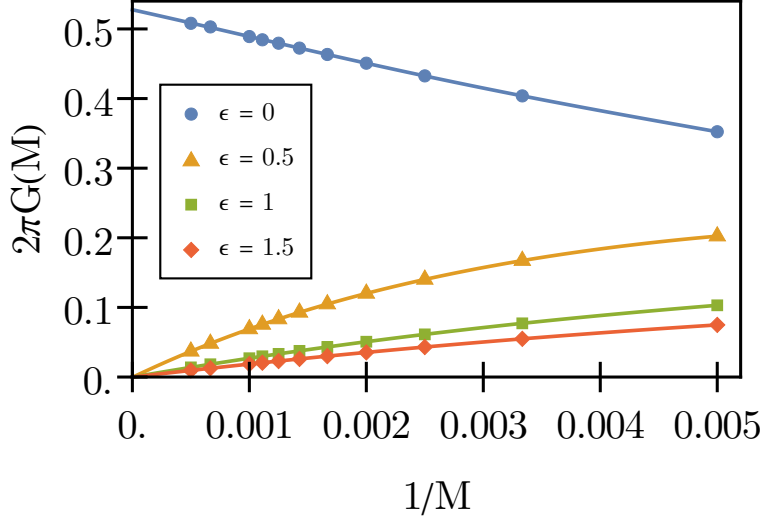


Figure 19: Conductance $G(M)$ for two impurities of opposite signs in their strength ϵ that are placed next to each other (case d)). The present setup is a chain of homogeneous interaction $V = 2t$. For all cases the wire has $M_W = 10$ sites.

accomplished in two ways. The first approach comprises of adding an impurity of the opposite sign to the same CDW domain the first barrier is already influencing. Thus, for example a repulsive barrier that rejects one of the CDW domains can be counteracted by an attractive impurity with a gap of one site to the first, such that it prefers the same CDW domain and therefore undoes the rejection (Fig. 17 f)). The second approach adds a barrier with the same sign as direct neighbor to the first impurity, in order to affect the other CDW domain in the same way as the first as depicted in Fig. 17 c). Remember this thought experiment is of qualitative nature, which means that one might not be able to completely undo, but still limit the effects of the first impurity. These effects are schematically explained in figure 17 by pointing out the expected effect of the impurity to the CDW domain it is placed in.

In summary, the method was tested on the four distinct cases c), d), e) and f). The strength of the pairs of impurities was always set as $|\epsilon_a| = |\epsilon_b| = \epsilon$. The first result can be observed in figure 18. Here the two barriers are of the same sign and adjacent to each other. After scheme 17 both barriers should suppress the two CDW configurations at the same time by the same amount depending on the impurity strength ϵ . This matches the resulting extrapolations quite well, because a low strength like $\epsilon = 0.5$ only slightly diminishes the DC conductance, while greater values ($\epsilon = 1.5$) for the two barriers can produce an insulator. So the conductance is gradually tuned down for barriers that are growing in strength. The next two cases represented in scheme 17 d) and e) are both cases, where the second barrier should enhance the effect of the first one. This is clearly reflected in the results in

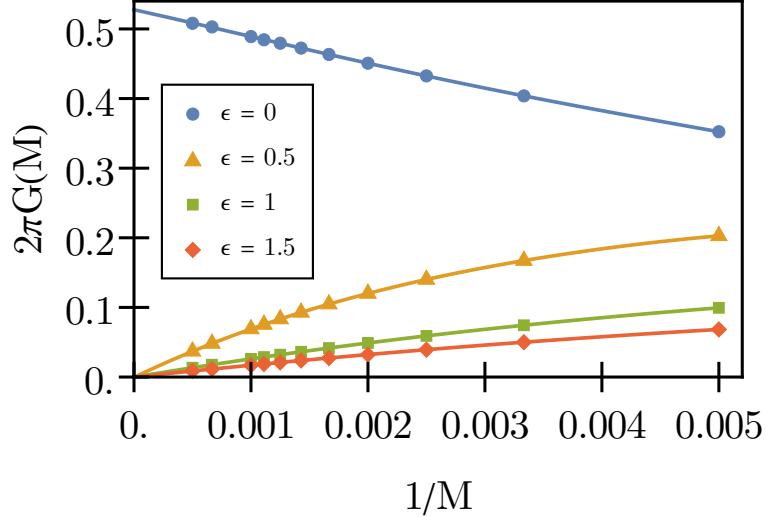


Figure 20: Conductance $G(M)$ for the case of two repulsive barriers that are next-nearest neighbors (case e)). The present setup is a chain of homogeneous interaction $V = 2t$. For all cases the wire has $M_W = 10$ sites.

Fig. 19 and Fig. 20. Both show a universal insulator for all impurity strengths that were chosen and are actually matching so well that it is impossible to distinguish the two plots with the eyes. It is quite astonishing that not only the extrapolated limit, but the results for the finite systems do not differ.

For the last and most surprising case I followed scheme 17 f) - the barrier was placed as next nearest neighbor to the first with opposite sign in strength: $\epsilon_a = \epsilon = -\epsilon_b$. The attractive potential at $j_b = j_a + 2$ enhances the formation of the CDW in the same way as the repulsive barrier at j_a disrupts it. The result in Fig. 21 shows therefore an unchanging conductance compared to the homogeneous chain. The strength of the two barriers seems to have no influence at all on the DC conductance. This behavior matches the predictions by field theoretical models [36] for a resonant double barrier, that enables resonant transmission, where on the other hand a single one of these impurities leads to total reflection.

Although the CDW picture is able to provide a qualitative explanation for the observed results one should still compare to the predictions of Landauer theory for double barrier scattering. Therefore, I calculated in appendix C.2 several different example transmissions for multiple barriers in the same way as is elaborated in Ref. [38]. Landauer theory that is neglecting the Luttinger liquid behavior results in a qualitatively stronger reduction in conductance for case d) than c) depending on the strength of the impurity. This is also observable here. Also the cases d) and e) should not scale the same regarding barrier strength. Here, we see the opposite behavior of the same scaling. In fact, case d) and e) are indistinguishable which rejects that explanation. The last case f) provides a better fit with Landauer theory as the transmission is unaffected by the impurities.

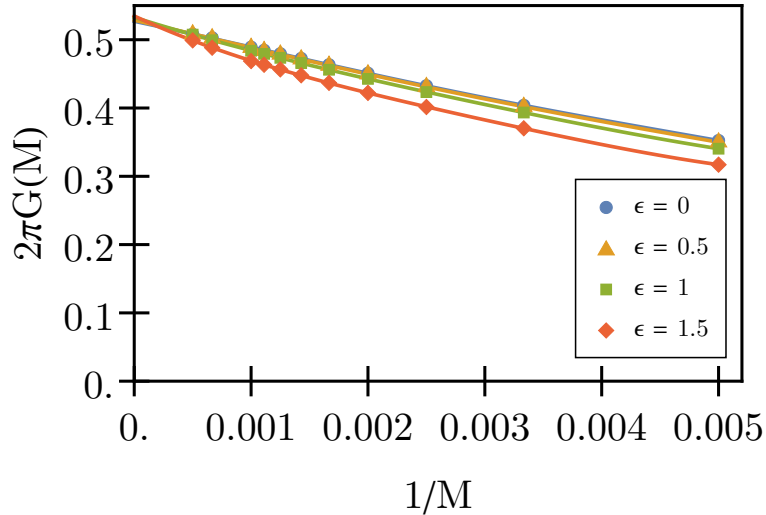


Figure 21: Conductance $G(M)$ for the case of homogeneous interaction $V = 2t$ and two next-nearest neighbor barriers of a strength ϵ of opposite sign(case f)). For all cases the wire has $M_W = 10$ sites. The figure was published in Ref. [33]

This concludes the experimentation scenarios using different barriers in interacting one-dimensional chains. The method of finite scaling in connection with DDMRG delivered some interesting results which are still not fully understood and remain a topic of debate. Nevertheless, the procedure is able to produce results that are in line with other methods and support their qualitative explanations.

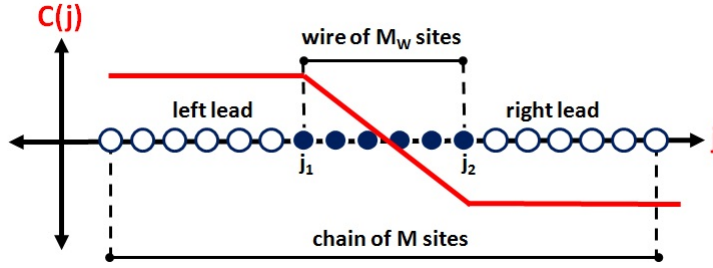


Figure 22: Schematic depiction of a wire-lead setup that has different interactions between the sites belonging to the wire section of M_W sites and the outer lead sections. The shape of the applied perturbation is depicted as $C(j)$. The figure was published in Ref. [39]

7. Inhomogeneous Interaction

The Hamiltonian 6.1 of the unperturbed system does not differentiate between wire and lead sections inside the chain. So far the hopping and interaction was homogeneous for the entire setup. In reality setups that follow the structure presented in section 1 may use different materials for the wire and leads. This distinction only ever was accounted for by the shape of the perturbation as it was discussed in chapter 2. In this section the model is extended to a chain, which differs in wire and lead interaction. The results of this section were published in Ref. [39]. The new base Hamiltonian for inhomogeneous interaction becomes

$$\begin{aligned}
 H_{\text{II}} = & -t \sum_{j=2}^M \left(c_j^\dagger c_{j-1} + c_{j-1}^\dagger c_j \right) + V_W \sum_{j=j_1+1}^{j_2} \left(n_j - \frac{1}{2} \right) \left(n_{j-1} - \frac{1}{2} \right) \\
 & + V_L \sum_{j=2}^{j_1} \left(n_j - \frac{1}{2} \right) \left(n_{j-1} - \frac{1}{2} \right) + V_L \sum_{j=j_2+1}^M \left(n_j - \frac{1}{2} \right) \left(n_{j-1} - \frac{1}{2} \right). \quad (7.1)
 \end{aligned}$$

Here, V_L describes the interaction in the leads and V_W denotes for the wire sections. All the other parameters are kept the same, meaning the system is still half filled with spinless fermions. Since the perturbation is also not changed, the current operator is still the same 2.19. Theory predicts in the form of a field-theoretical approach [40, 41] that the lead interaction determines the conductance of the whole setup. This means that for the still viable relation $G = KG_0$ the factor K is the Luttinger liquid parameter of the leads. The field theoretical approach is based on the assumption that there is a perfect transition from the leads into the wire. Therefore, the possibility of single particle backscattering events at a sharp transition zone is completely neglected. Interested in which of these predictions holds true three different setups with attractive, repulsive and no lead interaction were studied. In all cases the wire interaction was varied. In order to conduct a transport measurement of a nanostructure one of the most common ways is to attach metallic leads to the

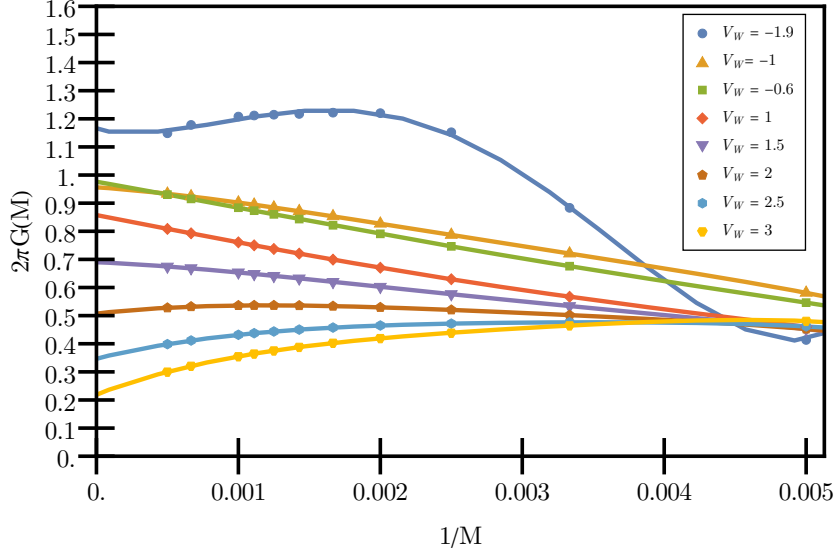


Figure 23: Polynomial extrapolations of the finite-system conductance $G(M)$ against inverse system length $1/M$ for the case of metallic leads $V_L = 0$ and different wire interactions V_W . The wire is of $M_W = 10$ sites. The figure was published in Ref. [39].

structure and expose them to a source and drain voltage. Electrons in metals are usually treated as Fermi liquids, which justifies to treat them as noninteracting [32, 42–49]. Therefore, the first case to study is that of noninteracting leads attached to an interacting wire.

The result for metallic leads with differing wire interaction can be observed in Figure 23. Several conclusions can already be drawn from the extrapolation starting with the division of the results into attracting and repulsive wire interactions.

For attractive interaction the conductance matches the expected conductance of a Luttinger liquid of a homogeneous chain for $V = 0$ at $G = G_0$. This supports the prediction of field theory for a smooth transition from the leads into the wire. The results for the wire interaction close to the border of the Luttinger liquid phase at $V_W = -1.9t$ cannot be extrapolated by a simple polynomial as applicable to the other results. Again I want to note that the polynomial fits should just be treated as guide to the eyes.

For repulsive interaction in the wire the picture looks completely different. The extrapolated conductance clearly decreases according to the strength of the wire interaction or in other words: The sharper the transitions from the noninteracting leads to the wire region becomes, the stronger the effect on the diminishing conductance. This behavior caused by single particle backscattering looks similar to what was observed before for the case of a homogeneous noninteracting chain with an impurity that was located in the middle of the wire in Fig. 14. Here, although heavily diminished this still holds true for values up to $V_W = 3t$ which would already be too high for the Luttinger liquid description of a homogeneous chain. For

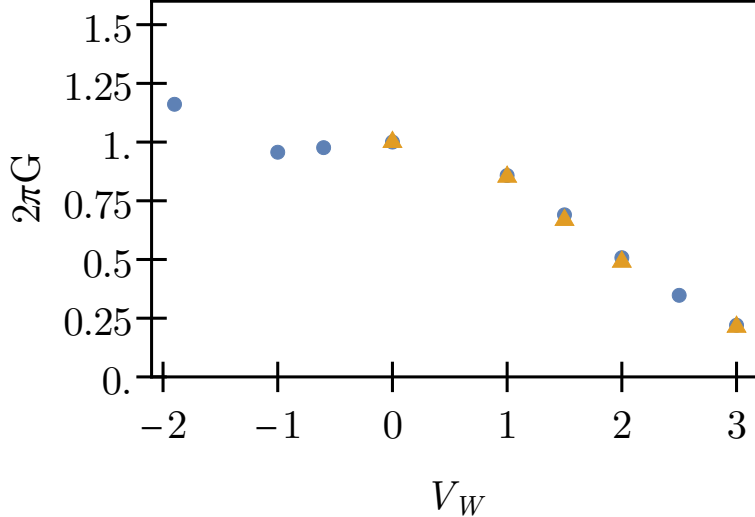


Figure 24: Conductance in the thermodynamic limit for metallic leads $V_L = 0$ and a short interacting wire $M_W = 10$ is plotted against wire interaction V_W . The circles are the extrapolated values of the DMRG data points in figure 23, while the triangles are DMRG data points taken from Ref. [42] for comparison. The figure was published in Ref. [39].

a homogeneous chain of $V = 3t$ the Luttinger phase is already left in favor of an insulating charge density wave state. Therefore, it is expected that for the limit $M_W \rightarrow \infty$ in this specific case the setup becomes also insulating.

There was a similar study (see Ref. [42]) conducted by V. Meden and U. Schollwöck for a setup with a slightly longer wire section of $M_W = 12$ sites. In figure 24 a direct comparison of their data and the results of the present DMRG method is illustrated. The data points are matching quite well and show a similar behavior of the setup for the different repulsive wire interactions.

The next logical step is to investigate the linear conductance of setups that also have interacting leads. I looked into a case of repulsive interaction of $V_L = 2t$ and of attractive interaction $V_L = -t$. The results and their extrapolation are depicted in Figure 25 and in Figure 26. In contrast to the previous case of non-interacting leads less research has been conducted so far.

In the case of $V_L = 2t$ illustrated in Fig. 25 the Luttinger liquid parameter for the homogeneous setup (compare with Fig.14) is determined by the Bethe ansatz solution (6.3) to be $K_L = 1/2$ which corresponds to a conductance of $G = (1/2)G_0$. Extrapolation of the data for a wire interaction V_W close to the value of the leads clearly converges against the Luttinger liquid value of the conductance. For the values $V_W = 0$ and $V_W = -t$, that are further away from the lead interaction backscattering is already occurring in form of a reduced conductance.

For attractive lead interaction $V_L = -t$ illustrated in Fig 26 the field theoretical approach for the smooth transition is also confirmed. When the value of V_W is close

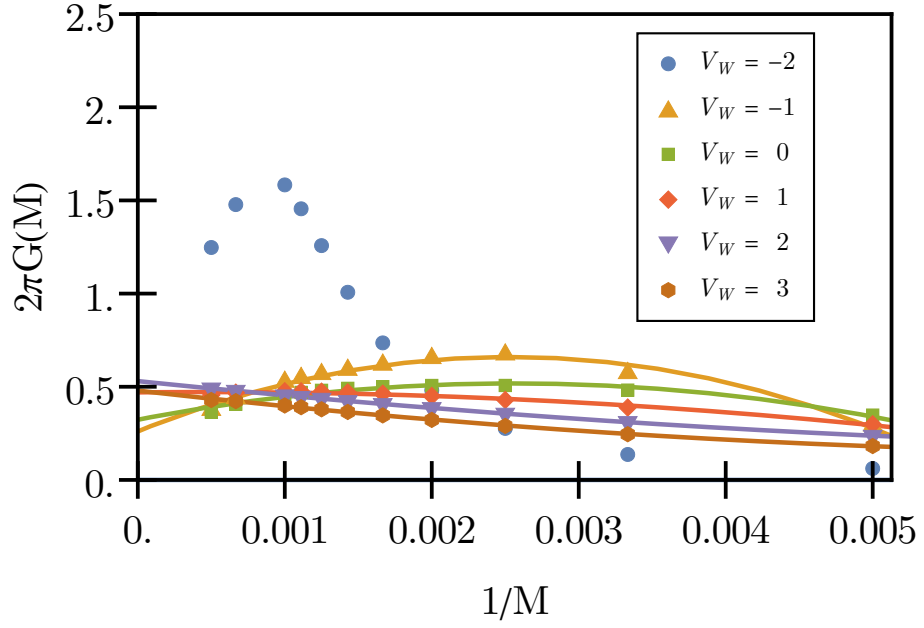


Figure 25: The same setup as figure 23 but with repulsive interaction in the leads $V_L = 2t$. The figure was published in Ref. [39].

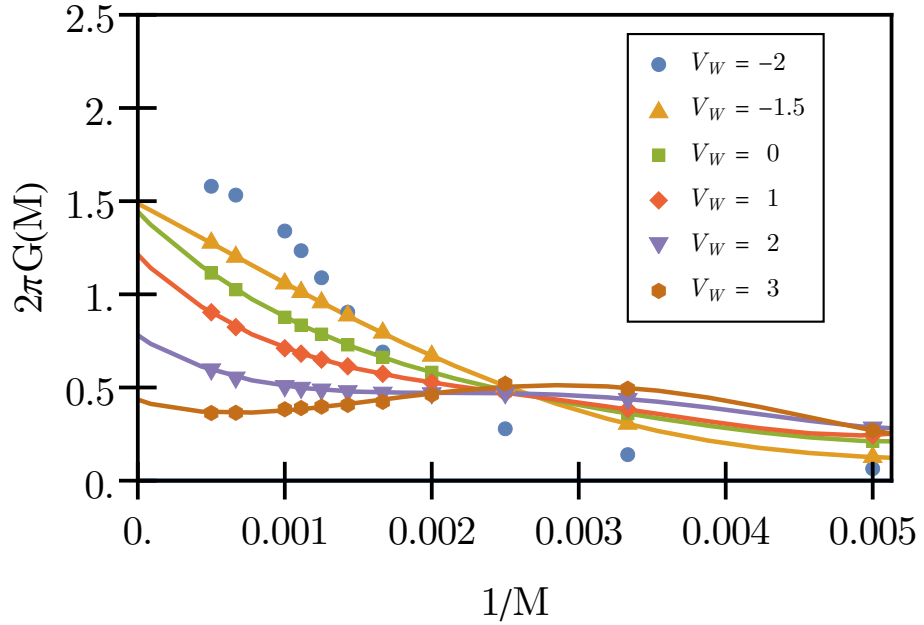


Figure 26: The same setup as figure 23 but with attractive interaction in the leads $V_L = -t$. The figure was published in Ref. [39].

to the lead interaction $V_L = -t$ as it is for example for the two cases $V_W = -1.5t, 0$ the leads dominate the behavior of the conductance. But as soon as the wire interaction deviates too much the single particle backscattering kicks in and diminishes the conductance.

In both interacting cases the wire interaction of $V_W = 3t$ shows a decreased but still finite conductance in the thermodynamic limit. However, the Luttinger liquid regime would already have been left for the homogeneous setup of this interaction. As for the case of noninteracting leads an insulator phase is expected for the limit $M_W \rightarrow \infty$.

In all three cases the extrapolation of the data close to the border of the Luttinger liquid phase at $V_W = -2t$ cannot be performed accurately. This could change if longer setups were studied, but due to computational limitations the maximum chain length was capped at $M = 2000$ sites.

In conclusion, the field theoretical predictions hold for a smooth transition from the leads into the wire region in all studied cases. When the difference between wire and lead interaction becomes too great the behavior deviates from field theory and shows signs of backscattering due to sharp transitions. Overall, the method presented in this thesis proved again to be a viable tool for this kind of problems.

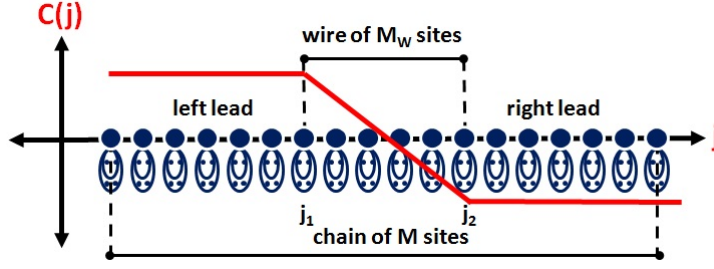


Figure 27: Schematics for the homogeneous noninteracting Holstein chain. On each site there are now two pseudo sites that can hold up to three phonons. The perturbation shape is described by $C(j)$.

8. Boson Interaction - Holstein Chain

It is realistic to assume an experimental setup for a transport measurement like shown in Fig. 1 to be subject to vibrations, that affect the transport of the quantum wire. This becomes especially relevant for systems of atomic dimensions that are connected to lead structures [16–19].

Therefore, I focus on a setup that integrates electron-boson interaction into the chain also known as the Holstein chain. The results were published in [39]. The vibrations can be described in the form of quasi particle bosons, called phonons. For a noninteracting chain the general Holstein Hamiltonian reads

$$\begin{aligned}
 H_{\text{Holstein}} &= H_{\text{Kin}} + H_{\text{Phonon}} \\
 &= -t \sum_{j=2}^M \left(c_j^\dagger c_{j-1} + c_{j-1}^\dagger c_j \right) + \omega_b \sum_{j=1}^M b_j^\dagger b_j - g \omega_b \sum_{j=1}^M \left(b_j^\dagger + b_j \right) n_j. \quad (8.1)
 \end{aligned}$$

Here, in addition to the familiar kinetic part of the tight-binding Hamiltonian for fermions there are now terms containing the boson creation and annihilation operators b^\dagger and b . The second term describes the collective energies of the phonons of frequency ω_b , while the last term indicates the interaction between the spinless fermions and bosons via the coupling g . An electron at site j thus creates or destroys a phonon of frequency ω_b according to the magnitude of the electron-phonon coupling g .

Since, in comparison to the setups in previous chapters, the fermion interaction is dropped the distinction between wire and lead sections is only found in the shape of the applied potential as explained in section 2. The chain is half filled with spinless fermions as it was the case in the previous setups. The major problem regarding phonons that now have to be added to each fermion site is that due to their bosonic nature in principle an unlimited amount of phonons can occupy a single site. This would require an infinite dimensional Hilbert space to represent the setup and make the DMRG method not viable. Therefore, a cutoff for a maximum

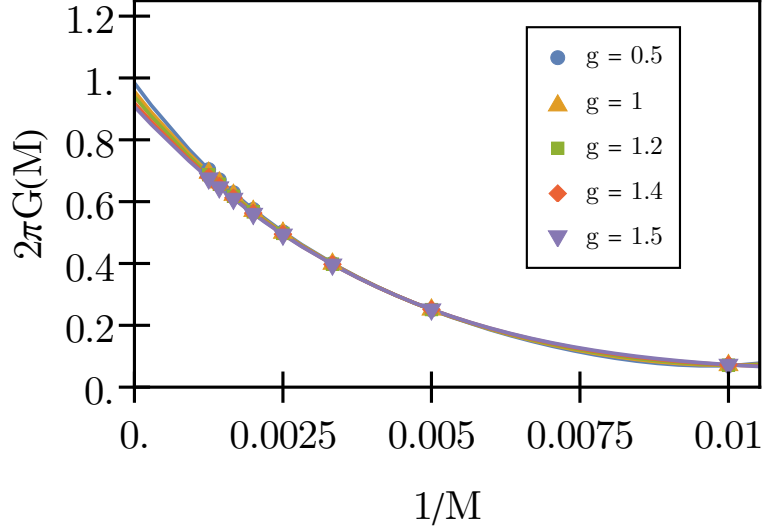


Figure 28: DMRG conductance $G(M)$ for the spinless fermion Hoslstein model in the adiabatic regime $\omega_b = 0.1t$ against inverse system length $1/M$ for different electron-phonon couplings g . The figure was published in Ref. [39].

number of phonons per site N_b has to be chosen to ensure a finite setup.

Another factor to take into account is in which form the boson sites are attached to the fermion sites. Simply adding an additional site per fermion site that is reserved for the bosons might lead to an extreme computational effort despite a seemingly small phonon cut off. In fact, the computational demand scales with N_b^3 as described in Ref. [50].

Let us assume for example that one decides to allow at maximum $N_b = 7$ phonons per fermion site, such that a local Hilbert space of eight dimensions is added to a fermion site. Part of the DMRG algorithm is to take a subsystem of the full lattice and to enlarge it by one site. After the enlargement one has to truncate the now bigger subsystem space to a predetermined maximum dimension. After evaluating the contribution to the new merged system, the least contributing states are omitted. Computationally it is more effective to add three two dimensional pseudo sites one after the other instead of one 8 dimensional site, such that there are now three easier consecutive subsystem truncations instead of one very ineffective big truncation. The pseudo site mapping introduced in Ref. [50] translates between a boson level $|\alpha\rangle$ with $\alpha \in \{1, 2, \dots, 2^N - 1\}$ phonons and an N-pseudo site state $|r_1, r_2, \dots, r_N\rangle$ with $r_j \in \{0, 1\}$ by

$$\alpha = \sum_{j=1}^N 2^{j-1} r_j. \quad (8.2)$$

This is very similar to the binary representation of decimal numbers and consequently means that the boson operators also have to be mapped to new pseudo site

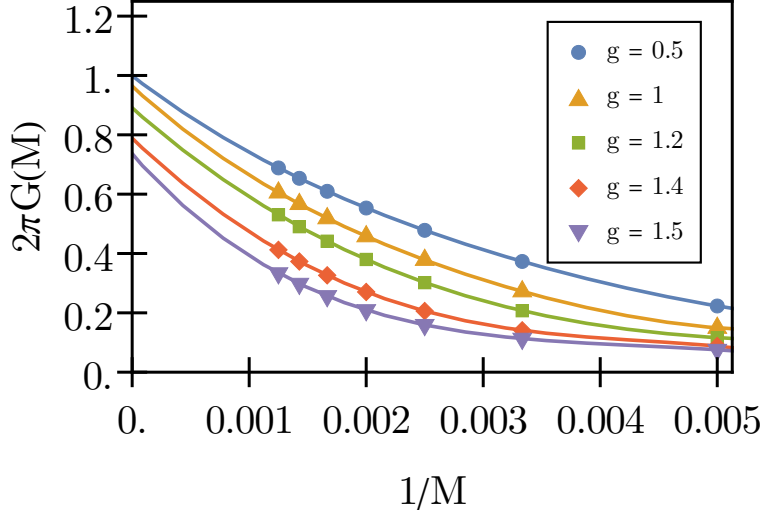


Figure 29: Same system as in Fig. 28 but for an intermediate phonon frequency $\omega_b = t$. The figure was published in Ref. [39].

operators via the relation

$$N_b = b^\dagger b = \sum_{j=1}^N 2^{j-1} a_j^\dagger a_j. \quad (8.3)$$

The trade off for this method is that typically the operators are much more complicated in the pseudo site basis and are formed of multiple terms depending on the number of pseudo sites N .

In all calculations the boson cutoff was chosen as $N_b = 3$ and therefore there are two pseudo sites per fermion site. Figure 27 shows schematically the Holstein chain setup in pseudo site representation.

The computation turned out to be much more demanding than the previous examples which limited the simulated chains to a maximum length of $M = 800$. The calculation for the longest setups took up to 600 CPU hours and 4GB of memory.

The DMRG procedure was used to study two different regimes. One in which the phonon frequency lies within in the adiabatic regime at $\omega_b = 0.1t$ and another where the frequency is of the same magnitude as the nearest neighbor hopping $\omega_b = t$ in the intermediate regime. The results and the extrapolation into the thermodynamic limit are depicted in Figure 28 and in Figure 29.

The conductance for the adiabatic case $\omega_b = 0.1t$ is very close to the quantum of conductance $G \approx G_0$ and decreases by a small amount for higher values of g . For the intermediate frequency $\omega_b = t$ the same principle is observed at a higher effect. For increasing g the conductance is deviating even stronger from G_0 in comparison to the first case.

According to the phase diagram for the Holstein model (see Ref. [51]) one ex-

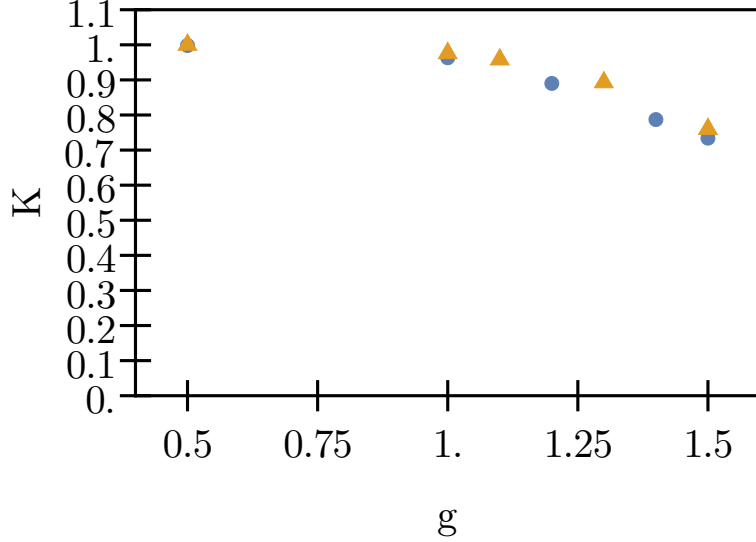


Figure 30: Luttinger parameter K for the Holstein chain in the case of a phonon frequency of $\omega_b = t$ against electron-phonon coupling g . The Luttinger parameter was determined from the conductance according to the data in Fig.29 (circles) and on the other hand from the charge structure factor in Ref. [51](triangles). The figure was published in Ref. [39].

pects a Luttinger liquid behavior for high phonon frequencies or small couplings. S. Ejima and H. Fehske computed the static charge structure factor, which allowed to extract the Luttinger liquid parameter in Ref. [51] for several different frequencies and electron-phonon couplings. Using the relation $G = K_L G_0$ allows to compare their results to the output of the DMRG method of this thesis. Figure 30 illustrates the comparison for the specific case of the intermediate phonon frequency $\omega_b = t$. The data matches astonishing well and points to a similar behavior for phonon coupled homogeneous chains. An increase in electron-phonon coupling g decreases the Luttinger liquid parameter K and therefore also decreases the conductance of the setup. There are no superconducting effects occurring and furthermore, there is no metal-insulator phase transition visible due to the weak coupling g restricted by the low phonon number per site. In order to see this phase transition a larger phonon cut off would be needed.

In summary, this shows that the DMRG method is a powerful tool for homogeneous noninteracting chains coupled to a small number of phonons. The method confirms that the relation for the conductance of a Luttinger liquid which was developed using pure fermion systems is extendable to the here discussed regime of weak phonon coupling.

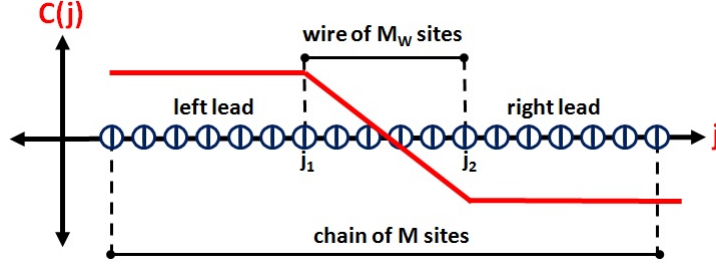


Figure 31: Schematics for a one-dimensional Hubbard chain half filled with spin- $\frac{1}{2}$ electrons for each kind of spin. Each site has now the possibility to harbor one electron of each spin. The shape of the perturbation is illustrated as $C(j)$.

9. Spinfull Fermions - Hubbard Chain

So far, the fermions were spinless in all models that were studied. Incorporating the spin degree of freedom allows to generalize the fermion description to electrons. The results were published in Ref. [39]. The Hamiltonian that describes the system of spinfull electrons with spin-spin Coulomb interaction is the Hubbard Hamiltonian

$$\begin{aligned}
 H_{\text{Hubbard}} &= H_{\text{Kin}} + H_{C2} \\
 &= -t \sum_{j=2}^M \sum_{\sigma} \left(c_{j,\sigma}^{\dagger} c_{j-1,\sigma} + \text{h.c.} \right) + U \sum_{j=1}^M n_{j,\uparrow} n_{j,\downarrow}.
 \end{aligned} \tag{9.1}$$

The kinetic tight-binding term is now spin selective and the second term describes the interaction between fermions of different spin σ . The chain is half filled with each kind of fermion such that there are twice as much charge carriers in the system as in the previous examples. Since now both kind of particle contribute to the current the effective charge current J_C is formed as

$$J_C = J_{\uparrow} + J_{\downarrow}, \tag{9.2}$$

$$J_{\sigma} = \frac{1}{M_W - 1} \frac{it}{\hbar} \sum_{j=j_1+1}^{j_2} \left(c_{j,\sigma}^{\dagger} c_{j-1,\sigma} - c_{j-1,\sigma}^{\dagger} c_{j,\sigma} \right). \tag{9.3}$$

In addition, adding spin to the system allows to look at a different kind of conductance that is dependent on the spin current instead of the charge current. The quantity of spin conductance can be derived in a very analogous way to the charge conductance by

$$G_S(\omega) = \lim_{V_{\text{SD}} \rightarrow 0} \text{Re} \left\{ \frac{q \langle J_S(\omega) \rangle}{V_{\text{SD}} f(\omega)} \right\} \tag{9.4}$$

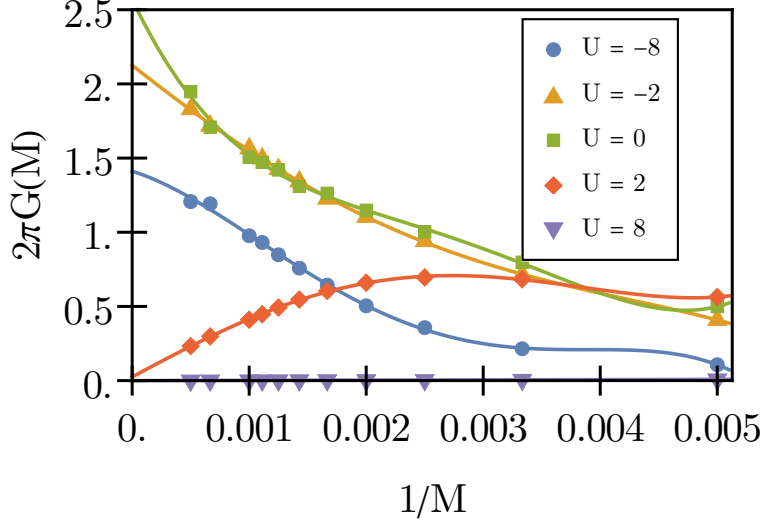


Figure 32: Charge conductance for the Hubbard chain against inverse system size $1/M$. There are polynomial fits for several Hubbard interactions U illustrated in the inset.

Key interest for this quantity is the expectation value of a generated spin current. The first step is to add a different perturbation to the system because an applied electrical field (1.18) like in the previous examples would not generate a spin current. In order to express this current as a linear response to the perturbation, the applied field has to couple selectively to the spins. Therefore, for the spin conductance the perturbation $\delta H(\tau)$ is of the nature of a magnetic field

$$\delta H(\tau) = qV_{\text{SD}}f(\tau) \sum_{j=1}^M C(j) (n_{j,\uparrow} - n_{j,\downarrow}). \quad (9.5)$$

Note that there is no other interaction in the base Hamiltonian of this model and the chain is therefore homogeneous. The leads and wire parts are only determined by the shape of this perturbation as depicted in Fig. 31. The spin current operator then can be formed by (9.3) as

$$J_{\text{S}} = J_{\uparrow} - J_{\downarrow}. \quad (9.6)$$

Analytically the model is solvable using the Bethe ansatz method [9]. The most interesting property of its low energy states is that charge- and spin excitations are separated. The gapless excitation modes can then be described as a Luttinger liquid. For the present case of half filling this leads to a symmetry between charge- and spin conductance regarding the interaction strength U and $-U$. For $U > 0$ the system is a Mott Insulator that still allows for gapless spin excitations, while for $U < 0$ the system changes to a Luther-Emery liquid [1], where the roles are reversed and spin excitation is gapped with gapless charge spectrum.

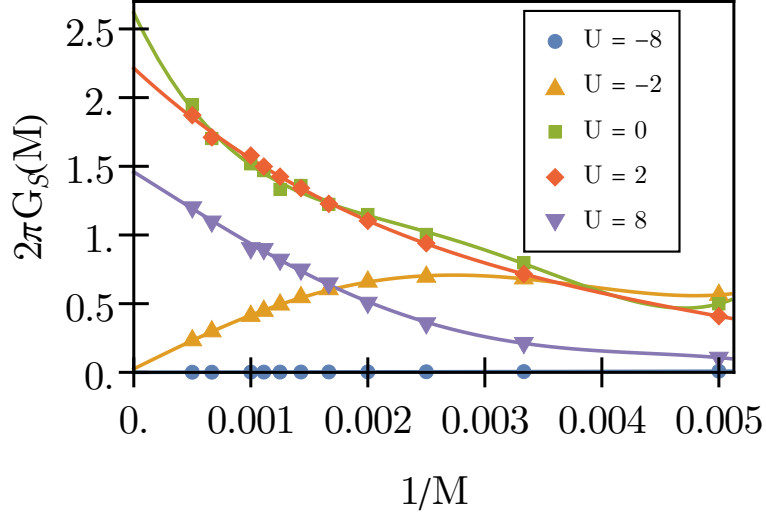


Figure 33: Spin conductance for the Hubbard chain against inverse system size $1/M$. There are polynomial fits for several Hubbard interactions U illustrated in the inset. The figure was published in Ref. [39].

Now all prerequisites are developed to use the DMRG method on the one-dimensional homogeneous Hubbard chain for the linear charge and spin conductance in the thermodynamic limit. In Figures 32 and 33 both quantities were extrapolated from a set of setups of different length and with different interaction parameters U . In direct comparison the mentioned symmetry is quite noticeable. There is not only symmetry visible in the values of the thermodynamic limits of the conductance but also in the finitely scaled systems as well. The limit of the case $U = 0$ shows a slight scattering and deviation from $G = 2G_0$, which would be the expected value for a tight-binding setup with two types of charge (spin) carriers. The reason is that the Hubbard model here has two gapless excitation modes while there is only a single one for any other interaction value. This decreases the accuracy of the DMRG algorithm for this specific example. For attractive values of $U < 0$ both the charge and spin conductance follow the expected behavior. The spin conductance completely vanishes due to the spin gap but the charge conductance is still finite because the spectrum is gapless. A qualitative difference in the extrapolation behavior of the spin conductance of these two examples might be due to the different correlation lengths associated with $U = -2t$ and $U = -8t$. We would expect a Mott insulator with gapped charge excitations and gapless spin excitations for repulsive interactions $U > 0$. That means the spin conductance G_S should approach $2G_0$. For the case of $U = 2t$ this can be extracted from the results. However, for $U = 8t$ this is not clear. The reason is that the spin excitations have a much smaller band width than in the previous examples. A different broadening $\eta \propto 4t^2/U$ would be needed and as a result a much larger system size to reach a higher resolution.

To conclude this chapter the procedure is still a viable tool for spinfull fermions,

but one has to be aware of its limitations. This chapter provides a good insight about what happens, when the DMRG loses its accuracy due to too many excitation modes, while on the other hand produces reliable results for nonvanishing interaction U .

10. Conclusion

The thesis presents a powerful procedure for the DC-conductance of one-dimensional correlated systems. It has shown its effectiveness for various model setups and also where its limits are.

At first the procedure was checked against simple noninteracting tight-binding chains (chapter 5) where the results were compared to the analytically calculated DC-conductance. Here, a variety of the surrounding parameters like an appropriate finite size scaling and wire length were determined.

For the models of homogeneous interacting chains presented in chapter 6 the method was able to reproduce the Luttinger liquid behavior in the respective regime of $V \in (-2t, 2t]$. After adding a barrier in the middle of the wire the results of the method were consistent with Landauer theory of elastic scattering [11]. Then the model was extended further to two barriers that were positioned either in neighboring sites or with a one site gap. Here, the results showed an either insulating phase or resonance depending on where the impurities are placed in relation to each other. This behavior was consistent with Kane and Fishers CDW picture explanation from Ref [36]

In chapter 7, an extension to the inhomogeneous interacting model was developed with setups that allow more realistic simulations of lead and wire material differences. The results were in strong agreement with field theory for a smooth transition [40, 41] from the leads through the wire and yielded backscattering once the transition became too sharp.

The DMRG method was able to retain up to 384 states after the truncation. The algorithm set out with a warmup for a maximum of 128 states and then performed a total of nine sweeps according to the infinite DMRG described in chapter 3. The number of states kept was increased after every three sweeps - after the first three sweeps reaching 256 states followed by 384 states after the second set of three sweeps.

For the more simple setups of homogeneous interaction the computation time required to calculate $G(M)$ for the largest chains was less than 100 CPU hours. For the Holstein setup of chapter 8 on the other hand the computation time was capped at 600 CPU hours and a total memory of 4GB was used. In addition, the maximum chain length in the Holstein chain was kept at $M = 800$ which is much smaller than the $M = 2000$ for the other setups. Nevertheless, the comparison of the results to similar studies [51] showed that even for this rather small setup the method is still a viable tool. One way to increase the calculation speed would be to reduce the number of frequencies for which $G(\omega, \eta, M_i)$ from equation (4.19) is calculated. However, this comes at the cost of a lower resolution around the value $\omega = 0$ when $G(M)$ is estimated.

In chapter 9 a spin and on site interaction was given to the fermions in the form of a Hubbard chain. The method was able to confirm some of the expected behavior but was limited by a broadening that turned out to be too large to resolve excitations for the smaller band gaps in the charge and spin conductance. In this specific example we saw that it also allows for the analysis of quantities that are similar to the conductance, in this case the spin-conductance. This only requires that the quantity is based on a Greens function [30] of the kind

$$G_{J,\eta}(\omega) = \left\langle 0 \left| J \frac{\eta}{(E_0 - H + \hbar\omega)^2 + \eta^2} J \right| 0 \right\rangle, \quad (10.1)$$

where J can be a current of any form that is the result of a linear response to a perturbation. This indicates that the method is also capable of studying quantities that would be based on other currents like an energy current [52–55].

Another field of study opens up when the underlying models are changed to disordered wires or ladder systems [56,57]. The method should definitely be suitable for such kind of systems as long as the current-current correlation functions can be calculated around $\omega = 0$ by the DMRG algorithm.

During the finite scaling process the wire length was not changed during the enlargement of the systems. This was based on the discovery in chapter 5 that the conductance scales with M_W/M . As a result a very small wire together with very large leads were chosen in all subsequent studies. In some cases like in the inhomogeneous interacting chain (chapter 7) the limit for an infinitely long wire would also be worth studying. This would definitely be something to investigate in the future.

A. Appendix

A.1. Current Operator as Linear Response to an External Field

The quantity of conductance discussed in chapter 1 is dependent on the expectation value of the current operator $\langle J \rangle$. Here, I show how to derive the current operator of equation (1.12) by following the explanations of the book [4] on linear response theory.

The lead-wire setup of chapter 1 was represented by a Hamiltonian H_0 . In order to generate an electron current a source-drain potential has to act on this system in the form of an perturbation $\delta H(\tau)$. The expectation value of the current operator can be expressed by making use of the corresponding density matrix $\rho(\tau)$.

$$\langle J \rangle(\tau) = \langle J \rangle_{\rho(\tau)} = \text{Tr}(J\rho(\tau)). \quad (\text{A.1})$$

Switching into the interaction picture gives J also time dependency

$$\text{Tr}(J\rho(\tau)) \rightarrow \text{Tr}(\hat{J}(\tau)\hat{\rho}(\tau)), \quad (\text{A.2})$$

$$\hat{O} = e^{i\frac{H_0}{\hbar}\tau} O e^{-i\frac{H_0}{\hbar}\tau}. \quad (\text{A.3})$$

Here, the interaction picture is denoted by a hat for an arbitrary operator O . The Von Neumann equation then reads

$$\frac{d}{d\tau}\hat{\rho}(\tau) = -\frac{iqV_{SD}f(\tau)}{\hbar}[\hat{A}(\tau), \hat{\rho}(\tau)]. \quad (\text{A.4})$$

Before the voltage is applied to the leads the system is in a state of equilibrium. In the chosen time scale this moment has happened long ago and lies infinitely far in the past. This means for $\tau \rightarrow -\infty$ the density operator can be expressed as

$$\rho_0 = \rho(-\infty) = \frac{1}{Z_0} e^{-\beta H_0}, \quad (\text{A.5})$$

$$\text{where } Z_0 = \sum_n e^{-\beta E_n} \quad (\text{A.6})$$

and β is the inverse temperature. This expression helps to integrate the Von Neumann equation (A.4) to arrive at

$$\hat{\rho}(\tau) = \rho_0 - \frac{iqV_{SD}}{\hbar} \int_{-\infty}^{\tau} [\hat{A}(\tau'), \hat{\rho}(\tau')] f(\tau') d\tau'. \quad (\text{A.7})$$

Iterating this formulation repeatedly yields

$$\begin{aligned} \hat{\rho}(\tau) = & \rho_0 - \frac{i}{\hbar} \int_{-\infty}^{\tau} [\hat{A}(\tau'), \rho_0] V_{\text{SD}} f(\tau') d\tau' \\ & - \frac{q^2 V_{\text{SD}}^2}{\hbar^2} \int_{-\infty}^{\tau} \int_{-\infty}^{\tau'} [\hat{A}(\tau''), [\hat{A}(\tau'), \rho_0]] f(\tau'') f(\tau') d\tau'' d\tau' + \dots \quad . \quad (\text{A.8}) \end{aligned}$$

Because higher orders are assumed to have a lower impact on the density matrix, this leaves only the first order contribution and thus the system is responding linearly to an external perturbation, which is why it is called linear response.

$$\hat{\rho}(\tau) = \rho_0 - \frac{iqV_{\text{SD}}}{\hbar} \int_{-\infty}^{\tau} [\hat{A}(\tau'), \rho_0] f(\tau') d\tau'. \quad (\text{A.9})$$

For the expectation value of the current operator equation (A.1) translates to

$$\langle J \rangle_{\rho(\tau)} = \langle J \rangle_{\rho_0} - \frac{iqV_{\text{SD}}}{\hbar} \int_{-\infty}^{\tau} \text{Tr}(\hat{J}(\tau) [\hat{A}(\tau'), \rho_0]) f(\tau') d\tau', \quad (\text{A.10})$$

$$= \langle J \rangle_{\rho_0} - \frac{iqV_{\text{SD}}}{\hbar} \int_{-\infty}^{\tau} \text{Tr}(\rho_0 [\hat{J}(\tau), \hat{A}(\tau')]) f(\tau') d\tau'. \quad (\text{A.11})$$

This expression is the basis for the formulation of the Kubo-conductance [7] in the next appendix chapter A.2.

A.2. Kubo Formulation of the Conductance

This section follows the derivation of the Kubo-conductance [7] by Dan Bohr in his PhD.-thesis (Ref. [5]). My derivation is a nearly one to one match, and the result is a well known formula in physics [4] and the basic quantity, which the method of this thesis is concerned about. Starting with the result of the last section, there are already two assumptions that can be made. First, there should be no equilibrium current and secondly for low temperatures the density matrix becomes

$$\begin{aligned}\rho_0(\beta \rightarrow \infty) &\approx e^{-\beta(H_0 - E_0)} = |0\rangle \langle 0|, \\ \langle J \rangle_{\rho_0} &= 0.\end{aligned}\tag{A.12}$$

Then equation (A.11) can be changed to

$$\begin{aligned}\langle J \rangle &= -\frac{iqV_{SD}}{\hbar} \int_{-\infty}^{\tau} \sum_m \langle m | e^{-\beta(H_0 - E_0)} [\hat{J}(\tau), \hat{A}(\tau')] | m \rangle f(\tau') d\tau', \\ &= -\frac{iqV_{SD}}{\hbar} \int_{-\infty}^{\tau} \sum_{m,n} \langle m | n \rangle \underbrace{e^{-\beta(E_n - E_0)}}_{\delta_{n0}} \langle n | [\hat{J}(\tau), \hat{A}(\tau')] | m \rangle f(\tau') d\tau', \\ &= -\frac{iqV_{SD}}{\hbar} \int_{-\infty}^{\tau} \langle 0 | [\hat{J}(\tau), \hat{A}(\tau')] | 0 \rangle f(\tau') d\tau'.\end{aligned}\tag{A.13}$$

Applying the Fourier transform $\mathcal{F}\{\}$ to this result opens up the frequency dependency of $J(\omega)$.

$$\begin{aligned}\mathcal{F}\{\langle J \rangle\} &= -\frac{iqV_{SD}}{\hbar} \int_{-\infty}^{\infty} e^{i\omega\tau} \int_{-\infty}^{\tau} \langle 0 | [\hat{J}(\tau), \hat{A}(\tau')] | 0 \rangle f(\tau') d\tau d\tau', \\ \langle J(\omega) \rangle &= -\frac{iqV_{SD}}{\hbar} \int_{-\infty}^{\infty} e^{i\omega\tau} \int_{-\infty}^{\infty} \theta(\tau - \tau') \langle 0 | [\hat{J}(\tau), \hat{A}(\tau')] | 0 \rangle f(\tau') d\tau d\tau', \\ &= -\frac{iqV_{SD}}{\hbar} \int_{-\infty}^{\infty} e^{i\omega\tau} \int_{-\infty}^{\infty} \theta(\tau - \tau') \langle 0 | [e^{\frac{i}{\hbar}H_0\tau} J e^{-\frac{i}{\hbar}H_0\tau}, e^{\frac{i}{\hbar}H_0\tau'} A e^{-\frac{i}{\hbar}H_0\tau'}] | 0 \rangle f(\tau') d\tau d\tau', \\ &= -\frac{iqV_{SD}}{\hbar} \int_{-\infty}^{\infty} e^{i\omega\tau} \int_{-\infty}^{\infty} \theta(\tau - \tau') \langle 0 | [\hat{J}(\tau - \tau'), A] | 0 \rangle f(\tau') d\tau d\tau', \\ &= \mathcal{F}\left\{qV_{SD}f(\tau') * -\frac{i}{\hbar}\theta(\tau - \tau') \langle 0 | [\hat{J}(\tau - \tau'), A] | 0 \rangle\right\}, \\ &= \mathcal{F}\left\{qV_{SD}f(\tau')\right\} \mathcal{F}\left\{-\frac{i}{\hbar}\theta(\tau - \tau') \langle 0 | [\hat{J}(\tau - \tau'), A] | 0 \rangle\right\}, \\ &= -\frac{iqV_{SD}}{\hbar} f(\omega) \int_0^{\infty} e^{i\omega\tau} \sum_m \left(\langle 0 | J | m \rangle \langle m | A | 0 \rangle e^{\frac{i}{\hbar}(E_0 - E_m)\tau} \right. \\ &\quad \left. - \langle 0 | A | m \rangle \langle m | J | 0 \rangle e^{-\frac{i}{\hbar}(E_0 - E_m)\tau} \right) d\tau,\end{aligned}\tag{A.14}$$

where in the last step the replacement $\tau - \tau' \rightarrow \tau$ happened and

$$f(\omega) = \mathcal{F} \left\{ f(\tau) \right\} = \int_{-\infty}^{\infty} e^{i\omega\tau} f(\tau) d\tau. \quad (\text{A.15})$$

Continuing following Dan Bohrs explanation by inverting the time axis transforms the operator A into the interaction picture representation \hat{A}

$$\begin{aligned} \langle J(\omega) \rangle &= \frac{iqV_{\text{SD}}}{\hbar} f(\omega) \int_0^{-\infty} e^{-i\omega\tau} \sum_m \langle 0| J |m\rangle \langle m| \hat{A} |0\rangle - \langle 0| \hat{A} |m\rangle \langle m| J |0\rangle d\tau, \\ &= \frac{iqV_{\text{SD}}}{\hbar} f(\omega) \int_0^{-\infty} e^{-i\omega\tau} \langle 0| [J, \hat{A}] |0\rangle d\tau, \\ &= \lim_{\eta \rightarrow 0} \frac{iqV_{\text{SD}}}{\hbar} f(\omega) \left(\left[\frac{e^{-(i\omega-\eta)\tau}}{-i\omega} \langle 0| [J, \hat{A}] |0\rangle \right]_{\tau=0}^{\tau=-\infty} - \int_0^{-\infty} \frac{e^{-(i\omega-\eta)\tau}}{-i\omega} \langle 0| [J, \hat{A}] |0\rangle d\tau \right), \\ &= \lim_{\eta \rightarrow 0} -\frac{V_{\text{SD}}}{\hbar\omega} f(\omega) \int_0^{-\infty} e^{-(i\omega-\eta)\tau} \langle 0| [J, \hat{J}] |0\rangle d\tau, \end{aligned} \quad (\text{A.16})$$

where a factor of $\lim_{\eta \rightarrow 0} e^{\eta\tau}$ helps the integral to converge and $\dot{\hat{A}} = -\hat{J}$. Now inserting the factor $\sum_m |m\rangle \langle m| = 1$.

$$\begin{aligned} \langle J(\omega) \rangle &= \lim_{\eta \rightarrow 0} -\frac{qV_{\text{SD}}}{\hbar\omega} f(\omega) \int_0^{-\infty} e^{-(i\omega-\eta)\tau} \sum_m \left(\langle 0| J |m\rangle \langle m| \hat{J} |0\rangle - \langle 0| \hat{J} |m\rangle \langle m| J |0\rangle \right) d\tau, \\ &= \lim_{\eta \rightarrow 0} -\frac{qV_{\text{SD}}}{\hbar\omega} f(\omega) \int_0^{-\infty} e^{-(i\omega-\eta)\tau} \\ &\quad \times \sum_m \left(\langle 0| J |m\rangle \langle m| J |0\rangle e^{\frac{i}{\hbar}(E_m-E_0)\tau} - \langle 0| J |m\rangle \langle m| J |0\rangle e^{-\frac{i}{\hbar}(E_m-E_0)\tau} \right) d\tau, \\ &= \lim_{\eta \rightarrow 0} -\frac{qV_{\text{SD}}}{\omega} f(\omega) \sum_m |\langle 0| J |m\rangle|^2 \left[\frac{e^{\frac{i}{\hbar}(E_m-E_0-\hbar\omega-i\hbar\eta)\tau}}{i(E_m-E_0-\hbar\omega-i\hbar\eta)} - \frac{e^{-\frac{i}{\hbar}(E_m-E_0+\hbar\omega+i\hbar\eta)\tau}}{-i(E_m-E_0+\hbar\omega+i\hbar\eta)} \right]_{\tau=0}^{\tau=-\infty}, \\ &= \lim_{\eta \rightarrow 0} \frac{qV_{\text{SD}}}{i\omega} f(\omega) \sum_m |\langle 0| J |m\rangle|^2 \left(\frac{1}{H_0-E_0-\hbar\omega-i\hbar\eta} + \frac{1}{H_0-E_0+\hbar\omega+i\hbar\eta} \right), \\ &= \lim_{\eta \rightarrow 0} \frac{qV_{\text{SD}}}{i\omega} f(\omega) \sum_m |\langle 0| J |m\rangle|^2 \left(\frac{H_0-E_0-\hbar\omega+i\hbar\eta}{(H_0-E_0-\hbar\omega)^2+(\hbar\eta)^2} + \frac{H_0-E_0+\hbar\omega-i\hbar\eta}{(H_0-E_0+\hbar\omega)^2+(\hbar\eta)^2} \right). \end{aligned} \quad (\text{A.17})$$

Only the real part contributes to the expectation value of $J(\omega)$. Therefore,

$$\begin{aligned} \text{Re}\{\langle J(\omega) \rangle\} &= \\ \lim_{\eta \rightarrow 0} \frac{q^2V_{\text{SD}}}{\omega} f(\omega) \sum_m |\langle 0| J |m\rangle|^2 &\left(\frac{\hbar\eta}{(E_m-E_0-\hbar\omega)^2+(\hbar\eta)^2} - \frac{\hbar\eta}{(E_m-E_0+\hbar\omega)^2+(\hbar\eta)^2} \right). \end{aligned} \quad (\text{A.18})$$

with formula (1.12) this leads to the Kubo formulation of conductance:

$$\begin{aligned}
G(\omega) &= \lim_{V_{\text{SD}} \rightarrow 0} \text{Re} \left\{ \frac{\langle J(\omega) \rangle}{V_{\text{SD}} f(\omega)} \right\} \\
&= \lim_{\eta \rightarrow 0} \frac{q^2}{\omega} \sum_m |\langle 0 | J | m \rangle|^2 \left(\frac{\hbar\eta}{(E_m - E_0 - \hbar\omega)^2 + (\hbar\eta)^2} - \frac{\hbar\eta}{(E_m - E_0 + \hbar\omega)^2 + (\hbar\eta)^2} \right)
\end{aligned}
\tag{A.19}$$

B. Appendix

B.1. Scaling Analysis

In this chapter the scaling behavior for $G(\omega, \eta)$ for $M \gg 1$ and $\omega \rightarrow 0$ is investigated for the special cases of a linear applied electromagnetic potential and a step like potential over the whole chain. As discussed in chapter 2 the shape of these two cases is described through the coefficients $\Delta C(i)$

$$G(\omega, \eta) = \frac{q^2}{\omega} \sum_m |\langle m|J|0\rangle|^2 L(\omega, \eta, m) \quad (\text{B.1})$$

$$\Delta C_{\text{Linear}} = -\frac{1}{M-1}, \quad (\text{B.2})$$

$$\Delta C(i)_{A\text{Step}} = \begin{cases} -\frac{1}{2} & \text{for } i = j_1, \\ -\frac{1}{2} & \text{for } i = j_2, \\ 0 & \text{else,} \end{cases} \quad (\text{B.3})$$

, where $L(\omega, \eta, m)$ represents the Lorentzian terms. The model system is the non interacting tight-binding chain of spinless fermions that is used in chapter 5. The wavefunctions from the chapter help to express the sum in $G(\omega, \eta)$ as in expression (5.14) as

$$\sum_m |\langle m|J|0\rangle|^2 L(\omega, \eta, m) = \sum_{\substack{k' \leq k_F \\ k > k_F}} \left| \sum_{i=2}^M \Delta C(i) J_i^{k,k'} \right|^2 L(\omega, \eta, m). \quad (\text{B.4})$$

Starting with the linear case the inner part becomes

$$\sum_{j=2}^M \Delta C_{\text{Linear}} J_j^{k,k'} = \frac{2it}{\hbar(M^2-1)} \sum_{j=2}^M \left[\sin(kj) \sin(k'(j-1)) - \sin(k(j-1)) \sin(k'j) \right], \quad (\text{B.5})$$

$$= \frac{4it}{\hbar(M^2-1)} \sin(k') \sum_{j=1}^M \sin(kj) \sin(k'j), \quad (\text{B.6})$$

The $\sum_{j=1}^M \sin(kj) \cos(k'j)$ -term can now be expressed as

$$\begin{aligned} \sum_{j=1}^M \sin(kj) \cos(k'j) &= \frac{1}{4i} \sum_{j=1}^M \left(e^{ikj} - e^{-ikj} \right) \left(e^{ik'j} + e^{-ik'j} \right) \\ &= \frac{1}{4i} \sum_{j=1}^M e^{i(k+k')j} + e^{i(k-k')j} - e^{i(k'-k)j} - e^{-i(k+k')j}. \end{aligned} \quad (\text{B.7})$$

In the next step the finite geometric series $\sum_{j=a}^b r^j = \frac{r^a - r^{b+1}}{1-r}$ will be used, such that

$$\begin{aligned} & \frac{1}{4i} \sum_{j=1}^M e^{i(k+k')j} + e^{i(k-k')j} - e^{i(k'-k)j} - e^{-i(k+k')j} \\ &= \frac{1}{4i} \left(\frac{e^{i(k+k')} - e^{i(k+k')(M+1)}}{1 - e^{i(k+k')}} + \frac{e^{i(k-k')} - e^{i(k-k')(M+1)}}{1 - e^{i(k-k')}} \right. \\ & \quad \left. - \frac{e^{i(k'-k)} - e^{i(k'-k)(M+1)}}{1 - e^{i(k'-k)}} - \frac{e^{-i(k+k')} - e^{-i(k+k')(M+1)}}{1 - e^{-i(k+k')}} \right). \end{aligned} \quad (\text{B.8})$$

Here the interesting terms are

$$\begin{aligned} e^{i(k+k')(M+1)} &= e^{i\pi(n+n')} = (-1)^{n+n'} \\ e^{i(k-k')(M+1)} &= e^{i\pi(n-n')} = (-1)^{n-n'}. \end{aligned} \quad (\text{B.9})$$

Therefore, the sum changes to

$$\begin{aligned} \sum_{i=1}^M \sin(ki) \cos(k'i) &= \frac{1}{4i} \left(\frac{e^{i(k+k')} - (-1)^{n+n'}}{1 - e^{i(k+k')}} + \frac{e^{i(k-k')} - (-1)^{n-n'}}{1 - e^{i(k-k')}} \right. \\ & \quad \left. - \frac{e^{i(k'-k)} - (-1)^{n'-n}}{1 - e^{i(k'-k)}} - \frac{e^{-i(k+k')} - (-1)^{n+n'}}{1 - e^{-i(k+k')}} \right) \\ &= \frac{1}{4i} \left(\frac{e^{i(k+k')} - (-1)^{n+n'}}{1 - e^{i(k+k')}} + \frac{e^{i(k-k')} - (-1)^{n-n'}}{1 - e^{i(k-k')}} \right. \\ & \quad \left. - \frac{e^{i(k'-k)} - (-1)^{n'-n}}{1 - e^{i(k'-k)}} - \frac{e^{-i(k+k')} - (-1)^{n+n'}}{1 - e^{-i(k+k')}} \right) \\ &= \frac{1}{4i} \left(\frac{1 + e^{i(k+k')}}{1 - e^{i(k+k')}} + \frac{1 + e^{i(k-k')}}{1 - e^{i(k-k')}} - \frac{1 + e^{i(k'-k)}}{1 - e^{i(k'-k)}} - \frac{1 + e^{-i(k+k')}}{1 - e^{-i(k+k')}} \right), \end{aligned} \quad (\text{B.10})$$

if $n + n'$ is odd and zero otherwise. Additionally, with

$$\cot(x) = \frac{\cos(x)}{\sin(x)} = i \frac{1 + e^{-2x}}{1 - e^{-2x}} \quad (\text{B.11})$$

it becomes

$$\begin{aligned} \sum_{i=1}^M \sin(ki) \cos(k'i) &= \frac{1}{2} \left(\cot \left(\frac{k+k'}{2} \right) + \cot \left(\frac{k-k'}{2} \right) \right) \\ &= \frac{1}{2} \frac{\sin(k)}{\sin(\frac{k+k'}{2}) \sin(\frac{k-k'}{2})} = \frac{\sin(k)}{\cos(k') - \cos(k)} h(k, k'), \end{aligned} \quad (\text{B.12})$$

where $h(k, k') = 1$ when $n + n'$ is odd and 0 for the even case. Therefore, for the linear case $G_{\text{Linear}}(\omega, \eta)$ becomes

$$\begin{aligned}
G_{\text{Linear}}(\omega, \eta) &= \frac{q^2}{\omega} \sum_{\substack{k' \leq k_F \\ k > k_F}} \left| \sum_{i=2}^M \Delta C(i)_{\text{Linear}} J_i^{k, k'} \right|^2 \left(\frac{\hbar\eta}{(E_m - E_0 - \hbar\omega)^2 + (\hbar\eta)^2} - \frac{\hbar\eta}{(E_m - E_0 + \hbar\omega)^2 + (\hbar\eta)^2} \right), \\
&= \frac{q^2 16t^2}{\hbar^2 (M^2 - 1)^2 \omega} \sum_{\substack{k' \leq k_F \\ k > k_F}} \frac{\sin(k)^2 \sin(k')^2}{(\cos(k') - \cos(k))^2} h(k, k') \\
&\quad \times \left(\frac{\hbar\eta}{(E_m - E_0 - \hbar\omega)^2 + (\hbar\eta)^2} - \frac{\hbar\eta}{(E_m - E_0 + \hbar\omega)^2 + (\hbar\eta)^2} \right). \tag{B.13}
\end{aligned}$$

Next an expression $G_{\text{Step}}(\omega, \eta)$ for the step potential is derived. For this case only two terms in the sum of (B.4) contribute.

$$\begin{aligned}
\sum_{j=2}^M \Delta C_{\text{Step}}(j) J_j^{k, k'} &= \frac{it}{\hbar(M+1)} \left[\sin(kj_1) \sin(k'(j_1 - 1)) - \sin(k(j_1 - 1)) \sin(k'j_1) \right. \\
&\quad \left. + \sin(kj_2) \sin(k'(j_2 - 1)) - \sin(k(j_2 - 1)) \sin(k'j_2) \right], \\
&= \frac{it}{\hbar(M+1)} \left[\sin\left(k\left(\frac{M - M_W}{2} + 1\right)\right) \sin\left(k'\left(\frac{M - M_W}{2}\right)\right) \right. \\
&\quad - \sin\left(k\left(\frac{M - M_W}{2}\right)\right) \sin\left(k'\left(\frac{M - M_W}{2} + 1\right)\right) \\
&\quad + \sin\left(k\left(\frac{M + 1 + M_W}{2} + 1\right)\right) \sin\left(k'\left(\frac{M + M_W}{2}\right)\right) \\
&\quad \left. - \sin\left(k\left(\frac{M + M_W}{2}\right)\right) \sin\left(k'\left(\frac{M + M_W}{2} + 1\right)\right) \right], \\
&= \frac{it}{\hbar(M+1)} \left[\sin\left(k\left(\frac{M + 1 - M_W}{2} + \frac{k}{2}\right)\right) \sin\left(k'\left(\frac{M + 1 - M_W}{2} - \frac{k'}{2}\right)\right) \right. \\
&\quad - \sin\left(k\left(\frac{M + 1 - M_W}{2} - \frac{k}{2}\right)\right) \sin\left(k'\left(\frac{M + 1 - M_W}{2} + \frac{k'}{2}\right)\right) \\
&\quad + \sin\left(k\left(\frac{M + 1 + M_W}{2} + \frac{k}{2}\right)\right) \sin\left(k'\left(\frac{M + 1 + M_W}{2} - \frac{k'}{2}\right)\right) \\
&\quad \left. - \sin\left(k\left(\frac{M + 1 + M_W}{2} - \frac{k}{2}\right)\right) \sin\left(k'\left(\frac{M + 1 + M_W}{2} + \frac{k'}{2}\right)\right) \right]. \tag{B.14}
\end{aligned}$$

Replacing $A_+ = \frac{M+1+M_W}{2}$ and $A_- = \frac{M+1-M_W}{2}$ reveals the following pattern for the four occurring terms

$$\begin{aligned}
\sin(lA_\pm + \frac{l}{2}) \sin(mA_\pm - \frac{m}{2}) &= \left(\sin(lA_\pm) \cos(\frac{l}{2}) + \cos(lA_\pm) \sin(\frac{l}{2}) \right) \\
&\quad \times \left(\sin(mA_\pm) \cos(\frac{m}{2}) - \cos(mA_\pm) \sin(\frac{m}{2}) \right), \\
&= \sin(lA_\pm) \sin(mA_\pm) \cos(\frac{l}{2}) \cos(\frac{m}{2}) \\
&\quad + \cos(lA_\pm) \sin(mA_\pm) \sin(\frac{l}{2}) \cos(\frac{m}{2}) \\
&\quad - \sin(lA_\pm) \cos(mA_\pm) \cos(\frac{l}{2}) \sin(\frac{m}{2}) \\
&\quad - \cos(lA_\pm) \cos(mA_\pm) \sin(\frac{l}{2}) \sin(\frac{m}{2}). \tag{B.15}
\end{aligned}$$

This transforms the previous expression to

$$\begin{aligned}
\sum_{j=2}^M \Delta C_{\text{Step}}(j) J_j^{k,k'} &= \frac{it}{\hbar(M+1)} \left[\sin(kA_- + \frac{k}{2}) \sin(k'A_- - \frac{k'}{2}) - \sin(kA_- - \frac{k}{2}) \sin(k'A_- + \frac{k'}{2}) \right. \\
&\quad \left. + \sin(kA_+ + \frac{k}{2}) \sin(k'A_+ - \frac{k'}{2}) - \sin(kA_+ - \frac{k}{2}) \sin(k'A_+ + \frac{k'}{2}) \right], \\
&= \frac{2it}{\hbar(M+1)} \left[\cos(kA_-) \sin(k'A_-) \sin(\frac{k}{2}) \cos(\frac{k'}{2}) \right. \\
&\quad - \sin(kA_-) \cos(k'A_-) \cos(\frac{k}{2}) \sin(\frac{k'}{2}) \\
&\quad + \cos(kA_+) \sin(k'A_+) \sin(\frac{k}{2}) \cos(\frac{k'}{2}) \\
&\quad \left. - \sin(kA_+) \cos(k'A_+) \cos(\frac{k}{2}) \sin(\frac{k'}{2}) \right]. \tag{B.16}
\end{aligned}$$

Using the definitions (5.4) reveals the following relations

$$kA_+ = \frac{n\pi}{2} + k \frac{M_W}{2}, \tag{B.17}$$

$$kA_- = \frac{n\pi}{2} - k \frac{M_W}{2}. \tag{B.18}$$

$$\tag{B.19}$$

$$\begin{aligned}
\sum_{j=2}^M \Delta C_{\text{Step}}(j) J_j^{k,k'} &= \frac{2it}{\hbar(M+1)} \left[\cos\left(\frac{n\pi}{2} - k\frac{M_W}{2}\right) \sin\left(\frac{n'\pi}{2} - k'\frac{M_W}{2}\right) \sin\left(\frac{k}{2}\right) \cos\left(\frac{k'}{2}\right) \right. \\
&\quad - \sin\left(\frac{n\pi}{2} - k\frac{M_W}{2}\right) \cos\left(\frac{n'\pi}{2} - k'\frac{M_W}{2}\right) \cos\left(\frac{k}{2}\right) \sin\left(\frac{k'}{2}\right) \\
&\quad + \cos\left(k\frac{n\pi}{2} + k\frac{M_W}{2}\right) \sin\left(\frac{n'\pi}{2} + k'\frac{M_W}{2}\right) \sin\left(\frac{k}{2}\right) \cos\left(\frac{k'}{2}\right) \\
&\quad \left. - \sin\left(k\frac{n\pi}{2} + k\frac{M_W}{2}\right) \cos\left(\frac{n'\pi}{2} + k'\frac{M_W}{2}\right) \cos\left(\frac{k}{2}\right) \sin\left(\frac{k'}{2}\right) \right].
\end{aligned} \tag{B.20}$$

The expression has now four possibilities depending on if n and n' are even or odd, where only two are non-zero

$$\begin{aligned}
\sum_{j=2}^M \Delta C_{\text{Step}}(j) J_j^{k,k'} &= \\
(-1)^{\frac{n+n'-1}{2}} \frac{2it}{\hbar(M+1)} &\begin{cases} \cos\left(\frac{(k+k')M_W}{2}\right) \sin\left(\frac{k-k'}{2}\right) - \cos\left(\frac{(k-k')M_W}{2}\right) \sin\left(\frac{k+k'}{2}\right) & \text{for } n \text{ odd, } n' \text{ even,} \\ \cos\left(\frac{(k-k')M_W}{2}\right) \sin\left(\frac{k+k'}{2}\right) + \cos\left(\frac{(k+k')M_W}{2}\right) \sin\left(\frac{k-k'}{2}\right) & \text{for } n \text{ even, } n' \text{ odd.} \end{cases}
\end{aligned} \tag{B.21}$$

Using these results $G_{\text{Step}}(\omega, \eta)$ finally becomes

$$\begin{aligned}
G_{\text{Step}}(\omega, \eta) &= \frac{k'^2}{\omega} \sum_{\substack{k' \leq k_F \\ k > k_F}} \left| \sum_{i=2}^M \Delta C(i)_{\text{Step}} J_i^{k,k'} \right|^2 \left(\frac{\hbar\eta}{(E_m - E_0 - \hbar\omega)^2 + (\hbar\eta)^2} - \frac{\hbar\eta}{(E_m - E_0 + \hbar\omega)^2 + (\hbar\eta)^2} \right), \\
&= \frac{k'^2 4t^2}{\hbar^2 (M+1)^2 \omega} \sum_{\substack{k' \leq k_F \\ k > k_F}} 2 \left[\cos^2\left(\frac{(k+k')M_W}{2}\right) \sin^2\left(\frac{k-k'}{2}\right) + \cos^2\left(\frac{(k-k')M_W}{2}\right) \sin^2\left(\frac{k+k'}{2}\right) \right] \\
&\quad \times \left(\frac{\hbar\eta}{(E_m - E_0 - \hbar\omega)^2 + (\hbar\eta)^2} - \frac{\hbar\eta}{(E_m - E_0 + \hbar\omega)^2 + (\hbar\eta)^2} \right). \tag{B.22}
\end{aligned}$$

Now the two expressions $G_{\text{Linear}}(\omega, \eta)$ and $G_{\text{Step}}(\omega, \eta)$ can be investigated for their scaling behavior for $M \gg 1$ and $\omega \rightarrow 0$. Starting with the linear case and by using

$$E(k, k') = -2t \cos(k) + 2t \cos(k') \tag{B.23}$$

$G_{\text{Linear}}(\omega, \eta)$ can be written as

$$G_{\text{Linear}}(\omega, \eta) = \frac{q^2 16t^2}{\hbar^2 (M^2 - 1)^2} \sum_{\substack{k' \leq k_F \\ k > k_F}} \frac{\sin(k)^2 \sin(k')^2}{E(k, k') (\cos(k') - \cos(k))^2} h(k, k') \\ \times \left(\frac{\hbar\eta}{(E(k, k') - \hbar\omega)^2 + (\hbar\eta)^2} - \frac{\hbar\eta}{(E(k, k') + \hbar\omega)^2 + (\hbar\eta)^2} \right). \quad (\text{B.24})$$

Now assuming a fixed η and a very large system size $M \gg 1$ the difference $k - k'$ is assumed to be close to zero. This is only possible if $k \rightarrow k_F^+$ and $k' \rightarrow k_F^-$. This allows for the following approximations

$$\sin^2(k) \approx \sin^2(k_F), \quad (\text{B.25})$$

$$\sin^2(k') \approx \sin^2(k_F), \quad (\text{B.26})$$

$$(\cos(k') - \cos(k))^2 \approx \sin^2(k_F)(k' - k)^2, \quad (\text{B.27})$$

$$E(k, k') \approx 2t \sin(k_F)(k - k'), \quad (\text{B.28})$$

$$\frac{\hbar\eta}{(E(k, k') \pm \hbar\omega)^2 + (\hbar\eta)^2} \approx \frac{1}{\hbar\eta}. \quad (\text{B.29})$$

This brings the finite frequency dependent conductance down to

$$G_{\text{Linear}}(\omega \rightarrow 0, \eta) \approx \frac{q^2 16t \sin(k_F)}{\hbar^2 \pi^3 \eta M} \sum_{n=1}^{n_F} \sum_{n'=n_{F+1}}^M \frac{1}{(n' - n)^3} \text{ for } n + n' \text{ odd}. \quad (\text{B.30})$$

Using $d = n - n'$ the sum can be transformed to

$$\sum_{n=1}^{n_F} \sum_{n'=n_{F+1}}^M \frac{1}{(n' - n)^3} \text{ for } n + n' \text{ odd}, \\ = \sum_{d \text{ is odd}} \frac{1}{d^3} \sum_{n=1}^{n_F} \sum_{n'=n_{F+1}}^M \delta_{n-n', d}, \\ = \sum_{d \text{ is odd}} \frac{1}{d^2} = \sum_d \frac{1}{d^2} - \sum_{d \text{ is even}} \frac{1}{d^2} = \frac{\pi^2}{6} - \frac{1}{4} \sum_d \frac{1}{d^2} = \frac{\pi^2}{8} \quad (\text{B.31})$$

So finally the expression can be approximated by

$$G_{\text{Linear}}(\omega \rightarrow 0, \eta) \approx \frac{q^2 2t \sin(k_F)}{\hbar^2 \pi \eta M} = \frac{q^2 v_F}{\hbar} \frac{1}{\pi \eta M} = \frac{D}{\pi \eta M} \quad (\text{B.32})$$

This means the finite conductance for the linear perturbation is proportional to the Drude weight D , which fits the observation that was made for the conductivity in equation (1.6). It also means that $G_{\text{Linear}}(\omega, \eta)$, is not useful in order to determine the real DC-conductance because of the potential shape that is spanned across the

whole setup.

Now the other case $G_{\text{Step}}(\omega, \eta)$ will be investigated. Since in this expression only two terms of the sum remain we look at the limit $\lim_{\eta \rightarrow 0^+} G_{\text{Step}}(\omega, \eta) = G_{\text{Step}}(\omega)$ and also transform the infinite sums into integrals via

$$\sum_{|k'| \leq k_F} \Delta k f(k') \stackrel{M \rightarrow \infty}{=} \int_0^{k_F} dk' f(k'),$$

$$\Delta k = \frac{\pi}{M+1} \quad (\text{B.33})$$

such that

$$G_{\text{Step}}(\omega) = \frac{k'^2 8t^2 \pi}{\hbar^2 (M+1)^2 \omega} \frac{(M+1)^2}{4\pi^2} \int_0^{k_F} dk' \int_{k_F}^{\pi} dk$$

$$\left[\cos^2\left((k+k')\frac{M_W}{2}\right) \sin^2\left(\frac{k-k'}{2}\right) + \cos^2\left((k-k')\frac{M_W}{2}\right) \sin^2\left(\frac{k+k'}{2}\right) \right]$$

$$\times \left(\delta(E(k, k') - \hbar\omega) - \delta(E(k, k') + \hbar\omega) \right). \quad (\text{B.34})$$

As before $k - k_F$ and $k_F - k'$ only contribute when they are small in the regime of small ω .

$$G_{\text{Step}}(\omega) = \frac{k'^2 8t^2 \pi}{\hbar^2 (M+1)^2 \omega} \frac{(M+1)^2}{4\pi^2} \int_0^{k_F} dk' \int_{k_F}^{\pi} dk$$

$$\left[\cos^2(k_F M_W) \frac{(k-k')^2}{4} + \sin^2(k_F) \right]$$

$$\times \left(\delta(E(k, k') - \hbar\omega) - \delta(E(k, k') + \hbar\omega) \right).$$

$$= \frac{q^2}{h} \left[1 + \frac{1}{\hbar\omega} \int_{-2t}^{\epsilon_F} d\epsilon' \int_{\epsilon_F}^{\epsilon'} d\epsilon \cos^2(k_F M_W) \frac{\epsilon - \epsilon'}{4(v_F)^2} \right.$$

$$\left. \times \left(\delta(\epsilon - \epsilon' - \hbar\omega) - \delta(\epsilon - \epsilon' + \hbar\omega) \right) \right].$$

$$= \frac{q^2}{h} \left[1 + \frac{1}{\hbar\omega} \cos^2(k_F M_W) \frac{1}{4} \frac{\omega^2}{v_F^2} \right.$$

$$\left. \times \left(\int_{\epsilon_F - \hbar\omega}^{\epsilon_F} d\epsilon' \theta(\omega) - \int_{\epsilon_F + \hbar\omega}^{\epsilon_F} d\epsilon' \theta(-\omega) \right) \right].$$

$$= \frac{q^2}{h} \left[1 + \cos^2(k_F M_W) \frac{1}{4} \frac{\omega^2}{v_F^2} \right], \quad (\text{B.35})$$

where $\theta(\omega)$ is the Heaviside function. This shows that in accordance with the conductivity in equation (1.8) a locally restricted potential leads to a result that is proportional to the quantum of conductance $G_0 = \frac{q^2}{h}$ for $\omega \rightarrow 0$.

C. Appendix

C.1. Elastic Scattering - Single Barrier

This section calculates the transmission coefficient of a single particle scattering problem for a barrier of strength ϵ in one dimension. The following calculations are very basic and resemble the standard problems taught in quantum mechanics classes as in Ref. [58]. For the two sections on the left and right side of the barrier the single particle wave function is assumed to follow the structure

$$\begin{aligned}\psi_L(x) &= e^{ikx} + \sqrt{R}e^{-ikx}, \\ \psi_R(x) &= \sqrt{T}e^{ikx},\end{aligned}\tag{C.1}$$

where $\psi_L(\psi_R)$ describes the left(right) part of the wave function. At the site of the impurity which is chosen to be at $x = 0$ the wave function has to have a definitive value such that

$$\begin{aligned}\psi_L(0) &= \psi_R(0), \\ \Rightarrow 1 + \sqrt{R} &= \sqrt{T}.\end{aligned}\tag{C.2}$$

Schroedingers Equation in conjunction with the energy 5.5 of the homogeneous non-interacting chain delivers additional information about the wave function by

$$\begin{aligned}E\psi(x) &= -t\psi(x+1) - t\psi(x-1) + \epsilon\psi(0)\delta_{x0}, \\ E\psi(0) &= -t\psi(1) - t\psi(-1) + \epsilon\psi(0), \\ E &= -2t\cos(k).\end{aligned}\tag{C.3}$$

The ansatz is to calculate the amplitude for the wave function that is transmitted. Expressing these conditions in terms of the transmission amplitude results in

$$\begin{aligned}E\sqrt{T} &= -t(\sqrt{T}e^{ik}) - t(e^{-ik} + \sqrt{R}e^{ik}) + \epsilon\sqrt{T}, \\ E\sqrt{T} &= -t(\sqrt{T}e^{ik}) - t(e^{-ik} + [\sqrt{T} - 1]e^{ik}) + \epsilon\sqrt{T} \\ E\sqrt{T} &= -t\sqrt{T}(e^{ik} + e^{ik}) - t(e^{-ik} - e^{ik}) + \epsilon\sqrt{T}, \\ [E - \epsilon + 2t(e^{ik})]\sqrt{T} &= i2t\sin(k), \\ \sqrt{T} &= \frac{i2t\sin(k)}{2te^{ik} - 2t\cos(k) - \epsilon}.\end{aligned}\tag{C.4}$$

Thus, the transmission coefficient is

$$\begin{aligned}
T = |\sqrt{T}|^2 &= \frac{4t^2 \sin(k)^2}{(2t[e^{ik} - \cos(k)] - \epsilon)(2t[e^{-ik} - \cos(k)] - \epsilon)}, \\
&= \frac{4t^2 \sin(k)^2}{4t^2[e^{-ik} - \cos(k)][e^{ik} - \cos(k)] - 2t\epsilon[e^{-ik} - \cos(k)] - 2t\epsilon[e^{ik} - \cos(k)] + \epsilon^2}, \\
&= \frac{4t^2 \sin(k)^2}{4t^2[1 - \cos(k)e^{ik} - \cos(k)e^{-ik} + \cos(k)^2] - 2t\epsilon[e^{-ik} + e^{ik}] + 4t\epsilon \cos(k) + \epsilon^2}, \\
&= \frac{4t^2 \sin(k)^2}{4t^2[1 - \cos(k)[e^{ik} + e^{-ik}] + \cos(k)^2] - 4t\epsilon \cos(k) + 4t\epsilon \cos(k) + \epsilon^2}, \\
&= \frac{4t^2 \sin(k)^2}{4t^2[1 - 2\cos(k)^2 + \cos(k)^2] + \epsilon^2}, \\
&= \frac{4t^2 \sin(k)^2}{4t^2[\sin(k)^2] + \epsilon^2}. \tag{C.5}
\end{aligned}$$

This is the transmission coefficient for just one particle. For a half filled chain of non-interacting fermions the transmission can be evaluated by using the expression for $k = k_F = \pi/2$.

C.2. Elastic Scattering - Two Barriers

Here the calculation for the transmission T of a system of two barriers placed in a one-dimensional chain at positions $x = 0$ and $x = a$ is presented in very analogous way to the bachelor's thesis of Jerome Jebai(Ref. [38]). The ansatz is the same as before for one barrier just that this time the wave function can be expressed in three sectional functions that are created by the two impurities.

$$\psi(x) = \begin{cases} e^{ikx} + \sqrt{R_1}e^{-ikx} & \text{for } x \leq 0, \\ \sqrt{T_1}e^{ikx} + \sqrt{R_2}e^{-ikx} & \text{for } 0 < x < a, \\ \sqrt{T_2}e^{ikx} & \text{for } x \geq a. \end{cases} \quad (\text{C.6})$$

The amplitudes of the waves are denoted by \sqrt{R} and \sqrt{T} for the reflected and transmitted part. The wave vectors k are real and the amplitude of the incoming wave is normalized to 1. The wave functions have to coincide at the specific location of the impurities such that two conditions are formed as

$$1 + \sqrt{R_1} = \sqrt{T_1} + \sqrt{R_2}, \quad (\text{C.7})$$

$$\sqrt{T_1}e^{ika} + \sqrt{R_2}e^{-ika} = \sqrt{T_2}e^{ika}. \quad (\text{C.8})$$

In addition, Schroedingers equation together with the energy spectrum for a chain with non interacting fermions 5.5 evaluated at the two impurities delivers two more constraints. Here the barriers are modelled as chemical potentials at the specific site.

$$E\psi(x) = -t\psi(x+1) - t\psi(x-1) + \epsilon_1\psi(x)\delta_{x0} + \epsilon_2\psi(x)\delta_{xa}, \quad (\text{C.9})$$

$$E\psi(0) = -t\psi(1) - t\psi(-1) + \epsilon_1\psi(0)\delta_{00}, \quad (\text{C.10})$$

$$E\psi(a) = -t\psi(a+1) - t\psi(a-1) + \epsilon_2\psi(a)\delta_{aa}. \quad (\text{C.11})$$

There are now four unknown amplitudes that can be solved for by a system of four equations. The transmission is the absolute value of the amplitude of the transmitted wave after the second barrier

$$T = |\sqrt{T_2}|^2. \quad (\text{C.12})$$

Solving first for $\sqrt{T_2}$ results in

$$\sqrt{T_2} = \frac{2it \sin(k)}{2it \sin(k) - \epsilon_1 - \epsilon_2 - \frac{\epsilon_1 \epsilon_2 (e^{2ika} - 1)}{2it \sin(k)}}, \quad (\text{C.13})$$

which in turn provides a general formulation for the transmission of a single particle of wave number k for two barriers placed at $x = 0$ and $x = a$ of respective barrier strength ϵ_1 and ϵ_2 as

$$T(a, \epsilon_1, \epsilon_2) = \frac{4t^2 \sin^2(k)}{4t^2 \sin^2(k) + \epsilon_1^2 + \epsilon_2^2 + \epsilon_1 \epsilon_2 \left(2 \cos(2ka) + \frac{\epsilon_1 + \epsilon_2}{t} \frac{\sin(2ka)}{\sin(k)} + \frac{\epsilon_1 \epsilon_2}{t^2} \frac{\sin^2(ka)}{\sin^2(k)} \right)} \quad (\text{C.14})$$

This formula is used in section 6.3 to make qualitative comparison to the interacting case.

$$T(k, a, \epsilon_1, \epsilon_2) = |\sqrt{T_2}|^2 = \frac{4t^2 \sin^2(k)}{4t^2 \sin^2(k) + \epsilon_1^2 + \epsilon_2^2 + \epsilon_1 \epsilon_2 \left(2 \cos(2ka) + \frac{\epsilon_1 + \epsilon_2}{t} \frac{\sin(2ka)}{\sin(k)} + \frac{\epsilon_1 \epsilon_2}{t^2} \frac{\sin^2(ka)}{\sin^2(k)} \right)} \quad (\text{C.15})$$

The following expressions are calculations according to the cases a)-f) depicted in the schematics 17 for different types of impurity combinations.

Case: nearest neighbor $a = 1$

$$\begin{aligned} T(k, a = 1, \epsilon_1, \epsilon_2) &= \frac{4t^2 \sin^2(k)}{4t^2 \sin^2(k) + \epsilon_1^2 + \epsilon_2^2 + \epsilon_1 \epsilon_2 \left(2 \cos(2k) + \frac{\epsilon_1 + \epsilon_2}{t} \frac{\sin(2k)}{\sin(k)} + \frac{\epsilon_1 \epsilon_2}{t^2} \frac{\sin^2(k)}{\sin^2(k)} \right)} \\ &= \frac{4t^2 \sin^2(k)}{4t^2 \sin^2(k) + \epsilon_1^2 + \epsilon_2^2 + \epsilon_1 \epsilon_2 \left(2 \cos(2k) + \frac{\epsilon_1 + \epsilon_2}{t} 2 \cos(k) + \frac{\epsilon_1 \epsilon_2}{t^2} \right)} \end{aligned} \quad (\text{C.16})$$

Case: nearest neighbor $a = 1$, half filling $k_F = \pi/2$

$$\begin{aligned} T(a = 1, k_F = \pi/2) &= \frac{4t^2 \sin^2(k)}{4t^2 \sin^2(k) + \epsilon_1^2 + \epsilon_2^2 + \epsilon_1 \epsilon_2 \left(2 \cos(2k) + \frac{\epsilon_1 + \epsilon_2}{t} 2 \cos(k) + \frac{\epsilon_1 \epsilon_2}{t^2} \right)} \\ &= \frac{2t^2}{2t^2 + \epsilon_1^2 + \epsilon_2^2 + \epsilon_1 \epsilon_2 \left(-2 + \frac{\epsilon_1 \epsilon_2}{t^2} \right)} \\ &= \frac{2t^2}{2t^2 + \epsilon_1^2 + \epsilon_2^2 + \epsilon_1 \epsilon_2 \left(\frac{\epsilon_1 \epsilon_2}{t^2} - 2 \right)} \end{aligned} \quad (\text{C.17})$$

Case c): nearest neighbor $a = 1$, half filling $k_F = \pi/2$, both repulsive $\epsilon_1 = \epsilon_2 = \epsilon$

$$\begin{aligned} T(a = 1, k_F = \pi/2) &= \frac{2t^2}{2t^2 + \epsilon^2 + \epsilon^2 + \epsilon^2 \left(\frac{\epsilon^2}{t^2} - 2\right)} \\ &= \frac{2t^2}{2t^2 + \frac{\epsilon^4}{t^2}} \end{aligned} \tag{C.18}$$

Case c): nearest neighbor $a = 1$, half filling $k_F = \pi/2$, both repulsive $\epsilon_1 = \epsilon_2 = t$

$$\begin{aligned} T(a = 1, k_F = \pi/2) &= \frac{2t^2}{2t^2 + \frac{\epsilon^4}{t^2}} \\ &= \frac{2}{3} \end{aligned} \tag{C.19}$$

Case d): nearest neighbor $a = 1$, half filling $k_F = \pi/2$, opposite sign $\epsilon_1 = -\epsilon_2 = \epsilon$

$$\begin{aligned} T(a = 1, k_F = \pi/2) &= \frac{2t^2}{2t^2 + \epsilon_1^2 + \epsilon_2^2 + \epsilon_1\epsilon_2 \left(\frac{\epsilon_1\epsilon_2}{t^2} - 2\right)} \\ &= \frac{2t^2}{2t^2 + \epsilon^2 + \epsilon^2 - \epsilon^2 \left(-\frac{\epsilon^2}{t^2} - 2\right)} \\ &= \frac{2t^2}{2t^2 + 4\epsilon^2 + \frac{\epsilon^4}{t^2}} \end{aligned} \tag{C.20}$$

Case d): nearest neighbor $a = 1$, half filling $k_F = \pi/2$, opposite sign $\epsilon_1 = -\epsilon_2 = t$

$$\begin{aligned} T(a = 1, k_F = \pi/2) &= \frac{2t^2}{2t^2 + 4\epsilon^2 + \frac{\epsilon^4}{t^2}} \\ &= \frac{2}{7} \end{aligned} \tag{C.21}$$

Case: next nearest neighbor $a = 2$

$$T(a = 2, \epsilon_1, \epsilon_2) = \frac{4t^2 \sin^2(k)}{4t^2 \sin^2(k) + \epsilon_1^2 + \epsilon_2^2 + \epsilon_1\epsilon_2 \left(2 \cos(4k) + \frac{\epsilon_1 + \epsilon_2}{t} \frac{\sin(4k)}{\sin(k)} + \frac{\epsilon_1\epsilon_2}{t^2} 4 \cos^2(k)\right)} \tag{C.22}$$

Case: next nearest neighbor $a = 2$, half filling $k_F = \pi/2$

$$\begin{aligned}
 T(a = 2, k_F = \pi/2) &= \frac{2t^2}{2t^2 + \epsilon_1^2 + \epsilon_2^2 + \epsilon_1\epsilon_2 \left(2 + \frac{\epsilon_1 + \epsilon_2}{t} 0 + \frac{\epsilon_1\epsilon_2}{t^2} 0\right)} \\
 &= \frac{2t^2}{2t^2 + \epsilon_1^2 + \epsilon_2^2 + 2\epsilon_1\epsilon_2}
 \end{aligned} \tag{C.23}$$

Case e): next nearest neighbor $a = 2$, half filling $k_F = \pi/2$, $\epsilon_1 = \epsilon_2 = \epsilon$

$$\begin{aligned}
 T(a = 2, k_F = \pi/2) &= \frac{2t^2}{2t^2 + \epsilon_1^2 + \epsilon_2^2 + 2\epsilon_1\epsilon_2} \\
 &= \frac{2t^2}{2t^2 + \epsilon^2 + \epsilon^2 + 2\epsilon^2} \\
 &= \frac{2t^2}{2t^2 + 4\epsilon^2}
 \end{aligned} \tag{C.24}$$

Case f): next nearest neighbor $a = 2$, half filling $k_F = \pi/2$, $\epsilon_1 = -\epsilon_2 = \epsilon$

$$\begin{aligned}
 T(a = 2, k_F = \pi/2) &= \frac{2t^2}{2t^2 + \epsilon_1^2 + \epsilon_2^2 + 2\epsilon_1\epsilon_2} \\
 &= \frac{2t^2}{2t^2 + \epsilon^2 + \epsilon^2 - 2\epsilon^2} \\
 &= 1
 \end{aligned} \tag{C.25}$$

References

- [1] T. Giamarchi. *Quantum Physics in One Dimension*. International Series of Monographs on Physics. Clarendon Press, 2003.
- [2] A Kawabata. Electron conduction in one-dimension. *Rep. Progr. Phys.*, 70(2):219, 2007.
- [3] H. J. Schulz. Fermi liquids and non-Fermi liquids. In E. Akkermans, G. Montambaux, J. Pichard, and J. Zinn-Justin, editors, *Proceedings of Les Houches Summer School LXI*, page 533, Amsterdam, 1995. Elsevier.
- [4] G. Czycholl. *Theoretische Festkörperphysik: Von den klassischen Modellen zu modernen Forschungsthemen*. Springer-Lehrbuch. Springer, Berlin, Heidelberg, 2013.
- [5] Dan Bohr. *Quantum Transport in Strongly Correlated Systems: A Density Matrix Renormalization Group Study*. PhD thesis, DTU Lingby, Denmark, 2007.
- [6] J. Sólyom. *Fundamentals of the Physics of Solids: Volume 3 - Normal, Broken-Symmetry, and Correlated Systems*. Theoretical Solid State Physics: Interaction Among Electrons. Springer Berlin Heidelberg, 2010.
- [7] Ryogo Kubo. Statistical-Mechanical Theory of Irreversible Processes. I. General Theory and Simple Applications to Magnetic and Conduction Problems. *J. Phys. Soc. Jpn.*, 12(6):570–586, 1957.
- [8] W. Barford. *Electronic and Optical Properties of Conjugated Polymers*. International Series of Monographs on Physics. OUP Oxford, 2013.
- [9] F.H.L. Essler, H. Frahm, F. Göhmann, A. Klümper, and V.E. Korepin. *The One-Dimensional Hubbard Model*. Cambridge University Press, Cambridge, 2005.
- [10] F.H.L. Essler and V. Korepin. *Exactly Solvable Models Of Strongly Correlated Electrons*. Advanced Series In Mathematical Physics. World Scientific Publishing Company, 1994.
- [11] J. Sólyom. *Fundamentals of the Physics of Solids, Volume 2 - Electronic Properties*. Springer, Berlin, 2009.
- [12] Seigo Tarucha, Takashi Honda, and Tadashi Saku. Reduction of quantized conductance at low temperatures observed in 2 to 10 μm -long quantum wires. *Solid State Communications*, 94(6):413 – 418, 1995.

- [13] Marc Bockrath, David H. Cobden, Jia Lu, Andrew G. Rinzler, Richard E. Smalley, Leon Balents, and Paul L. McEuen. Luttinger-liquid behaviour in carbon nanotubes. *Nature*, 397(6720):598–601, 02 1999.
- [14] C. Blumenstein, J. Schäfer, S. Mietke, S. Meyer, A. Dollinger, M. Lochner, X. Y. Cui, L. Patthey, R. Matzdorf, and R. Claessen. Atomically controlled quantum chains hosting a Tomonaga-Luttinger liquid. *Nat Phys*, 7(10):776–780, 10 2011.
- [15] Yoshiyuki Ohtsubo, Jun-ichiro Kishi, Kenta Hagiwara, Patrick Le Fèvre, François Bertran, Amina Taleb-Ibrahimi, Hiroyuki Yamane, Shin-ichiro Ideta, Masaharu Matsunami, Kiyohisa Tanaka, and Shin-ichi Kimura. Surface Tomonaga-Luttinger-liquid state on Bi/InSb(001). *Phys. Rev. Lett.*, 115:256404, Dec 2015.
- [16] Nicolás Agraït, Carlos Untiedt, Gabino Rubio-Bollinger, and Sebastián Vieira. Onset of energy dissipation in ballistic atomic wires. *Phys. Rev. Lett.*, 88:216803, May 2002.
- [17] Nicolás Agraït, Carlos Untiedt, Gabino Rubio-Bollinger, and Sebastián Vieira. Electron transport and phonons in atomic wires. *Chemical Physics*, 281(2–3):231 – 234, 2002.
- [18] H. Ness and A.J. Fisher. Coherent electron injection and transport in molecular wires: inelastic tunneling and electron–phonon interactions. *Chemical Physics*, 281(2–3):279 – 292, 2002.
- [19] Joshua Hihath and Nongjian Tao. Electron–phonon interactions in atomic and molecular devices. *Progress in Surface Science*, 87(9–12):189 – 208, 2012.
- [20] T. Dürkop, S. A. Getty, Enrique Cobas, and M. S. Fuhrer. Extraordinary mobility in semiconducting carbon nanotubes. *Nano Lett.*, 4(1):35–39, January 2004.
- [21] Sen Li, Guang-Yao Huang, Jing-Kun Guo, Ning Kang, Philippe Caroff, and Hong-Qi Xu. Ballistic transport and quantum interference in InSb nanowire devices. *Chinese Physics B*, 26(2):027305, feb 2017.
- [22] S. Heinze, J. Tersoff, R. Martel, V. Derycke, J. Appenzeller, and Ph. Avouris. Carbon nanotubes as schottky barrier transistors. *Phys. Rev. Lett.*, 89:106801, Aug 2002.
- [23] Jesús A. del Alamo. Nanometre-scale electronics with iii-v compound semiconductors. *Nature*, 479:317, November 2011.

- [24] Philip F. Bagwell and Terry P. Orlando. Landauer’s conductance formula and its generalization to finite voltages. *Phys. Rev. B*, 40:1456–1464, Jul 1989.
- [25] Steven R. White. Density matrix formulation for quantum renormalization groups. *Phys. Rev. Lett.*, 69(19):2863–2866, Nov 1992.
- [26] Steven R. White. Density-matrix algorithms for quantum renormalization groups. *Phys. Rev. B*, 48(14):10345–10356, Oct 1993.
- [27] Ulrich Schollwöck. The density-matrix renormalization group in the age of matrix product states. *Ann. Phys.*, 326(1):96–192, 2011.
- [28] E. Jeckelmann. *Density-Matrix Renormalization Group Algorithms*, volume 739 of *Lecture Notes in Physics*, chapter 21, pages 597–619. Springer Berlin Heidelberg, 2008.
- [29] J.K. Cullum and R.A. Willoughby. *Lanczos Algorithms for Large Symmetric Eigenvalue Computations: Vol. 1: Theory*. Classics in Applied Mathematics. Society for Industrial and Applied Mathematics, 2002.
- [30] Eric Jeckelmann. Dynamical density-matrix renormalization-group method. *Phys. Rev. B*, 66(4):045114, Jul 2002.
- [31] E. Jeckelmann and H. Benthien. *Dynamical density-matrix renormalization group*, volume 739 of *Lecture Notes in Physics*, chapter 22, pages 621–635. Springer Berlin Heidelberg, 2008.
- [32] D. Bohr, P. Schmitteckert, and P. Wölfle. DMRG evaluation of the Kubo formula — Conductance of strongly interacting quantum systems. *EPL (Europhysics Letters)*, 73(2):246, 2006.
- [33] Jan-Moritz Bischoff and Eric Jeckelmann. Density-matrix renormalization group method for the conductance of one-dimensional correlated systems using the Kubo formula. *Phys. Rev. B*, 96:195111, Nov 2017.
- [34] W. Apel and T. M. Rice. Combined effect of disorder and interaction on the conductance of a one-dimensional fermion system. *Phys. Rev. B*, 26:7063–7065, Dec 1982.
- [35] C. L. Kane and Matthew P. A. Fisher. Transport in a one-channel Luttinger liquid. *Phys. Rev. Lett.*, 68:1220–1223, Feb 1992.
- [36] C. L. Kane and M. P. A. Fisher. Transmission through barriers and resonant tunneling in an interacting one-dimensional electron gas. *Phys. Rev. B*, 46:15233–15262, Dec 1992.

- [37] J. Sirker. The Luttinger liquid and integrable models. *Int. J. Mod. Phys. B*, 26(22):1244009, 2012.
- [38] Jerom Jebai. Streuung eines elektronischen Wellenpakets durch eine doppelte dynamische Störstelle, Bachelor’s thesis, March 2019.
- [39] Jan-Moritz Bischoff and Eric Jeckelmann. Density-matrix renormalization group study of the linear conductance in quantum wires coupled to interacting leads or phonons. *Phys. Rev. B*, 100:075151, Aug 2019.
- [40] I. Safi and H. J. Schulz. Transport in an inhomogeneous interacting one-dimensional system. *Phys. Rev. B*, 52:R17040–R17043, Dec 1995.
- [41] K. Janzen, V. Meden, and K. Schönhammer. Influence of the contacts on the conductance of interacting quantum wires. *Phys. Rev. B*, 74:085301, Aug 2006.
- [42] V. Meden, S. Andergassen, W. Metzner, U. Schollwöck, and K. Schönhammer. Scaling of the conductance in a quantum wire. *Europhys. Lett.*, 64(6):769–775, 2003.
- [43] V. Meden and U. Schollwöck. Conductance of interacting nanowires. *Phys. Rev. B*, 67:193303, May 2003.
- [44] Dan Bohr and Peter Schmitteckert. Strong enhancement of transport by interaction on contact links. *Phys. Rev. B*, 75:241103, Jun 2007.
- [45] A. Branschädel, G. Schneider, and P. Schmitteckert. Conductance of inhomogeneous systems: Real-time dynamics. *Ann. Phys. (Berlin)*, 522:657, 2010.
- [46] F. Heidrich-Meisner, I. González, K. A. Al-Hassanieh, A. E. Feiguin, M. J. Rozenberg, and E. Dagotto. Nonequilibrium electronic transport in a one-dimensional Mott insulator. *Phys. Rev. B*, 82:205110, Nov 2010.
- [47] Luis G. G. V. Dias da Silva, Khaled A. Al-Hassanieh, Adrian E. Feiguin, Fernando A. Reboredo, and Elbio Dagotto. Real-time dynamics of particle-hole excitations in Mott insulator-metal junctions. *Phys. Rev. B*, 81:125113, Mar 2010.
- [48] D. Morath, N. Sedlmayr, J. Sirker, and S. Eggert. Conductance in inhomogeneous quantum wires: Luttinger liquid predictions and quantum Monte Carlo results. *Phys. Rev. B*, 94:115162, Sep 2016.
- [49] Florian Lange, Satoshi Ejima, Tomonori Shirakawa, Seiji Yunoki, and Holger Fehske. Spin transport through a spin- $\frac{1}{2}$ XXZ chain contacted to fermionic leads. *Phys. Rev. B*, 97:245124, Jun 2018.

- [50] Eric Jeckelmann and Steven R. White. Density-matrix renormalization-group study of the polaron problem in the Holstein model. *Phys. Rev. B*, 57:6376–6385, Mar 1998.
- [51] S. Ejima and H. Fehske. Luttinger parameters and momentum distribution function for the half-filled spinless fermion Holstein model: A DMRG approach. *Europhys. Lett.*, 87:27001, 2009.
- [52] X. Zotos, F. Naef, and P. Prelovsek. Transport and conservation laws. *Phys. Rev. B*, 55:11029–11032, May 1997.
- [53] F. Heidrich-Meisner, A. Honecker, D. C. Cabra, and W. Brenig. Thermal conductivity of anisotropic and frustrated spin- $\frac{1}{2}$ chains. *Phys. Rev. B*, 66:140406, Oct 2002.
- [54] Robin Steinigeweg, Jacek Herbrych, Xenophon Zotos, and Wolfram Brenig. Heat conductivity of the Heisenberg spin-1/2 ladder: From weak to strong breaking of integrability. *Phys. Rev. Lett.*, 116:017202, Jan 2016.
- [55] C. Karrasch, D. M. Kennes, and F. Heidrich-Meisner. Thermal Conductivity of the One-Dimensional Fermi-Hubbard model. *Phys. Rev. Lett.*, 117:116401, Sep 2016.
- [56] A. Nocera and G. Alvarez. Spectral functions with the density matrix renormalization group: Krylov-space approach for correction vectors. *Phys. Rev. E*, 94:053308, Nov 2016.
- [57] A. Nocera, N. D. Patel, J. Fernandez-Baca, E. Dagotto, and G. Alvarez. Magnetic excitation spectra of strongly correlated quasi-one-dimensional systems: Heisenberg versus Hubbard-like behavior. *Phys. Rev. B*, 94:205145, Nov 2016.
- [58] P.K. Ghosh. *Quantum Mechanics*. Alpha Science International Limited, 2014.

Acknowledgements

I would like to express my utmost gratitude to Professor Eric Jeckelmann for giving me the opportunity to work on this thesis project under his supervision. His guidance and countless discussions were of immeasurable value to this project. It was also an honor and a valuable learning experience to assist in his lectures and exercises.

I also would like to acknowledge Doktor Anas Abdelwahab. I greatly appreciate his willingness to share his profound knowledge about DMRG and one-dimensional models that were essential to this work.

My thanks go to the secretary of the institute, Gitta Richter, who helped me tackle the travel- and accounting organization. This provided me with the time to concentrate on the project.

Special thanks go to my girlfriend and my family who ardently supported my research and provided me with the necessary foundation to succeed.

At last, I would like to thank the *School for Contacts in Nanosystems* under the leadership of Professor Haug for the organization of numerous workshops and schools that were always a fun experience and helped me to get a broader vision regarding the research in solid state physics. I am also grateful for the financial support provided by the *School for Contacts in Nanosystems* and the DFG (Deutsche Forschungsgemeinschaft) that made this research possible.

Currucilum Vitae

Personal Information

Name: Jan-Moritz Bischoff

Date of birth: 27.01.1989

Place of birth: Hannover

Education

- 2015–2019 Promotion - Leibniz University Hannover
Doctoral thesis: DMRG method for the linear conductance of one-dimensional correlated systems
- 2013–2015 Master Studies - Leibniz University Hannover
Master's thesis: Theory of Phase contrast imaging of cold molecules
- 2012–2013 Master Studies - Hua Zhong University of Science and Technology, Wuhan
Semester abroad
- 2009–2012 Bachelor Studies - Leibniz University Hannover
Bachelor's thesis: Untersuchung von Einzelphotonenquellen am Beispiel von Quantenpunkten
- 2001–2008 General University Entrance Qualification, Kaiser-Wilhelm- und Ratsgymnasium

List of Publications

- 3 November 2017 *Density-matrix renormalization group method for the conductance of one-dimensional correlated systems using the Kubo formula*
Jan-Moritz Bischoff and Eric Jeckelmann
Physical Review B96, 195111
- 28 August 2019 *Density-matrix renormalization group study of the linear conductance in quantum wires coupled to interacting leads or phonons*
Jan-Moritz Bischoff and Eric Jeckelmann
Physical Review B100, 075151